Harmonic State-Space Modelling of an HVdc Converter with Closed-Loop Control

Sheng-Pu Hwang

A thesis presented for the degree of
Doctor of Philosophy
in
Electrical and Computer Engineering
at the
University of Canterbury,
Christchurch, New Zealand.

2013

Maths do not lie.

Alan Wood
April, 2012

Everything has to be linear.

Lance Frater
July, 2011

ABSTRACT

Frequency domain models for power electronic circuits are either based on iterative techniques such as Newton's method or linearised around an operating point. Iterative frequency domain models provide great accuracy as they are capable of calculating the exact switching instants of the device. On the other hand, the accuracy of a linearised frequency domain model relies on the magnitude of input waveform to be small so that the circuit's operating point does not vary or varies very little. However, an important advantage of a linearised model is its ability to provide insight into waveform distortion interaction, more specifically, the frequency cross-coupling around a power electronic circuit.

In general, a linearised model for harmonic analysis would not normally include the description of feedback control. Likewise a linearised model for control analysis would usually disregard frequency interactions above the fundamental (or the most significant component); that is assuming the cross-coupling between harmonic frequencies does not affect the dynamics of control. However, this thesis proposes that a linearised model for control analysis shall also include the complete description of frequency cross-coupling between harmonics to produce the correct dynamic response.

This thesis presents a harmonic state-space (HSS) model of an HVdc converter that incorporates the full effect of varying switching instants, both through control and commutation period dynamics, while remaining within the constraints of a linear time-invariant (LTI) system. An example is given using the HSS model to explain how a close to 5^{th} harmonic resonance contributes to the dominant system response through the frequency cross-coupling of the converter and the controller feedback loop. The response of the system is validated against a time domain model built in PSCAD/EMTDC, and more importantly, the correct response cannot be produced without including the harmonic interactions beyond the fundamental frequency component.

ACKNOWLEDGEMENTS

First of all, I would like to express my deepest gratitude to my supervisory team, Dr. Alan Wood, Prof. Neville Watson, and Prof. Pat Bodger. This research would not have been possible without their wisdom, patience, and encouragements. I would like to thank Alan for sparking my interest in this research since my undergraduate days and for the many helpful and lengthy discussions over the past few years which included many wonderful analogies between caving and research. I would like to thank Neville for his guidance during my PhD, and especially for his spiritual leadership in our weekly bible studies. I would like to thank Pat for his continual support and encouragements in the past few years.

I would like to express my gratitude to my postgraduate comrades, Lance Frater, Dr. Andrew Lapthorn, Dr. Jordan Orillaza, Bhaba Das, Ida Hussain, Dr. Thahirah Syed Jalal, Ali Farzanehrafat, Kalyan Malla, Parash Acharya, Ming Zhong, Dr. Rowan Sinton, Ryan van Herel, Dr. Victor Lo, Dr. Amanda Zhang, Kelvin Gong, Alejandro Castellanos Escamilla, Rabia Nazir, Tae Woo Kim, Lisiate Takau, Shreejan Pandey, Yanosh Irani, Alex Hu, Tauseef Khawaja, Harry Li, Zahid Rauf, and Senthuran Sivasubramaniam for the many joyful moments we shared together. I must thank Lance, Jordan, and Bhaba for the many never-ending discussions on this research; their support towards this thesis is highly appreciated.

I would like to acknowledge the technical staffs at the Electrical and Computer Engineering Department, Ken Smart, Edsel Villa, and Jac Woudberg for their support over the past years as well as their effort in keeping the department safe. I would also like to acknowledge Joseph Huang, Chan Yeong Ying, Patrick Yeung, Jonny Lung, Jennifer Wen, Jeff Wen, Tommy Yang, Sarah Frater, Naomi Harmer, Alice Bao, and everyone that I have met during my PhD for their friendship and kindness over the past years. I would also like to acknowledge the Electric Power Engineering Centre and Transpower for their financial support during my PhD.

Finally, I would like to express my most sincere appreciation to my parents, my family, and my girlfriend Joanna for their love, patience, and support.

:]

CONTENTS

LIST OF FIGURES

LIST OF TABLES

GLOSSARY

NOMENCLATURE

α_0	Base case thyristor switch-on instant
β_0	Base case thyristor switch-off instant
$\Gamma(t)$	Modulation vector to transform a harmonic domain vector into a time domain signal
$\mathbf{\Lambda}_{\int}$	Frequency transfer matrix for integration
$\mathbf{\Lambda}_{\Phi}$	Frequency transfer matrix for phase shifting
$\mathbf{\Lambda}_{D}$	Frequency transfer matrix for differentiation
$\mathcal{D}\{\cdot\}$	Operation to convert a sequence into a diagonal matrix
$\mathcal{T}\{\cdot\}$	Operation to convert a sequence into a Toeplitz matrix
μ_0	Base case commutation period
ω_0	Fundamental frequency measured in rad/s
$\Psi(t)$	A time domain switching function
f_0	Fundamental frequency measured in Hz
i_{dc}	DC side current

s	Complex frequency ($s = \sigma + j\omega$)
$v_{\phi,1}$	Three-phase ac voltage at fundamental frequency
v_{dc}	DC side voltage
v_{ll}	AC side line-to-line voltage

ABBREVIATIONS

AMIT	Amplitude Modulated Impulse Train
DFT	Discrete Fourier Transform
DHD	Dynamic Harmonic Domain
EHD	Extended Harmonic Domain
EMP	Exponentially Modulated Periodic
FACTS	Flexible AC Transmission System
FD	Frequency Domain
FTM	Frequency Transfer Matrix
HSS	Harmonic State-Space
HTF	Harmonic Transfer Function
HVdc	High-Voltage Direct Current
LTI	Linear Time-Invariant
LTP	Linear Time-Periodic

MDHD	Modified Dynamic Harmonic Domain
NIS	Numerical Integration Substitution
ODE	Odinary Differential Equation
PI	Proportional-Integral
PLL	Phase-Locked Loop
PLO	Phase-Locked Oscillator
PWM	Pulse Width Modulation
SIV	Switching Instant Variation
SVC	Static VAr Compensator
TCR	Thyristor Controlled Reactor
TCSC	Thyristor Controlled Series Capacitor
TD	Time Domain
VCO	Voltage-Controlled Oscillator

Chapter 1

INTRODUCTION

1.1 GENERAL OVERVIEW

Electricity is without question an essential element of modern society, and with the ever increasing use of electricity, new possibilities for generation are constantly being explored. Due to the current focus on reducing carbon emissions around the world, the use of renewable energy has been a popular topic amongst policy makers. The biggest challenge with renewable energy is perhaps the fact that its sources are often located in remote areas that are far away from the load centres. Hence, the transmission of electricity is an important aspect of renewable energy.

Ever since the introduction of flexible ac transmission system (FACTS) controllers and high voltage direct current (HVdc) links, the transmission of electricity has greatly evolved. These power electronic technologies bring great benefits to a power system due to their ability to improve the flexibility (controllable and bi-directional power flow), the capability (increase of active power flow), and the security (voltage and transient stability) of the electricity transmission network. Furthermore, as the technology of power semiconductor devices matures and as the concepts of FACTS continue to advance, the proliferation of power electronic controllers in the power system is guaranteed [Hingorani and Gyugyi 2000].

Despite the fact that the transmission of electric power can be facilitated by the use of power electronic controllers, they also contribute to some problems that may occur within the power system; one example of which is waveform distortion leading to instability due to harmonics. This is often referred to as harmonic instability, and some of the various incidents recorded around the world are listed as follows:

- In the early days of the HVdc technology, the use of individual firing control often led to harmonic instability. Ainsworth concluded that the majority of the incidents reported were due to a positive feedback loop in the conventional firing control scheme. The distortion in the supply voltage causes the firing pulses to occur irregularly which in turn magnifies the original distortion [Ainsworth 1967]. This research was the catalyst for his design of the

phase-locked oscillator (PLO) which became an integral part of the firing control today [Ainsworth 1968].

- In 1992, Hammad reported a second harmonic instability that occurred in the Chateauguay HVdc installation [Hammad 1992]. It was concluded that the instability was due to a combination of several factors, namely, the ac side and the dc side impedances, converter transformer saturation, and the control. Using frequency domain techniques, Hammad presented a thorough analysis of the system and proposed the installation of auxiliary dc stabilising controls and second harmonic filters.

- In 1977, Mathur and Sharaf conducted an investigation into the malfunctioning of the Nelson River HVdc scheme [Mathur and Sharaf 1977]. It was concluded that the non-characteristic harmonics which occurred on the dc side following a disturbance in the supply caused the dc side filters to overload and trip out of service. They acknowledged that their steady-state harmonic analysis was limited to transient distortion in the ac bus voltage.

- In 1992, Thallam presented a review of existing HVdc installations that are connected to relatively weak ac systems compared to the rating of their dc systems [Thallam 1992]. It was reported that these systems often suffer from low order harmonic resonances, transient overvoltages, voltage fluctuations, or control system instability.

In order to produce efficient controller designs and prevent system failures, there is a strong need for modelling techniques to provide better understanding of power electronic systems, and to predict the interaction between multiple power electronic controllers in the same network [Mohan *et al.* 1994].

1.2 THESIS OBJECTIVES

In 1954, the first commercial HVdc link was commissioned between mainland Sweden and Gotland island. Since then, many more have been installed around the world with a total transmission capacity exceeding 50 GW, and it will continue to grow in the foreseeable future[1]. Due to their large power ratings, HVdc links are perhaps the biggest contributors of waveform distortion in the high-voltage power system. Therefore, there is value in developing detailed models of the HVdc converter to study the waveform modulation aspect of an HVdc system. There have been a number of frequency domain based models published in the past, but due to the constraint of traditional frequency domain formulation, they have been confined to the steady-state description of the system.

[1] See Appendix A for a map of ABB HVdc classic installations around the world.

This thesis aims to take advantage of a new modelling approach known as the harmonic state-space (HSS) in order to develop a linearised model of an HVdc converter. The goal of this HSS model is to capture full system dynamics, including harmonic/frequency coupling effects, during both the transient and steady-state, and be suitable for small-signal stability analysis. A model of a power electronic circuit is never complete without the description of control as feedback controllers are known to have a significant effect on the dynamics of the system. Thus this model must accommodate converter control. Furthermore, as the model is to be linearised around an operating point, the effects of switching instant variation have to be incorporated. Lastly, this HSS model will be posed in the form of a linearised time-invariant (LTI) system, therefore it will be usable by classic control analysis methods such as pole-zero analysis for stability studies.

1.3 THESIS OUTLINE

Chapter 2 presents a review of existing modelling techniques for power electronic circuits. They are categorised into time domain, frequency domain, and hybrid time and frequency domain. In particular, linearised frequency domain models are further divided into subcategories according to their application, namely, models for harmonic analysis or models for control analysis. The merits of each modelling technique are identified, and possible improvements are discussed. The kernel of this chapter is to highlight that the clear distinction between models for analysing harmonic interactions and models for analysing controller stability is diminishing. A complete model of a power electronic system has to incorporate both aspects which is the motivation behind this research of HSS modelling.

Chapter 3 begins with a brief description of linearised small-signal modelling and the linear time-periodic (LTP) system class. It is then followed by theories of frequency separation and harmonic balance which are essential to the formulation of the HSS framework. Practical aspects of applying the HSS to the modelling of a three-phase power electronic circuit are discussed; they include system reduction through harmonic truncation, and the modelling of switching instant variation in an LTI environment.

Chapter 4 presents an HSS model of an uncontrolled HVdc converter system. The waveform modulation nature of the converter is captured by a set of switching functions that describe the connection of the thyristor bridge. Procedures for modelling switching instant variation at the end of commutation using voltage impulses are detailed. Validation of this open-loop model is achieved by comparing transient waveform shapes against a time domain simulation; comparisons between steady-state harmonics are also presented.

Chapter 5 extends the HSS model to a closed-loop model by incorporating a constant current controller on the dc side. The converter control system consists of three components, a current

transducer, a proportional-integral (PI) controller, and an actuator. In addition, a simple ac side system including a harmonic filter is incorporated into the closed-loop model. The model is validated against a time domain based model by comparing waveform shapes. S-domain pole plots are used to explain a low frequency resonance resulting from the frequency cross-coupling characteristic of the converter and the interaction between system impedances. The result from this chapter validates the HSS approach of including control and harmonic interactions beyond the fundamental frequency.

Chapter 6 closes this thesis by summarising the major achievements of this research, and identifies possible future improvements and extensions to the HSS model developed.

Chapter 2

LITERATURE REVIEW

2.1 INTRODUCTION

There is a long history behind the modelling of HVdc converters and FACTS devices. Broadly speaking, the modelling techniques available can be classified as time domain (TD), frequency domain (FD), or hybrid TD-FD techniques. According to the dictionary published by the Institute of Electrical and Electronics Engineers [IEEE 2000], the terms time domain and frequency domain are defined as follows:

- Time Domain: A function in which the signals are represented as a function of time.
- Frequency Domain: A function in which frequency is the independent variable.

These two modelling domains are widely used, and each has its own merits and disadvantages. In general, time domain modelling naturally accommodates nonlinear circuit equations, but its simulation time can be slow due to the existence of very long and very short time constants in a typical system. On the other hand, frequency domain modelling provides fast steady-state solutions, and explicitly represents the frequency coupling nature of power electronic circuits. However, it cannot be used to capture the dynamics of a system. In 2010, an IEEE Task Force identified some existing techniques that provide an interface between the two domains [Chavez *et al.* 2010]. Their intention was to develop a hybrid method to combine the merits of both domains for the modelling of power system networks with nonlinear and switching elements.

This chapter presents an overview of existing techniques for modelling power electronic circuits, and identifies their strengths and weaknesses. The aim of this process is to reveal the motivations behind this research in the harmonic state-space (HSS). The subsequent sections describe the techniques used in each modelling domain. In particular, linearised frequency domain models are further divided into different categories according to their application, namely, models for harmonic analysis, models for control analysis, and models suitable for both harmonic and control analysis as described in [Wood *et al.* 2000].

2.2 TIME DOMAIN MODELLING

Time domain modelling is the most mature power system simulation approach, and it is widely used in popular software packages such as ATP-EMTP, EMTP-RV and PSCAD/EMTDC [Woodford *et al.* 1983]. These programs rely on various mathematical methods to solve differential equations for both electromagnetic and electromechanical systems in the time domain. One of the most popular methods in use was developed by Dommel in 1969, and is often referred as Dommel's method [Dommel 1969, Dommel and Meyer 1974, Dommel 1997]. It was a combination of the trapezoidal rule and Bergeron's method [Frey and Althammer 1961], capable of solving transients in both single and multiphase networks. Although at the time of its introduction, the algorithm was not particularly time efficient in handling nonlinear differential equations, it was later improved by the use of the compensation method which confines the time consuming process (iterative calculation through Newton-Raphson) for nonlinear or time-varying elements to the incident branches or nodes only [Dommel 1971]. However, the method requires the network to be separated into subsystems, each containing only one nonlinear or time-varying element. More recently, Noda *et al.* proposed a predictor-corrector method that solved this limitation [Noda *et al.* 1997].

In general, time domain methods are capable of modelling linear and nonlinear elements in both the steady and transient state, but they can suffer from numerical oscillation and long simulation initialisation. The error introduced by numerical oscillation is cumulative due to the fixed time-step (Δt) used in trapezoidal integrations. Furthermore, the time-step determines the maximum frequency that can be captured, and if it is not properly chosen, it could lead to an inaccurate solution for a switching network [Power Electronics Modeling Task Force & Digital Simulation Working Group 1997]. However, this issue can be mitigated using interpolation methods [Kulicke 1981, Kuffel *et al.* 1997] or multiple time-step sizes [Maguire and Gole 1991, Semlyen and de León 1993]. The simulation initialisation refers to the time required to simulate the entire transient process before arriving at the steady-state. If a small time-step is used for high solution accuracy, the simulation can be computationally expensive and time consuming, especially in poorly damped networks [Dommel *et al.* 1986]. Several techniques have been proposed to accelerate the transient calculation process, namely, the shooting method [Aprille Jr. and Trick 1972, Perkins *et al.* 1995], extrapolation to the limit cycle [Segundo and Medina 2008], and the waveform relaxation technique [Wang and Marti 1996]. There also have been some attempts to obtain the steady-state initial condition through frequency domain [Perkins *et al.* 1995] and hybrid TD-FD techniques [Murere *et al.* 1995].

Although time domain modelling methods are well established, they do not provide explicit information about the harmonic and interharmonic interaction around a power electronic circuit. However, despite its limited contribution for harmonic analysis, time domain simulations can be used to provide validations for a new modelling technique [Ino *et al.* 1985]. Hence,

PSCAD/EMTDC simulations are used in this thesis to not only provide conditions of operating points, but also serves as a benchmark for the modelling technique developed.

2.3 FREQUENCY DOMAIN MODELLING

It is without question that thyristor based power electronic circuits are time-variant and exhibit nonlinearity. For an HVdc converter, the time-variance is associated with the switching operation of the thyristor bridge while the nonlinearity is due to the dependence of thyristor switching instants on system conditions. This means that the converter generates a range of output frequencies for any single frequency input (frequency coupling), and the resulting spectrum varies in a nonlinear manner with respect to the variation in the input. In order to capture these characteristics, models built in the frequency domain or its subset, the harmonic domain, are either iterative or linearised around an operating point[1]. The following subsections describe a number of frequency domain models related to the work presented in this thesis.

2.3.1 Iterative Models

Harmonic domain models often employ iterative algorithms, such as Newton-Raphson, to solve system mismatch equations. They produce accurate results due to their ability to determine the exact switching instants. One of the most detailed iterative model of the HVdc converter was developed by Smith [Smith *et al.* 1996a, Smith *et al.* 1996b]; his model is powered by a multi-variable Newton's method, and it produced results that were validated against a time domain model. In addition, Smith developed a method to accelerate the iterative process by taking advantage of the sparsity in the system Jacobian matrix. Later, this work was continued by Bathurst who extended the model to a full HVdc link [Bathurst *et al.* 1999, Bathurst *et al.* 2000, Bathurst 1999]. An excellent review of iterative harmonic domain models of ac-dc converter systems can be found in [Smith *et al.* 1998].

Interestingly, both Smith and Bathurst reported that their respective models often produce a solution after a single iteration. This means that the initial Jacobian matrix, which is a linearisation of the system mismatch equations, does not require updating in the iterative process to reach a convergence. This was an early acknowledgement that the HVdc converter could be reasonably linear in the frequency domain. Using a similar iterative frequency domain model, Hume investigated the linearity of the converter by injecting various types of distortion [Hume 2002]. He concluded that the converter was linearisable for small-signal analysis, and outlined the effects of switching instant variation on the converter waveforms due to a change in the operating

[1] Frequency domain models that are linearised around an operating point are also often referred to as small-signal models to highlight the fact that linearity may be assumed when the deviation from the operating point which the linearisation is based on is small.

point. Similarly, these effects were proven to be linearisable for small distortion levels. More recently, Collins presented a number of iterative harmonic domain models of FACTS devices including a static synchronous series compensator (SSSC), a unified power flow controller (UPFC), and a STATCOM [Collins 2006].

2.3.2 Linearised Models for Control Analysis

One of the earliest linearised complex frequency domain model of the HVdc converter was presented in [Persson 1970]. Persson adopted the transfer function technique (also known as switching or describing functions) to model the switching operation of the thyristor bridge. His model fully described the frequency transfers around the 6-pulse converter with a constant current controller (individual phase firing), and in particular, the effect of the commutation period was also included. In addition, the 6-pulse transfer functions were expanded to model a complete mono-polar HVdc link, and control analysis was conducted through the use of the Nyquist diagrams generated from the model. Later, this model was harmonically truncated, and only preserved the fundamental frequency components in the transfers [Sucena Paiva and Freris 1974]. Similarly, Nyquist plots were used to determine the stability of the converter system. This was an early indication that high-order harmonics were believed to be insignificant for control analysis. This thesis offers an alternative perspective.

In 1993, Wood presented a linearised HVdc converter model including both firing angle control and commutation period variation in his transfer functions [Wood 1993]. He also reduced his transfers to a three-port model (three coupled frequencies around the converter, namely, the positive sequence fundamental frequency, the negative sequence fundamental frequency, and the dc frequency), and used it to describe the frequency dependent impedance of an HVdc converter. In addition, the concept of composite resonance (the overall resonance of the converter system taking into account of the frequency transfers of the thyristor bridge; this approach is also used in this thesis) was introduced. From a different approach, Todd systematically fitted poles and zeros to form an s-domain model matching the results generated from Wood's model [Todd and Wood 1997]. This model was used for frequency domain based control design.

2.3.2.1 Generalised State-Space Averaging and Dynamic Phasor

Recently, there have been a number attempts at extending the description of harmonics to the transient state through techniques such as generalised state-space averaging and dynamic phasor. These are described in the following paragraphs.

State-space averaging has been perceived as a suitable and powerful method for the modelling and control design of pulse width modulation (PWM) dc-dc converters [Middlebrook

and Cuk 1976]. However, this method can only be applied to switching circuits that satisfy the small ripple assumption. More specifically, the method assumes that the dominant Fourier coefficient of a circuit waveform is its dc frequency component, and that the circuit waveforms are linear functions of time during each switching stage. In order to make state-space averaging applicable for resonant type converters, Sanders *et al.* modified the original method by using time dependent Fourier series expansion with a sliding window along the circuit waveforms [Sanders *et al.* 1991]. The new method was referred to as generalised state-space averaging. Similarly, their new approach retains only the dc frequency component, though it was acknowledged that higher order coefficients could also be included; they recommended that the fundamental frequency component should be included for a resonant converter model.

On the other hand, the term dynamic phasor was introduced by Mattavelli, Verghese, and Stanković in 1997 to emphasize the time-varying nature of the Fourier coefficients in their approach [Mattavelli *et al.* 1997]. However, the dynamic phasor method essentially shares the same formulation as the generalised state-space averaging method. Since then, they have published a number of dynamic phasor models for power electronic circuits including FACTS devices [Mattavelli *et al.* 1999, Stanković *et al.* 2000, Stefanov and Stanković 2002]. More recently, Gomes *et al.* proposed an improved controller design for Static VAr Compensator (SVC) using their dynamic phasor model of the device, and again, they acknowledged the fact that higher frequencies need to be modelled if their interaction with the ac network or other nearby FACTS devices is of interest. Similarly, He and Cai and Dang *et al.* have also reported that higher frequency components need to be incorporated for a more accurate representation of the system, and they have included the third and fifth harmonic components in their respective models of a thyristor controlled series capacitor (TCSC) [He and Cai 2005, Dang *et al.* 2007]. However, both models lack the presence of active control.

Although it was not explicitly stated as such, Wood *et al.* published two small-signal models of the HVdc converter through a similar approach as dynamic phasor in 2003. The first small-signal model presented in [Osauskas and Wood 2003] fully describes a mono-polar HVdc link, and did not assume the presence of an ideal equidistant firing angle control system. Thus, a phase-locked loop (PLL) system consisting of an error signal calculator, a PI controller, and a voltage-controlled oscillator (VCO) was incorporated in the model. This model was used to study the dynamics of an HVdc system in the frequency range between 2 and 200 Hz on the dc side, and it was acknowledged that this model needs to be expanded for the analysis of different specialised phenomena. For example, the frequency coupling between the zero frequency and the positive sequence second harmonic components of the transformer magnetising current has to be modelled if the interest is in the instability associated with transformer core saturation. The second paper describes a small-signal dynamic model of a controlled HVdc converter, and it was used to optimise the control design for the converter connecting to a weak ac network [O'Reilly *et al.* 2003]. Both of these models adopted a modular approach by breaking the overall

system up into smaller subsystems, and connecting them up systematically. A similar approach is used in this thesis to form the harmonic state-space model of an HVdc converter.

2.3.3 Linearised Models for Harmonic Analysis

In 1985, Sakui and Fujita presented a linearised frequency domain model of a controlled thyristor rectifier for their study of harmonic problems [Sakui *et al.* 1985]. In particular, they included the commutation period in their switching functions, and the effects of dc side current ripple was also incorporated. Later, this work was extended to model a diode rectifier [Sakui *et al.* 1989], and an uncontrolled thyristor rectifier for unbalanced power supply by allowing different length of commutation period in each phase [Sakui and Fujita 1992]. The highlight of this work, though it was not heavily emphasised at the time, is the significant effect of the variation in the commutation period on the converter frequency transfer functions. Around the same time, Hu and Yacamini also presented a switching function based frequency domain model of the HVdc converter [Hu and Yacamini 1992, Hu and Yacamini 1993]. However, despite generating accurate results, their model did not have an exact representation of the ac side currents during the commutation period. The ac side currents were modelled by a linear ramping function during the commutation period to simplify the analysis.

In 1998, Osauskas and Wood presented a frequency domain model of a thyristor controlled reactor (TCR) [Osauskas and Wood 1998]. They linearised the frequency transfers between the thyristor currents, terminal voltages, and thyristor firing angle. In addition, the frequency transfers were used to develop an admittance matrix for the TCR valid for both harmonics and interharmonics. A similar model was developed by Orillaza and Wood, and a brief preview was given on extending their steady-state model to a dynamic representation through the use of harmonic state-space [Orillaza and Wood 2008]. In 2001, Osauskas *et al.* published a linearised model of a 6-pulse HVdc converter. The effects of switching instant variation (at both the beginning and the end of commutation period) were linearised, however, feedback control was absent in the model. This model was extended to a full HVdc link including ac side impedances in the following year by Hume *et al.*, and it was used to analyse the effects of ac system impedance variation on the transfers of distortion through the HVdc link [Hume *et al.* 2002]. Later, the same model was modified to account for interharmonic distortions [Hume *et al.* 2003]. Continuing with their modelling approach, Wood and Osauskas presented a very complete small-signal model of a STATCOM including a PLL system and a constant reactive power controller, and achieved excellent agreement with time domain simulations for realistic levels of ac system voltage unbalance [Wood and Osauskas 2004].

2.3.3.1 Extended Harmonic Domain and Dynamic Harmonic Domain

Traditionally, frequency domain models of power electronic circuits have been confined to a steady-state description of frequency coupling. However, their frequency coupling characteristic also exists during the transient state. Hence, it is apparent that frequency domain based models could be extended to allow a dynamic description of system signals. More recently, this has been achieved through techniques such as extended harmonic domain (EHD) and dynamic harmonic domain (DHD). Models based on these techniques generally have been applied for analysing the interaction between harmonics, and due to this reason, they have incorporated harmonics up to a relatively high order. However, most of them have not included any form of feedback control.

The extended harmonic domain was first introduced in 2003 by Rico *et al.*, and it was applied for the modelling of a PWM based STATCOM [Rico *et al.* 2003]. The EHD technique models the system using standard state-space equations for time-periodic systems, and the transient variation of state-variables and input signals are described using exponentially modulated periodic (EMP) signals. In 2010, Vyakaranam *et al.* applied the EHD technique to model a wide range of FACTS devices including a TCSC, an SVC, an SSSC, and a UPFC [Vyakaranam *et al.* 2010]. Despite its broad coverage, these models did not incorporate the effects of switching instant variation (SIV), i.e. the switching instants were not allowed to vary with system distortion.

In 2008, Chavez and Ramirez were the first to use the term dynamic harmonic domain to describe their approach to model a three-phase transmission line; their method shares an identical formulation with the EHD models [Chavez and Ramirez 2008]. The model was used to analyse the travelling waves in the transmission line with a nonlinear load, and coincidentally, non-harmonic resonant frequencies were observed in a system with long transmission lines. They acknowledged that the DHD method can be extended to separately study this phenomenon. Later, Garcia and Madrigal presented a DHD model of a TCR, and in particular, their model uses numerical integration substitution (NIS) to solve for the exact thyristor switching instants, thus this model remains time-variant and cannot be used to perform classical linear time-invariant (LTI) system analysis [Garcia and Madrigal 2009]. However, they have closed the loop in their model with a proportional-integral (PI) controller. In 2011, Garcia *et al.* extended the paper to highlight the use of companion harmonic circuit models for the modelling of power electronic devices [Garcia *et al.* 2011].

The DHD technique has also been extended to model interharmonics where the time domain inputs are transformed into the modified dynamic harmonic domain (MDHD) through the use of discrete Fourier transform (DFT), and the ordinary differential equations (ODEs) describing the system are solved by numerical integration [Chavez 2010, Ramirez 2011].

2.3.4 Harmonic State-Space Models for both Harmonic and Control Analysis

The dynamic modelling methods developed to date are very good, though the majority of these models either omit the representation of frequency coupling beyond the fundamental frequency component or neglect any form of feedback control. In general, power electronic converters rely on active controllers to ensure satisfactory operation, and it is without question that their dynamics depend heavily on the controls. Therefore, for the approach to be useful, the associated controllers must be modelled. In addition, numerous authors have acknowledged that the frequency coupling between higher order harmonics must be included if their interaction with the ac network or other power electronic devices is of primary interest. In order to address these two concerns, the harmonic state-space has been applied to the development of models where both control and the frequency coupling between higher order harmonics are included.

The harmonic state-space (HSS) is an extension to the conventional frequency domain in the sense that it preserves the explicit description of the frequency coupling nature of power electronic circuits, but more importantly, it extends the description of frequency coupling to the transient state. It was first developed by Werely in 1991 for his study in periodic time-varying systems [Wereley 1991]. Werely presented a thorough formulation of the HSS through classical theories, namely Floquet theory and Hill theory, and applied the framework for the study of helicopter vibration control. Although useful for power electronic systems which are also time-periodic, the HSS was left unnoticed by power engineers for many years. In 2000, Möllerstedt was the first to apply the HSS in the analysis of a power electronic system [Mollerstedt 2000a]. In particular, he presented a closed-loop HSS model of an inverter locomotive for the study of an harmonic instability that occurred in Zürich [Mollerstedt 2000b]. His model was linearised, and Nyquist plots were used to determine the stable boundary of the controller gains.

In 2008, Love and Wood published an HSS model of a Buck-Boost converter operating in discontinuous conduction mode [Love and Wood 2008]. They analytically described the different switching stages of the converter, and how they evolve from one to the other. In addition, the contribution of switching instant variation to the state-variables and outputs is also derived. Love also presented an HSS model of an uncontrolled Graetz bridge in his thesis [Love 2007]. Later, Orillaza *et al.* published a conference paper describing the use of voltage impulses to model the effects associated with switching instant variation in an HSS environment [Orillaza *et al.* 2010]. More recently, Orillaza and Wood presented a closed-loop model of a TCR with voltage control [Orillaza and Wood 2013]. This work showed that the controller responded to a system resonance around the fifth harmonic which is usually not expected to be within the bandwidth of the controller, but due to the strong coupling between the fifth harmonic and fundamental frequency, the system resonance also exists as a low frequency variation. In addition, standard root-locus technique was applied for control design. The highlight of this work is confirming the need to include higher order frequency coupling to observe potential system res-

onances. This background has led up to the closed-loop model of an HVdc converter presented in this thesis.

2.4 HYBRID TIME AND FREQUENCY DOMAIN MODELS

On a different track, Semlyen and Medina developed a hybrid method that combines both time and frequency domain techniques [Semlyen and Medina 1995]. In general, the linear components of the system including transmission lines and some part of the loads are modelled in the frequency domain while the nonlinear components such as power electronic converters or time-varying loads are modelled in the time domain. This hybrid process is iterative, and for every iteration a mismatch equation is solved for each harmonic current at each bus; its solution is used to update the voltages until a convergence is reached. The procedure is relatively straight forward for the linear parts where an admittance matrix is formed. However, a time domain simulation is required for the nonlinear components to determine the periodic steady-state harmonic currents, and the results are converted into the frequency domain by Fourier transforms. It was reported that time domain simulations can be accelerated by the extrapolation to the limit cycle technique [Guckenheimer and Holmes 2002]. The hybrid method is considered to be suitable when great accuracy is required in modelling large networks.

In 2010, Chavez *et al.* presented a review of the available techniques for interfacing time and frequency domain [Chavez *et al.* 2010]. They broadly summarised the techniques into the following approaches:

- solving the network in the frequency domain, and post-process the converged results back to time domain.
- allowing the model to go back and forth from frequency domain to time domain in an iterative process.
- computing the solution in both time domain and frequency domain simultaneously.

Although these hybrid methods achieve the objective of obtaining accurate steady-state and transient state of a network containing linear and nonlinear elements, they can be complicated due to the need to post-process the results through transformations or separating the network elements into time domain and frequency domain. They acknowledged that both modelling in the dynamic harmonic domain or the wavelet transform technique are direct approaches to capture the dynamics of harmonic signals.

2.5 CONCLUSIONS

In this chapter, a review of power system modelling techniques was given. They were divided into time domain, frequency domain, and hybrid time and frequency domain techniques. Traditionally, time domain is the only available modelling approach for transient type analysis while frequency domain techniques are often applied to explicitly represent the frequency interaction around a power electronic circuit or the modelling of frequency dependent impedances. As the number of switching devices and nonlinear elements increases in the power system, and for the fact that their associated effects do not only exist during the steady-state but are also present in the transient state, the clear distinction between the traditional use of time or frequency domain diminishes. There is a demand for modelling techniques that are capable of describing nonlinear time-variant components throughout the transient state before arriving at the steady-state.

In addition, active controls are always employed in power electronic systems, and they have significant contribution to the overall system dynamics. Thus, it is of great importance to incorporate them into the system model to properly represent the dynamics of the system. Furthermore, it has become apparent from Orillaza's work that the frequency coupling beyond the fundamental component needs to be modelled [Orillaza 2012]. This is because a high frequency system resonance may fall within the bandwidth of the controller due to frequency coupling and affect the stability of the system. The only way to observe this is if the frequency couplings around the system resonance are represented in the model.

Chapter 3

HARMONIC STATE-SPACE MODELLING FOR POWER ELECTRONIC CIRCUITS

3.1 BACKGROUND

The Harmonic State-Space (HSS) was first introduced in [Wereley 1991]. The primary objective of Wereley's research was to develop a modelling framework to accommodate linear time-periodic (LTP) systems, and to gain more insight to the design of feedback control for this class of system. His new modelling framework, the HSS, provides a frequency domain environment that not only describes the harmonics of signals in the steady-state, but also captures the time evolution of each individual harmonic during transient conditions. Furthermore, the HSS explicitly models the frequency coupling nature of LTP systems, and as it is analogous to linear time-invariant (LTI) systems it benefits from the well established theories for LTI systems, and to a certain extent some of the existing techniques for analysing LTI systems can be applied.

Wereley's thesis was highly generalised in terms of classical control theory and was not noticed by power engineers till the publication of the papers included in [Mollerstedt 2000a]. Mollerstedt built on Wereley's work and applied the HSS framework to model a number of electrical systems, more specifically a small distribution network with light dimmers, a diode converter based locomotive, and a power converter with reactive power control. This was the first time the HSS was applied in the context of power electronics.

Following Mollerstedt's work, Love generalised the procedures and developed a systematic approach to modelling power electronic circuits using the HSS framework [Love 2007]. Love's HSS models include the Buck-Boost converter, the Graetz Bridge, and the capacitor commutated converter. A noteworthy contribution is the mathematics developed for implementing the effects of switching instant variation (SIV) in HSS models of power electronic circuits. More recently, Orillaza built an HSS model of a three-phase thyristor-controlled reactor (TCR) with a voltage controller [Orillaza 2012], and illustrated that the interaction between the fundamental frequency and the characteristic harmonic frequency that is closest to the natural frequency of the system needs to be modelled carefully to show the system resonance.

The objective of this chapter is to present the pivotal mathematics required to formulate the basic HSS framework, and extend it to accommodate the modelling of three-phase power electronic circuits. Firstly, a brief introduction to LTP systems is presented, followed by the theories of *frequency separation* and *harmonic balance* leading up to the formulation of the HSS. The second part of this chapter focuses on the extension of the HSS framework in order to model power electronic circuits efficiently and accurately, this includes system reduction and the modelling of *switching instant variation* in the linear environment.

3.2 LINEARISATION AROUND AN OPERATING POINT

Power electronic circuits often exhibit nonlinearity in addition to their time-variant nature. The switching instants of a power electronic circuit, specifically the switch-on instants and the switch-off instants, may vary due to disturbances in its electrical or control inputs. Regardless whether fully controlled switches or semi-controlled switches are used, a power electronic circuit is only linear time-periodic if its switching instants are fixed. In small-signal modelling, a nonlinear power electronic circuit can be linearised around an operating point, that is the relationships between small-signal waveforms around the power electronic circuit are linear with any small deviation from this operating point. An operating point defines the switching instants of a power electronic circuit, and it must remain unchanged or change very little when subjected to distortion for the linearisation to be accurate.

In [Hume 2002], an iterative frequency domain model of the HVdc converter was used to investigate its nonlinear behaviour associated with waveform distortion. It was found that the converter is nonlinear as its operating point varies with waveform distortion, but the variation in its operating point is small. This shows that the HVdc converter can be linearised around an operating point, which is referred to as the base case operating point for the rest of this thesis. The base case operating point approximates the true converter operating point with small-signal waveform distortion.

The operating point of the HVdc converter is defined by the following base case quantities: the fundamental ac voltage, the dc side current, the converter commutation reactance, and the thyristor firing angle[1]. If the three-phase base case fundamental ac voltage is defined as

$$v_{\phi,1} = V_1 \cos\left(\omega_0 t - \phi\right) \tag{3.1}$$

where V_1 is the peak ac side voltage magnitude, ω_0 is the fundamental frequency, and ϕ is 0, $\frac{2\pi}{3}$, and $\frac{4\pi}{3}$ radians for phase a, b, and c respectively, then the commutation period, μ_0 is calculated

[1]The thyristor firing angle is measured from the zero crossings of the ac side line-to-line voltage waveforms to the switch-on instants.

as

$$\mu_0 = \cos^{-1}\left(\cos\alpha_0 - \frac{2X_{com}I_{dc}}{\sqrt{3}V_1}\right) - \alpha_0 \tag{3.2}$$

Thus the base case thyristor switch-off instant is given by,

$$\beta_0 = \alpha_0 + \mu_0 \tag{3.3}$$

These switching instants fully defines the base case operating point of an HVdc converter.

3.3 LINEAR TIME-PERIODIC SYSTEM

Large rotating machines are used in power systems to generate electric power. This means that the voltage waveforms generated from these machines are sinusoidal in steady-state, and hence the switching pattern of power electronic converters derived from these waveforms are periodic. Thus a typical power system with connected power electronic circuits fall under the class of linear time periodic (LTP) systems in small-signal modelling. The LTP system class traces its origin back to the French mathematician Floquet and the American physicist Hill with their publications in [Floquet 1883] and [Hill 1886] respectively. Traditionally LTP systems have been associated with the study of astronomical phenomena, and since then, the study of LTP systems has extended to more modern applications such as the rotation of helicopter blades [Wereley 1991], and power electronic circuits [Mollerstedt 2000a]. The LTP system class in the time domain is formally described in definition 1.

Definition 1 (Linear Time Periodic)**.** *Any linear time periodic system can be represented by a set of first order linear state-space equations. The first equation is known as the state dynamic equation,*

$$\dot{x}(t) = A(t)x(t) + B(t)u(t) \tag{3.4}$$

and the second equation is known as the measurement equation,

$$y(t) = C(t)x(t) + D(t)u(t) \tag{3.5}$$

where the state matrix, $A(t)$, the control matrix, $B(t)$, the measurement matrix, $C(t)$, and the feed-forward matrix, $D(t)$ are time periodic matrices, i.e. $A(t+T) = A(t)$ and similarly for $B(t)$, $C(t)$, and $D(t)$.

The frequency domain has been commonly used for studying linear time-invariant (LTI) systems because of its frequency separation property. In the steady-state, a complex exponential input signal at any given frequency can be mapped to a complex exponential output signal of the same frequency through the LTI system transfer function, but possibly with a different magnitude and phase angle.

On the contrary, applying a complex exponential input signal at a given frequency to an LTP system does not result in a complex exponential output signal of the same frequency, but instead a sum of complex exponential signals. Suppose the LTP system has a *pumping frequency* of ω_p, then the steady-state response resulting from a complex exponential input signal, $u(t) = e^{st}$, can be written in general as

$$y(t) = Ae^{st} + Be^{(s+j\omega_p)t} + Be^{(s-j\omega_p)t} \tag{3.6}$$

Thus, to allow the frequency separation property to be applicable to LTP systems, a different basis signal must be used.

3.4 EXPONENTIALLY MODULATED PERIODIC SIGNAL

The Exponentially Modulated Periodic (EMP) signal class was first introduced by Hill over a hundred years ago, it represents all realisable signals in an LTP system under both steady and transient conditions [Hill 1878]. The EMP signal class is formally described in definition 2, and serves as the basis signal class for the rest of this thesis.

Definition 2 (Exponentially Modulated Periodic Signal)**.** *An Exponentially Modulated Periodic (EMP) signal is the product of a complex Fourier series and a complex exponential written as*

$$u(t) = e^{st} \sum_{n=-\infty}^{\infty} u_n e^{jn\omega_0 t} \tag{3.7}$$

where ω_0 is the fundamental frequency of the periodic signal, and s is a complex number.

The first component of an EMP signal, e^{st}, modulates each harmonic represented in the complex Fourier series, allowing the harmonics to vary with time, and hence describing the dynamics of harmonics under transient conditions. With e^{st} tending towards zero over time, the harmonics tend towards steady-state, thus in steady-state an EMP signal becomes an exponential Fourier series.

3.5 FREQUENCY SEPARATION

With the EMP signal class serving as the basis for all realisable signals, the frequency separation property of an LTI system is applicable to an LTP system. Suppose the input signal to an LTP system is written as

$$u(t) = u_p(t)e^{st} \tag{3.8}$$

where $u_p(t)$ is a time-periodic signal. The LTP system transfer function $H(s)$ must map the input signal to an output signal in the form given in (3.9),

$$y(t) = H(s)u_p(t)e^{st} \tag{3.9}$$

and therefore,

$$\begin{aligned} y(t-T) &= H(s)u(t-T) \\ &= H(s)u_p(t-T)e^{s(t-T)} \\ &= H(s)u_p(t)e^{st}e^{-sT} \\ &= y(t)e^{-sT} \end{aligned} \tag{3.10}$$

But the desired output signal from the LTP system can be written in the form,

$$y(t) = y_p(t)e^{st} \tag{3.11}$$

where $y_p(t)$ is a time-periodic signal. Thus, rearranging (3.11) to make $y_p(t)$ the subject, and substituting both $t = t - T$ and (3.10) into the equation, this yields

$$\begin{aligned} y_p(t-T) &= y(t-T)e^{-s(t-T)} \\ &= y(t)\cancel{e^{-sT}}e^{-st}\cancel{e^{sT}} \\ &= y(t)e^{-st} \\ &= y_p(t) \end{aligned} \tag{3.12}$$

This confirms that $y_p(t)$ is a time-periodic function which can be replaced with a complex Fourier series, such that the output signal is written as

$$y(t) = e^{st}\sum_{n=-\infty}^{\infty} y_n e^{jn\omega_0 t} \tag{3.13}$$

Hence the LTP system transfer function maps an input EMP signal to an output EMP signal, but more importantly LTP systems exhibit frequency coupling, that is any input frequency is coupled to a set of output frequencies separated by n times the fundamental frequency of the LTP system. Thus a correct model of an LTP system must be able to accurately capture the coupling between frequencies.

3.6 HARMONIC BALANCE

Since its original introduction in [Hill 1886], the method of harmonic balance has been used in a large number of studies for finding the steady-state solution to nonlinear systems, for example in [Nakhla 1976] and [Arrillaga *et al.* 1995]. The harmonic balance terminology essentially refers to the *linear independence* of each harmonic of the steady-state solution to an LTP system, i.e. each element is not a linear combination of the other elements. The harmonic balance method involves a Fourier series expansion of the input signal into a set of complex exponentials at harmonic frequencies, and more importantly the set of complex exponentials form an orthonormal basis over the fundamental period $[0, 2\pi]$. The series expansion of the input signal suggests that the system transfer function should also be expanded to the same set of complex exponentials.

Given that both of the series expansions of the input signal and the system transfer function form an orthonormal basis, the resulting output must also be an orthonormal set of complex exponentials. The mapping from a harmonic of the input signal through a particular harmonic of the transfer function is unique to a single harmonic of the output signal, therefore every element of the output vector is linearly independent of each other.

Consider a system described by a set of state-space equations introduced in definition 1, and its $A(t)$, $B(t)$, $C(t)$, and $D(t)$ matrices are time-periodic. If the input signal, $u(t)$, is in the form of an EMP signal such that,

$$u(t) = \sum_{m=-\infty}^{\infty} u_m e^{(jm\omega_0+s)t} \tag{3.14}$$

then from the principal of frequency separation, its steady-state solution must also be in the form of an EMP signal at the same set of harmonic frequencies, and hence its gradient takes the form of (3.16).

$$x(t) = \sum_{m=-\infty}^{\infty} x_m e^{(jm\omega_0+s)t} \tag{3.15}$$

$$\dot{x}(t) = \sum_{m=-\infty}^{\infty} (jm\omega_0 + s)\, x_m e^{(jm\omega_0+s)t} \tag{3.16}$$

Following the harmonic balance method, the time-periodic $A(t)$, $B(t)$, $C(t)$, and $D(t)$ matrices are expanded using complex Fourier series, i.e.

$$A(t) = \sum_{n=-\infty}^{\infty} A_n e^{jn\omega_0 t} \tag{3.17}$$

and similarly for $B(t)$, $C(t)$, and $D(t)$. Substituting the complex Fourier series above into the state dynamic equation in (3.4), and let m denote the set of harmonic frequencies of the state

variable to allow frequency cross-coupling, a new state dynamic equation can be written as

$$\begin{aligned}\sum_{n=-\infty}^{\infty}(jn\omega_0+s)\,x_n e^{(jn\omega_0+s)t} &= \sum_{n=-\infty}^{\infty}A_n e^{jn\omega_0 t}\sum_{m=-\infty}^{\infty}x_m e^{(jm\omega_0+s)t}\\ &+\sum_{n=-\infty}^{\infty}B_n e^{jn\omega_0 t}\sum_{m=-\infty}^{\infty}u_m e^{(jm\omega_0+s)t}\\ &=\sum_{n,m=-\infty}^{\infty}A_n x_m e^{j(n+m)\omega_0 t}e^{st}+\sum_{n,m=-\infty}^{\infty}B_n u_m e^{j(n+m)\omega_0 t}e^{st}\\ &=\sum_{n,m=-\infty}^{\infty}A_{n-m}x_m e^{jn\omega_0 t}e^{st}+\sum_{n,m=-\infty}^{\infty}B_{n-m}u_m e^{jn\omega_0 t}e^{st}\end{aligned}\tag{3.18}$$

The principle of harmonic balance states that every harmonic of the steady-state solution to a system is linearly independent, therefore every harmonic of the gradient of the steady-state solution must also be linearly independent. Noting cancellation, (3.18) can be rewritten for each harmonic of the gradient of the steady-state solution as

$$\begin{aligned}(jn\omega_0+s)\,x_n e^{(jn\omega_0+s)t} &= \sum_{m=-\infty}^{\infty}A_{n-m}x_m e^{jn\omega_0 t}e^{st}+\sum_{m=-\infty}^{\infty}B_{n-m}u_m e^{jn\omega_0 t}e^{st}\\ \therefore sx_n &= \sum_{m=-\infty}^{\infty}A_{n-m}x_m+\sum_{m=-\infty}^{\infty}B_{n-m}u_m-jn\omega_0 x_n\end{aligned}\tag{3.19}$$

Similarly, the measurement equation in (3.5) is rewritten as

$$\begin{aligned}y_n e^{(jn\omega_0+s)t} &= \sum_{m=-\infty}^{\infty}C_{n-m}x_m e^{jn\omega_0 t}e^{st}+\sum_{m=-\infty}^{\infty}D_{n-m}u_m e^{jn\omega_0 t}e^{st}\\ \therefore y_n &= \sum_{m=-\infty}^{\infty}C_{n-m}x_m+\sum_{m=-\infty}^{\infty}D_{n-m}u_m\end{aligned}\tag{3.20}$$

Equations in (3.19) and (3.20) form a new set of state-space equations and fully describe the dynamics of an LTP system in time domain. In order to take advantage of standard LTI techniques to analyse an LTP system, the LTP system must be converted to an equivalent LTI system.

3.7 HARMONIC STATE-SPACE

The time-periodic nature of an LTP system means that in the frequency domain it can be described by a set of steady-state harmonics, and becomes a time-invariant system (i.e. no longer a function of time). The process of multiplying each single harmonic of the state variable $x(t)$ or the control input $u(t)$ by the complex Fourier series of $A(t)$, $B(t)$, $C(t)$, or $D(t)$ is cumbersome.

The same process can be implemented by a single matrix multiplication, given that $A(t)$, $B(t)$, $C(t)$, or $D(t)$ are constructed in the form of a Toeplitz matrix filled with appropriate Fourier coefficients while $x(t)$ and $u(t)$ are decomposed into column vectors with their respective Fourier coefficients. The formal definition of a Toeplitz matrix is given in definition 3.

Definition 3 (Toeplitz Matrix)**.** *Given a sequence* $\{a_n\}_{n=-\infty}^{\infty}$*, the Toeplitz transform operation on the sequence maps the elements of the sequence to a doubly infinite Toeplitz matrix of the form,*

$$\mathcal{T}\{a_n\} = \begin{bmatrix} \ddots & \vdots & \vdots & \vdots & \\ \cdots & a_{+0} & a_{-1} & a_{-2} & \cdots \\ \cdots & a_{+1} & a_{+0} & a_{-1} & \cdots \\ \cdots & a_{+2} & a_{+1} & a_{+0} & \cdots \\ & \vdots & \vdots & \vdots & \ddots \end{bmatrix} \tag{3.21}$$

As previously mentioned, any LTP system exhibits a frequency coupling property. The use of Toeplitz matrices allows the input frequency to be stepped up or stepped down to the set of appropriate output frequencies, fully representing the frequency coupling nature of LTP systems. This type of matrix that provides coupling of frequencies around the power electronic circuit model is referred to as *frequency transfer matrix* (FTM).

Representing the set of first-order differential equations for each state variable harmonic as Toeplitz matrices means that the $-jn\omega_0$ component of (3.19) also has to be expanded into an appropriate matrix form, and it is achieved by using a diagonal matrix defined in definition 4. This leads to the formal description of the harmonic state-space (HSS) framework defined in definition 5.

Definition 4 (Diagonal Matrix)**.** *The diagonal matrix transform converts a sequence,* $\{a_n\}_{n=-\infty}^{\infty}$ *into a diagonal matrix of the form,*

$$\mathcal{D}\{a_n\} = \begin{bmatrix} \ddots & & & & \\ & a_{-1} & & & \\ & & a_{+0} & & \\ & & & a_{+1} & \\ & & & & \ddots \end{bmatrix} \tag{3.22}$$

Definition 5 (Harmonic State-Space)**.** *Given an LTP system written in the form described in definition 1. Posing its state variable, input control signal, and output signal as EMP signals, through the method of harmonic balance the LTP system can be rewritten as*

$$sX = (\mathcal{A} - \mathcal{N})\, X + \mathcal{B}U \tag{3.23}$$

$$Y = \mathcal{C}X + \mathcal{D}U \tag{3.24}$$

where $\mathcal{A}$, $\mathcal{B}$, $\mathcal{C}$, and $\mathcal{D}$ denote the Fourier coefficients of $A(t)$, $B(t)$, $C(t)$, and $D(t)$ constructed in the form of Toeplitz matrices respectively, and $\mathcal{N}$ is the diagonal matrix of the sequence $\{jn\omega_0\}_{n=-\infty}^{\infty}$ such that,

$$\mathcal{N} = \begin{bmatrix} \ddots & & & & & \\ & -j\omega_0 & & & & \\ & & 0 & & & \\ & & & +j\omega_0 & & \\ & & & & \ddots & \end{bmatrix} \tag{3.25}$$

The state variable, $x(t)$, system input signal, $u(t)$, and the system output signal, $y(t)$ are in the form of infinite dimensioned vectors of the Fourier coefficients of the steady-state harmonics from their respective complex Fourier series expansion such that,

$$X = \begin{bmatrix} \vdots \\ X_{-1} \\ X_{+0} \\ X_{+1} \\ \vdots \end{bmatrix} \qquad U = \begin{bmatrix} \vdots \\ U_{-1} \\ U_{+0} \\ U_{+1} \\ \vdots \end{bmatrix} \qquad Y = \begin{bmatrix} \vdots \\ Y_{-1} \\ Y_{+0} \\ Y_{+1} \\ \vdots \end{bmatrix} \tag{3.26}$$

The equation in (3.23) describes the transient evolution of each harmonic of the state variable, and it is equivalent to the first-order differential equation describing an LTI system. The s operator is a complex phasor varying with time; during transient conditions it describes the variation of each harmonic frequency with respect to time, and it vanishes as the harmonics reach steady-state, i.e. no further variation in the harmonics. Note, sX does not represent the gradient of the state variable's time domain waveform, it strictly represents the variation of the harmonics over time.

A harmonic vector used to represent a signal in the HSS is filled with complex Fourier coefficients, and it comprises of both positive and negative frequency components, but they must be complex conjugate pairs for the signal to be real. Strictly speaking, the dc component in the harmonic vector should be a scalar, but for a uniform representation in this modelling, it is treated as a complex number with zero imaginary component.

A constant harmonic vector can be reconstructed as a time-periodic waveform in the time domain through a multiplication with a modulation vector, $\Gamma(t)$. The process modulates each complex number in the harmonic vector by its associated frequency and summed to result in a time domain equivalent; it can be mathematically described as

$$x(t) = \Gamma(t)X \tag{3.27}$$

where

$$\Gamma(t) = \begin{bmatrix} \cdots & e^{-j2\omega_0 t} & e^{-j\omega_0 t} & 1 & e^{+j\omega_0 t} & e^{+j2\omega_0 t} & \cdots \end{bmatrix}$$

In the case of a time-varying harmonic vector, a time domain representation can still be reconstructed as long as the modulation is done at each time step.

3.7.1 Series RL Circuit

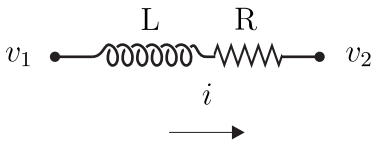

Figure 3.1: A series RL circuit.

A series RL circuit as shown in Fig. 3.1 can be described a first-order differential equation, and choosing the inductor current as the state variable as well as the output, the differential equation can be rewritten in the state-space format as

$$\begin{aligned} \begin{bmatrix} \dot{i(t)} \end{bmatrix} &= \begin{bmatrix} \frac{-R}{L} \end{bmatrix} \begin{bmatrix} i(t) \end{bmatrix} + \begin{bmatrix} \frac{1}{L} & \frac{-1}{L} \end{bmatrix} \begin{bmatrix} v_1(t) \\ v_2(t) \end{bmatrix} \\ \begin{bmatrix} i(t) \end{bmatrix} &= \begin{bmatrix} 1 \end{bmatrix} \begin{bmatrix} i(t) \end{bmatrix} + \begin{bmatrix} 0 & 0 \end{bmatrix} \begin{bmatrix} v_1(t) \\ v_2(t) \end{bmatrix} \end{aligned} \tag{3.28}$$

Applying the HSS formulation described in Sec. 3.7, the state-space matrices in (3.28) can be converted into constant matrices without any frequency cross-coupling such as

$$\mathcal{A} - \mathcal{N} = \begin{bmatrix} \ddots & & & & & \\ & \frac{-R}{L} & & & & \\ & & \frac{-R}{L} & & & \\ & & & \frac{-R}{L} & & \\ & & & & \ddots \end{bmatrix} - \begin{bmatrix} \ddots & & & & & \\ & -j\omega_0 & & & & \\ & & 0 & & & \\ & & & +j\omega_0 & & \\ & & & & \ddots \end{bmatrix} \tag{3.29}$$

$$\mathcal{B} = \begin{bmatrix} \ddots & & & & \ddots & & & & \\ & \frac{1}{L} & & & & \frac{-1}{L} & & & \\ & & \frac{1}{L} & & & & \frac{-1}{L} & & \\ & & & \frac{1}{L} & & & & \frac{-1}{L} & \\ & & & & \ddots & & & & \ddots \end{bmatrix} \tag{3.30}$$

$$\mathcal{C} = \begin{bmatrix} \ddots & & & & \\ & 1 & & & \\ & & 1 & & \\ & & & 1 & \\ & & & & \ddots \end{bmatrix} \tag{3.31}$$

$$\mathcal{D} = \begin{bmatrix} \ddots & & & & \ddots & & & \\ & 0 & & & & 0 & & \\ & & 0 & & & & 0 & \\ & & & 0 & & & & 0 \\ & & & & \ddots & & & \ddots \end{bmatrix} \tag{3.32}$$

3.8 FREQUENCY TRANSFER MATRIX

Performing a mathematical operation on a system signal in the HSS framework is achieved by multiplying its associated vector of frequency components to an appropriate frequency transfer matrix (FTM). Depending on the type of operation, an FTM is either in the form of a Toeplitz matrix or in the form of a diagonal matrix. More specifically, if the operation results in an output vector of harmonics, and each element of the output vector is solely coupled to an input harmonic of the same frequency, that is the operation does not exhibit frequency cross-coupling between the input and output signals, then the FTM associated with this particular operation is in the form of a diagonal matrix, otherwise the FTM is in the form of a Toeplitz matrix.

The mathematical operations that do not exhibit frequency cross-coupling include differentiation, integration, and time shifting while the mathematical operation that does exhibit frequency cross-coupling is typically a multiplication between two time-periodic waveforms. The FTMs associated with the aforementioned mathematical operations are described as follows:

Differentiation FTM

Given a steady-state time-periodic signal $x(t)$ with a fundamental frequency of ω_0. The process of differentiating this signal can be described in the time domain as

$$y(t) = \frac{dx(t)}{dt} \tag{3.33}$$

or in the frequency domain for each harmonic as

$$Y_n = jn\omega_0 X_n \tag{3.34}$$

where $n \in [-\infty, \infty]$, and hence the FTM associated with this operation is written in the form,

$$\mathbf{\Lambda}_D = \begin{bmatrix} \ddots & & & & & \\ & -j\omega_0 & & & & \\ & & 0 & & & \\ & & & +j\omega_0 & & \\ & & & & \ddots & \end{bmatrix} \tag{3.35}$$

Integration FTM

Given a steady-state time-periodic signal $x(t)$ with a fundamental frequency of ω_0. The process of integrating this signal can be described in the time domain as

$$y(t) = \int x(t)dt \tag{3.36}$$

or in the frequency domain for each harmonic as

$$Y_n = \frac{1}{jn\omega_0} X_n \tag{3.37}$$

where $n \in [-\infty, \infty]$, and hence the FTM associated with this operation is written in the form,

$$\mathbf{\Lambda}_{\int} = \begin{bmatrix} \ddots & & & & & \\ & \frac{1}{-j\omega_0} & & & & \\ & & 0 & & & \\ & & & \frac{1}{+j\omega_0} & & \\ & & & & \ddots & \end{bmatrix} \tag{3.38}$$

and the integration of the dc frequency component has to be treated separately.

Phase Shifting FTM

Given a steady-state time-periodic signal $x(t)$ with a fundamental frequency of ω_0. Phase shifting this signal by θ radians in the time domain is equivalent to shifting every n^{th} harmonic by $n\theta$ in the frequency domain and this can be described as

$$Y_n = e^{jn\theta} X_n \tag{3.39}$$

where $n \in [-\infty, \infty]$, and hence the FTM associated with this operation is written in the form,

$$\mathbf{\Lambda}_{\Phi}(\theta) = \begin{bmatrix} \ddots & & & & \\ & e^{-j\theta} & & & \\ & & 0 & & \\ & & & e^{+j\theta} & \\ & & & & \ddots \end{bmatrix} \tag{3.40}$$

Multiplication FTM

The product of two time-periodic signal $h(t)$ and $u(t)$ is equivalent to the element-wise convolution of their associated Fourier coefficients structured as infinite dimensioned vectors H and U. This operation can be implemented as an FTM multiplication, and the process is described as

$$\begin{aligned} y(t) &= h(t)u(t) \\ \sum_{n=-\infty}^{\infty} Y_n e^{jn\omega_0 t} &= \sum_{n=-\infty}^{\infty} H_n e^{jn\omega_0 t} \sum_{m=-\infty}^{\infty} U_m e^{jm\omega_0 t} \\ &= \sum_{n-m=-\infty}^{\infty} H_{n-m} \sum_{m=-\infty}^{\infty} U_m e^{jm\omega_0 t} \end{aligned} \tag{3.41}$$

which can be rewritten as a matrix multiplication where H is posed in the form of a Toeplitz matrix,

$$\mathcal{T}\{H\} = \begin{bmatrix} \ddots & \vdots & \vdots & \vdots & \\ \cdots & H_{+0} & H_{-1} & H_{-2} & \cdots \\ \cdots & H_{+1} & H_{+0} & H_{-1} & \cdots \\ \cdots & H_{+2} & H_{+1} & H_{+0} & \cdots \\ & \vdots & \vdots & \vdots & \ddots \end{bmatrix} \tag{3.42}$$

This operation is often used in the sampling of a system signal with a switching function. In the context of an HSS model, the constant Fourier coefficients of a switching function populates the diagonals of an FTM, and the resulting FTM is posed as the $\mathcal{D}$ matrix of a subsystem with its $\mathcal{A}$, $\mathcal{B}$, and $\mathcal{C}$ matrices fixed at zero.

3.9 HARMONIC TRANSFER FUNCTION

The HSS framework is analogous to the LTI state-space framework, thus its set of first-order differential equations can be used in the same way to derive a linear system transfer function,

$\mathcal{H}(s)$, that describes the relationship between the input signals and the output signals, i.e.

$$Y = \mathcal{H}(s)U \tag{3.43}$$

This linear system transfer function is known as the harmonic transfer function (HTF), and it is given in definition 6.

Definition 6 (Harmonic Transfer Function)**.** *The harmonic transfer function is a doubly infinite matrix, and it describes the linear mapping from the harmonics of the input signals to the harmonics of the output signals. The HTF can be derived from the set of first-order differential equations describing an HSS system such that,*

$$\mathcal{H}(s) = \mathcal{C}\left[s\mathcal{I} - (\mathcal{A} - \mathcal{N})\right]^{-1}\mathcal{B} + \mathcal{D} \tag{3.44}$$

where $\mathcal{I}$ is an infinite dimensioned identity matrix. Hence the harmonic transfer function is in the form,

$$\mathcal{H}(s) = \begin{bmatrix} \ddots & \vdots & \vdots & \vdots & \\ \cdots & H_{+0}(s) & H_{-1}(s) & H_{-2}(s) & \cdots \\ \cdots & H_{+1}(s) & H_{+0}(s) & H_{-1}(s) & \cdots \\ \cdots & H_{+2}(s) & H_{+1}(s) & H_{+0}(s) & \cdots \\ & \vdots & \vdots & \vdots & \ddots \end{bmatrix} \tag{3.45}$$

where the subscripts of $H(s)$ represents the step in harmonic order required to establish the cross-coupling between the harmonics of the input signal and the harmonics of the output signal.

The derivation of the HTF requires the doubly infinite matrix, $\mathcal{H}(s)$, to be invertible. That is each linearly independent first-order differential equation of the system must be unique, this is discussed more in detail in the next chapter. This concludes the preliminary discussion of the HSS, the remaining of this chapter focuses on the application of the HSS to the modelling of power electronic circuits.

3.10 REFERENCE FRAMES

From the previous sections, it is clear that an LTP system exhibits cross-coupling between harmonics of the input signal and the harmonics of the output signal through its specific HTF. In reality, the harmonic coupling is really frequency coupling. That is, any frequency contained in the input signal is coupled in the same way as harmonic frequencies to a set of frequencies in the output signal.

Due to the fact that any frequency experiences the same frequency modulation through the HTF, and that an EMP signal is the sum of an infinite number of harmonics each modulated with a complex exponential that is varying over time, any frequency can be posed as a frequency modulated version of a harmonic. This implies that the HSS framework features the ability to observe the same frequency from an infinite number of reference frames and still correctly represent the frequency coupling nature of LTP systems.

For example, an interharmonic with a frequency that is k times the fundamental frequency can be observed from the reference frame of the n^{th} harmonic if the reference harmonic is modulated by a complex exponential at $(k-n)$ frequency such that,

$$x_k(t) = X_k e^{st} e^{j(k-n)\omega_0 t} e^{jn\omega_0 t} \tag{3.46}$$

Therefore any interharmonic or frequency in the HSS framework can be fully modelled under both steady-state and transient conditions as a harmonic frequency from the Fourier series expansion modulated by a complex exponential at an appropriate frequency.

3.11 SYSTEM REDUCTION

Previous sections in this chapter have assumed an untruncated expansion of periodic signals using complex Fourier series, thus the associated vectors and matrices have infinite dimensions. However, this is not possible to implement in practice; all vectors and matrices must have a finite dimension in a digital model. Furthermore, each harmonic frequency of a state variable is posed as an additional state variable, hence the size of the state-space model is directly proportional to the number of harmonic frequencies represented. Therefore, to have an efficient HSS model, the minimum set of harmonic frequencies required to fully represent a power electronic circuit while still providing an acceptable accuracy must be determined.

There are two steps for system reduction for an HSS model of a power electronic circuit; the first is a truncation of all harmonic frequencies above a predetermined harmonic order, such that a periodic signal $x(t)$ is represented by a finite dimensioned vector of its Fourier coefficients with a length of $2h+1$, where h is the highest order of harmonic. The second step is to further reduce the system size by only keeping the harmonics required to fully represent the frequency cross-coupling characteristic of the power electronic circuit. Given that most time-periodic signals exhibit the property of high frequency roll-off and power electronic circuits are often set up with filters to reduce high frequencies, any time-periodic signals can be approximated by a Fourier series truncated to a relatively high harmonic order.

The harmonic truncation introduces errors in the waveforms, which is particularly significant at discontinuities of piecewise functions; this error is known as the *Gibbs phenomenon*. It is

important to note that the absence of higher harmonic orders due to truncation does not only affect the high frequency transfers but also low frequency transfers due to matrix inversion. This was discussed extensively in [Love 2007] and is not repeated here.

The truncated set of harmonics can be further refined to keep the minimum set of harmonic frequencies required to fully represent a power electronic circuit, more specifically, the minimum set of harmonics must fully represent the frequency modulating nature of power electronic circuits. In general, a p-pulse converter modulates the fundamental frequency to generate $pn \pm 1$ harmonics on the ac side known as the *characteristic harmonics*, and they are coupled to pn harmonics on the dc side. Thus, it is sufficient to fully capture the frequency modulation of a power electronic circuit with its characteristic harmonics or with any set of harmonics that are p harmonics apart on both sides of the converter. For example, an HSS model of a 6-pulse converter requires $[1, 5, 7, 11, 13, ...]$ harmonics and $[0, 6, 12, 18, 24, ...]$ harmonics to be modelled on the ac side and the dc side respectively.

3.12 SWITCHING INSTANT VARIATION

Traditionally, thyristors have been commonly used in power electronic applications due to their high current ratings. A thyristor is a semi-controlled switch, i.e. its switch-on instant is determined by a control algorithm, but its switch-off instant cannot be predefined; it continues to conduct until its current stops flowing. Insulated-gate bipolar transistors (IGBTs) have become increasingly popular in modern power electronic applications due to their ability to define their switch-off instant through control, thus an IGBT is a fully controlled switch. Regardless the type of switch used in the power electronic circuit, variation in their switching instants is a common phenomenon and must be modelled correctly. As this thesis is focused on a conventional HVdc configuration, only thyristors are considered for the rest of the thesis.

Switching instant variation (SIV) was first described in [Wood 1993] as the commutation period variability of an HVdc converter. Wood discussed the effect of current distortion on the dc side, voltage distortion on the ac side, and firing angle variation on the commutation period of the converter. He concluded that the related effects were nonlinear in frequency domain, but linearisable in small-signal analysis. Hume then investigated the contribution of SIV to the nonlinearity of the HVdc converter [Hume 2002]. He examined the convergence of the end of commutation period using Newton's method with a single iteration and confirmed that the switching instants of the converter can be solved accurately using direct linearised analytic equations. Later, Love identified two types of SIV, the *autonomous switching instant variation* and the *controlled switching instant variation* [Love 2007], and more recently, Orillaza *et al.* published the first set of HSS models of power electronic circuits (a three-phase TCR and an HVdc converter) incorporating the effects from both types of SIV [Orillaza *et al.* 2010]. SIV is a

result of variations in the base case quantities, and its effects are nonlinear in frequency domain. Therefore to incorporate the phenomenon into the linear context of HSS, the relationships must be linearised around the base case operating point.

Autonomous SIV is the product of a variation in a system electrical input. For example, in a linearised small-signal model, the current through the thyristor beyond the base case switch-off instant is expected to be zero. Any residual current beyond this point is evidence of an incorrect model; the thyristor current must be set to zero at the base case switch-off instant. Similarly, controlled SIV occurs in the presence of disturbance in the control signal at the base case switch-on instant of the thyristor. To implement a model of SIV in the HSS framework, amplitude modulated impulse trains (AMITs) are used to reset or modify signal waveforms, and because the impulses are introduced at the base case switching instants, this method is linear time-periodic. The exact procedure is discussed in the following chapters in the context of an HVdc converter.

3.13 SYMMETRICAL COMPONENTS

The method of symmetrical components was first introduced in [Fortescue 1918], and it was developed during an investigation to the operation of an induction motor under unbalanced conditions. Since then, the method of symmetrical components has been extensively used in fault analysis. Any unbalanced three-phase system can be expressed as the sum of a set of three balanced components, specifically, *positive sequence*, *negative sequence*, and *zero sequence* as defined in definition 7.

Definition 7 (Symmetrical Components)**.** *Consider a set of three-phase signals, x_a, x_b, and x_c written as a vector,*

$$x_{abc} = \begin{bmatrix} x_a \\ x_b \\ x_c \end{bmatrix} \tag{3.47}$$

There exists a linear transformation which maps the three-phase signals to a set of three balanced components, the relationship is written as

$$\begin{bmatrix} x_p \\ x_n \\ x_z \end{bmatrix} = \begin{bmatrix} 1 & \alpha & \alpha^2 \\ 1 & \alpha^2 & \alpha \\ 1 & 1 & 1 \end{bmatrix} \begin{bmatrix} x_a \\ x_b \\ x_c \end{bmatrix} \tag{3.48}$$

where α is $e^{j\frac{2\pi}{3}}$, and α^2 is $e^{j\frac{4\pi}{3}}$. The subscript p denotes for positive sequence components, a sum of three phasors equal in magnitude but $\frac{2\pi}{3}$ apart with a phase sequence abc as illustrated in Fig. 3.2a. The subscript n denotes for negative sequence components, a sum of three phasors equal in magnitude but $\frac{2\pi}{3}$ apart with a phase sequence acb as illustrated in Fig. 3.2b. The subscript

z denotes for zero sequence, a sum of three phasors equal in both magnitude and phase angle as illustrated in Fig. 3.2c.

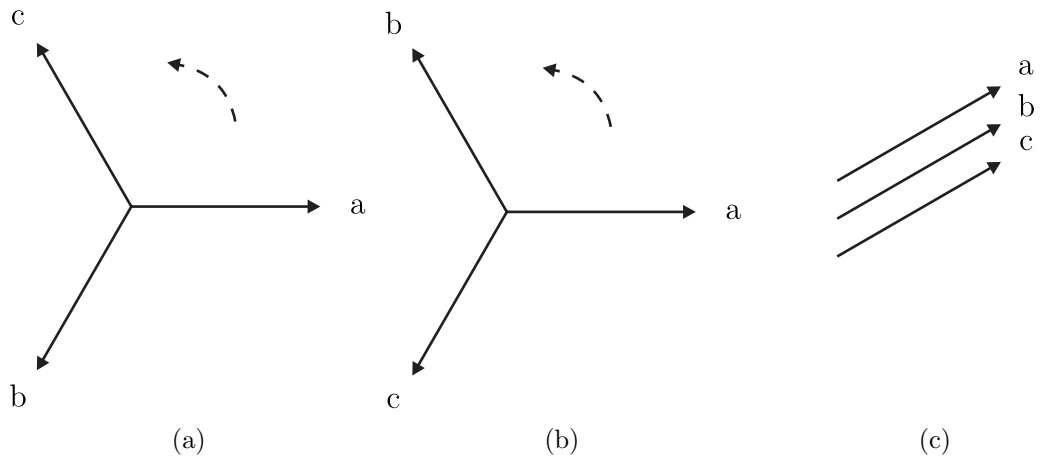

Figure 3.2: Symmetrical components of three-phase phasors: (a) Positive sequence components. (b) Negative sequence components. (c) Zero sequence components.

The same transformation can be applied to each individual harmonic of the three-phase signals. It is shown in [Acha and Madrigal 2001] that the harmonics of orders, $3n+1$, where n is a positive integer, exhibit identical characteristic to a positive sequence fundamental frequency. Similarly, the harmonics of orders, $3n-1$ and $3n$, behave the same as a negative sequence fundamental frequency and a zero sequence fundamental frequency respectively. However, it is important to note that the switching of a 6-pulse converter does not generate even harmonics on the ac side.

Assuming that each harmonic in the truncated list of the ac side characteristic harmonics mentioned in Sec. 3.11 is represented by the sum of two identical complex exponentials (phasors) rotating in the opposite direction on the complex plane, these phasors can be regrouped as symmetrical components. The positive sequence components contain phasors at $[..., -11, -5, 1, 7, 13, ...]$ harmonics, and the negative sequence components contain phasors at $[..., -13, -7, -1, 5, 11, ...]$ harmonics. Although phasors at $[..., -11, -5]$ harmonics technically belong to negative sequence components, but since they are of negative frequency, they behave as positive sequence components; similarly for phasors at $[..., -13, -7]$ harmonics behaving as negative sequence components. Note that for an HVdc system, there is no neutral connection, hence there is no path for zero sequence currents to flow, and thus zero sequence components of such system do not need to be implemented in the model.

For example, a typical transfer on the ac side described using the three-phase representation is written in the form

$$\begin{bmatrix} a \\ b \\ c \end{bmatrix} = \left[\begin{array}{c:c:c} a \leftarrow a & a \leftarrow b & a \leftarrow c \\ \hdashline b \leftarrow a & b \leftarrow b & b \leftarrow c \\ \hdashline c \leftarrow a & c \leftarrow b & c \leftarrow c \end{array}\right] \begin{bmatrix} a \\ b \\ c \end{bmatrix} \tag{3.49}$$

whereas the same transfer written in symmetrical components is in the form

$$\begin{bmatrix} p \\ n \end{bmatrix} = \left[\begin{array}{c:c} p \leftarrow p & p \leftarrow n \\ \hdashline n \leftarrow p & n \leftarrow n \end{array}\right] \begin{bmatrix} p \\ n \end{bmatrix} \tag{3.50}$$

This allows a systematic way to further reduce the size of a three-phase system model. Under the three-phase representation, the same set of harmonic orders on the ac side has to be modelled three times for the three separate phases, but using symmetrical components, the same set of harmonic orders only has to be modelled once to fully represent an equivalent three-phase system. Furthermore, the modulation through the HTF is similar for each harmonic in the same symmetrical component, for example, all positive sequence components modulate in the same way to couple with the dc side harmonics, and likewise all negative sequence components modulate in the same way to couple onto the harmonics that exist on the dc side.

3.14 CONCLUSIONS

In this chapter, the formulation of the HSS framework has been described through the use of *frequency separation* and *harmonic balance* techniques. The HSS is an ideal framework for the modelling of LTP systems which is also applicable for a power electronic converter model that is linearised around an operating point.

The HSS has the ability to track harmonics of an LTP system in the steady-state and under transient conditions with its EMP basis signal. By posing the LTP system as an LTI equivalent using s-domain state-space equations, the dynamic behaviour of the system can be analysed through techniques such as pole-zero maps and root-locus. Furthermore, each harmonic of the state variable is explicitly represented as an additional state variable, this grants the opportunity to fully capture the frequency cross-coupling nature of power electronic circuits across a wide range of frequencies as opposed to a *dynamic phasor* or a *generalised state-space averaging* model where only the fundamental frequency is modelled. In addition, incorporating a range of harmonics in the model allows the ability to observe the effect of a system resonance from a number of reference frames; an example is presented in a succeeding chapter.

The effects of SIV in a linearised model of a power electronic circuit has been described, and a modelling approach through the use of AMIT is briefly introduced. This is an important step to the correct representation of the system. System reduction through frequency truncation and only including the characteristic harmonics of the power electronic circuit ensures an efficient digital model. In the next chapter, a linearised small-signal model of an uncontrolled HVdc converter is developed using the HSS formulation.

Chapter 4

HARMONIC STATE-SPACE MODEL OF AN UNCONTROLLED HVDC CONVERTER

4.1 INTRODUCTION

The HVdc converter is known to be a nonlinear and time-variant circuit because its associated thyristor switching instants (both switch-on and switch-off instants) are subjected to change upon a signal variation at its electrical or control input. A nonlinear and time-variant power electronic circuit can be linearised and posed as a time-invariant system model in complex frequency domain around a predetermined operating point if the perturbations to the system inputs are assumed to be relatively small. This leads to the objective of this chapter, to analytically develop a linearised uncontrolled HVdc converter model.

Linearisation in the frequency domain through small-signal modelling has been adopted by many researchers to produce a linearised model of the HVdc converter but most of them are limited to the steady-state. Persson was perhaps the first to publish a linearised s-domain HVdc converter model which incorporates firing angle variation due to the dc side current control, but lacked a description of the commutation period variation [Persson 1970]. Later, Sakui published a number of analytical models of an uncontrolled bridge rectifier based on switching functions in [Sakui *et al.* 1985], [Sakui *et al.* 1989], and [Sakui and Fujita 1992]. Similarly, Hu and Yacamini published a model of the HVdc converter with fixed firing angle and commutation period in [Hu and Yacamini 1992]. Then in 1995, Wood and Arrillaga published a frequency domain model of a controlled HVdc converter that incorporated commutation period variation into the converter switching function [Wood and Arrillaga 1995b]. This was the first model that fully captured the effects associated with switching instant variation (SIV).

Since then, frequency domain analysis of the converter has been extended to capture its dynamic behaviour under transient conditions. In 2003, Osauskas and Wood published a controlled HVdc converter model based on the popular *dynamic phasor* technique which describes the transient evolution of the fundamental component [Osauskas and Wood 2003]. More recently, Vyakaranam published a number of dynamic models of FACTS devices in [Vyakaranam *et al.* 2010] using

the extended harmonic domain (EHD) which is equivalent to the harmonic state-space (HSS). This work was a great contribution in terms of its extensive coverage, but none of the models presented incorporated control dynamics. In 2007, Love published the first HSS model of the HVdc converter [Love 2007], but again this model did not incorporate any form of feedback control. This leads to the work presented in this chapter.

This chapter presents a small-signal HVdc converter model with fixed and equidistant firing pulses accommodated by the HSS framework that was introduced in Chapter 3. This model accurately describes the frequency coupling of the converter in the steady-state and also under transient conditions. The model has to manage some state variables, the current through the commutation circuits and the dc side current, so that they maintain the correct values in the presence of switching instant variation. The discussion begins with the derivation of the transfers required to generate the base case waveforms, more specifically, the ac side current spectrum and the dc side voltage spectrum resulting from the base case three-phase ac side voltage. The focus then shifts to the derivation of the small-signal transfers required to generate the variation in the ac side current spectrum and the dc side voltage spectrum resulting from perturbations to the electrical inputs of the converter. The small-signal analysis assumes piecewise linearity, therefore summing up all the effects from the transfers describes the overall converter operation.

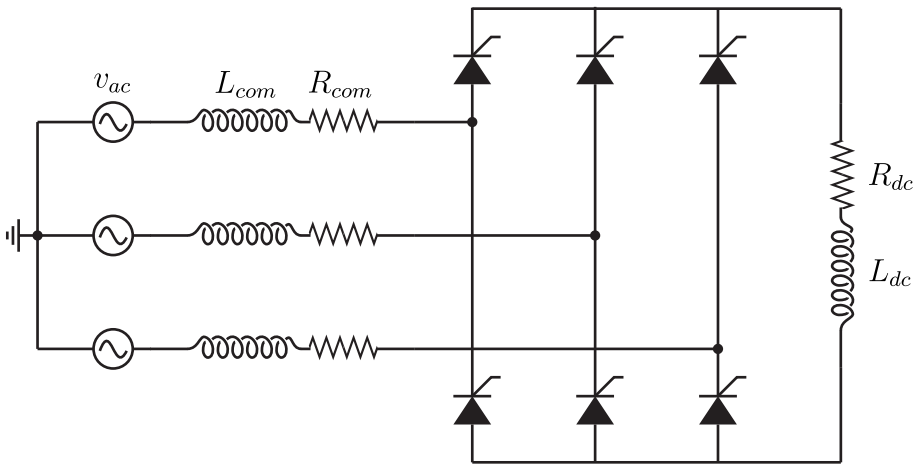

Figure 4.1: Circuit diagram of the HVdc converter model.

The circuit of interest to this study is a heavily simplified version of the widely used *Cigre Benchmark Model for HVDC Controls*. In this HSS HVdc converter model, the usual 12-pulse converter bridge is reduced down to a 6-pulse converter bridge, and limited to the rectifier side of the HVdc link. The nonlinearity of the converter transformer such as core saturation and hysteresis is not included in this model, the converter transformer is simply modelled as its leakage reactance referred to its secondary side, and together with the resistance of the thyristor during its conduction state referred to the ac side of the converter, they form the commutation circuit in this model. The dc side of the converter circuit is modelled as a series impedance consisting of a current smoothing reactor and a resistor which draws the rated current of the

converter. The converter model circuit diagram is shown in Fig. 4.1 while its base case quantities and values of the its components are summarised in Table 4.1.

Table 4.1: Uncontrolled 6-Pulse HVdc Converter Model Specifications

Parameter	Value	Unit
Base Case AC Side Line-to-Line Voltage (v_{ll})	213.4557	kV
Fundamental Frequency (f_0)	50	Hz
Base Case DC Side Voltage (v_{dc})	250	kV
Base Case DC Side Current (i_{dc})	2	kA
Base Case Firing Angle (α_0)	15	deg
Base Case Commutation Period (μ_0)	22	deg
Commutation Circuit Resistance (R_{com})	1	mΩ
Commutation Circuit Inductance (L_{com})	432	mH
DC Side Resistance (R_{dc})	125	Ω
DC Side Inductance (L_{dc})	1	H

4.2 BASE CASE WAVEFORMS

This section details the formulation of the transfer functions required to generate the base case spectra for the ac side current and the dc side voltage. The HSS model of the HVdc converter is linearised around a base case operating point and represented as a time-invariant system in the frequency domain. The ac side current, i_{ac} and the dc side voltage, v_{dc} are generated using transfer functions with fixed frequency spectra. That is, the switching instants of the model are fixed at the base case switch-on instants and the base case switch-off instants which are defined by the base case firing angle, α_0 and the base case commutation period, μ_0.

4.2.1 Base Case AC Side Current Spectrum

Each phase of the base case ac current waveform is a piecewise function of time; it is the sum of three periodic subfunctions each describing a distinct portion of the ac current waveform during a certain interval of time. These time intervals are referred as the *direct conduction period*, the *commutation period*, and the *non-conduction period*. The converter circuit configuration is different for each of these periods based on the switching of its thyristors. Figure 4.2 shows an example of a typical set of converter circuit configurations during these periods.

During the direct conduction period, the current flows from one of the three phases on the ac side through a thyristor to the dc side, and returns to a different phase through another thyristor. Given that the current flows in a direct path, the ac side current must equal the dc side current during the direct conduction period. During the non-conduction period, the associated phase

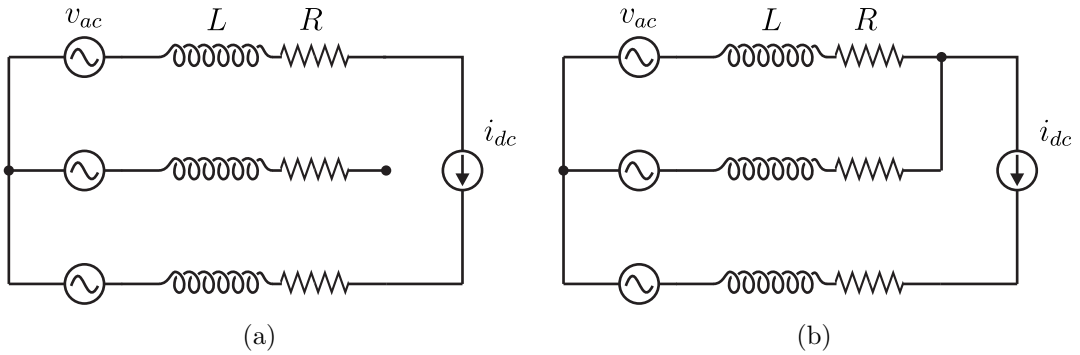

Figure 4.2: Typical HVdc converter circuit configurations: (a) During the direct conduction period and the non-conduction period. (b) During the commutation period.

on the ac side is disconnected from the dc side terminal as its thyristor is fully switched off. A typical converter circuit configuration during these two intervals of time is shown in Fig. 4.2a.

During the commutation period, two phases on the ac side are joined together at the dc side terminal, each carrying a varying portion of the dc side current i.e. the currents in these two phases are varying with time, but they should always sum to the dc side current. This is due to the leakage reactance of the converter transformer (also referred as the commutation reactance) on the ac side limiting the rate of change of ac side current, and thus requiring a finite time (the commutation period) for a phase to be disconnected from the dc side circuit. The current in the phase that is commutating to a non-conduction state is approaching zero while the current in the phase that is commutating to a direct conduction state is approaching the dc current. A typical converter circuit configuration during the commutation period is shown in Fig. 4.2b.

With no variation to the base case quantities i.e. steady fundamental ac side voltage, dc side current, and the thyristor firing angle, the voltage across the commutation reactance is the only variable that has a contribution towards the rate of change of ac side current during the commutation period. The commutation process is governed a first-order ordinary differential equation (ODE) written as

$$\frac{di_{ac_\phi}(t)}{dt} = \frac{-R}{L} i_{ac_\phi}(t) + \frac{1}{L} v_{com_\phi}(t) \tag{4.1}$$

where v_{com_ϕ} is the voltage drop across the commutation reactance (L) in a commutating phase, inducing a rate of change of the ac current (i_{ac_ϕ}) flowing in the same phase. R is the relatively small forward resistance of the thyristors referred to the ac side commutation circuit.

Equation in (4.1) can be transformed to the state dynamic equation describing the ac side commutation circuit with its current posed as the state variable. Applying the HSS formulation, and selecting the state variable as the output, the HSS equations to the commutation circuit is

written as

$$sI_{ac_\phi} = \left(\frac{-R}{L}\mathcal{I} - \mathcal{N}\right) I_{ac_\phi} + \frac{1}{L}\mathcal{I}V_{com_\phi} \tag{4.2}$$

$$Y = \mathcal{I}I_{ac_\phi} + \mathcal{D}V_{com_\phi} \tag{4.3}$$

where in this case, the feed-forward matrix ($\mathcal{D}$) is a zero matrix.

The voltage applied across the commutation circuit in any single phase is strictly confined within the commutation period, and sampling of the ac side voltage waveforms during the commutation period is required to generate this voltage spectrum. The *describing function* technique (also referred as switching function in this thesis) has been adopted for this purpose. A switching function describes the switching pattern of the thyristor bridge where values of ± 1, $\pm\frac{1}{2}$, and 0 represents the connection during the direct conduction, the commutation, and the non-conduction periods respectively. In this case, generating the voltage across the commutation circuit requires sampling the three-phase fundamental ac voltages, $v_{ac,1}$, during the base case commutation period. This is written as

$$\begin{aligned} v_{com_\phi}(t) = {} & \Psi^{v_{com}\leftarrow v_{ac}}_{\phi\leftarrow\phi}(t) \cdot v_{ac,1_\phi}(t) \\ & + \Psi^{v_{com}\leftarrow v_{ac}}_{\phi\leftarrow\phi+\frac{2\pi}{3}}(t) \cdot v_{ac,1_{\phi+\frac{2\pi}{3}}}(t) \\ & + \Psi^{v_{com}\leftarrow v_{ac}}_{\phi\leftarrow\phi+\frac{4\pi}{3}}(t) \cdot v_{ac,1_{\phi+\frac{4\pi}{3}}}(t) \end{aligned} \tag{4.4}$$

where $\Psi^{v_{com}\leftarrow v_{ac}}$ are the switching functions required to sample the three-phase ac side voltages during the commutation period.

The commutation process occurs six times during a fundamental interval across the three phases, with four commutations occurring in each phase. Thus the switching functions required to generate the voltage across the commutation circuit in any one phase consist of four pulses in each fundamental cycle with heights of $\frac{1}{2}$ to acquire half of the ac side voltages, and hence half of the ac side line-to-line voltages after summation. The switching functions are written in terms of the base case thyristor switch-on instant, α_0, and the base case commutation period, μ_0, as

$$\begin{aligned} \Psi^{v_{com}\leftarrow v_{ac}}_{\phi\leftarrow\phi}(t) = \frac{2\mu_0}{\pi} + \sum_{m=-\infty}^{\infty} \frac{1}{m\pi} \sin\left(\frac{m\mu_0}{2}\right) \Big[& e^{-jm\left(\omega_0 t + \frac{\pi}{3} + \alpha_0 + \frac{\mu_0}{2} + \phi\right)} \\ & + e^{-jm\left(\omega_0 t + \frac{2\pi}{3} + \alpha_0 + \frac{\mu_0}{2} + \phi\right)} \Big] \end{aligned} \tag{4.5a}$$

$$\Psi^{v_{com}\leftarrow v_{ac}}_{\phi\leftarrow\phi+\frac{2\pi}{3}}(t) = \frac{-\mu_0}{\pi} - \sum_{m=-\infty}^{\infty} \frac{1}{m\pi} \sin\left(\frac{m\mu_0}{2}\right) e^{-jm\left(\omega_0 t + \frac{\pi}{3} + \alpha_0 + \frac{\mu_0}{2} + \phi\right)} \tag{4.5b}$$

$$\Psi^{v_{com}\leftarrow v_{ac}}_{\phi\leftarrow\phi+\frac{4\pi}{3}}(t) = \frac{-\mu_0}{\pi} - \sum_{m=-\infty}^{\infty} \frac{1}{m\pi} \sin\left(\frac{m\mu_0}{2}\right) e^{-jm\left(\omega_0 t + \frac{2\pi}{3} + \alpha_0 + \frac{\mu_0}{2} + \phi\right)} \tag{4.5c}$$

where m is all integers excluding zero while $\phi = 0$, $\frac{2\pi}{3}$, $\frac{4\pi}{3}$ for phase a, b, c respectively, and $\mu_0 = \beta_0 - \alpha_0$ which is the duration of the base case commutation period. For illustration, these switching functions are plotted in Fig. 4.3.

Rewriting the equations in (4.5) in symmetrical components (positive and negative sequences) yields

$$\Psi_{p,n\leftarrow p,n}^{v_{com}\leftarrow v_{ac}}(t) = \frac{\mu_0}{2\pi} + \sum_m \frac{1}{m\pi}\sin\left(\frac{m\mu_0}{2}\right)\Big[e^{-jm\left(\omega_0 t+\frac{\pi}{3}+\alpha_0+\frac{\mu_0}{2}\right)} + e^{-jm\left(\omega_0 t+\frac{2\pi}{3}+\alpha_0+\frac{\mu_0}{2}\right)} - e^{-jm\left(\omega_0 t+\frac{\pi}{3}+\alpha_0+\frac{\mu_0}{2}\right)-s\frac{2\pi}{3}} - e^{-jm\left(\omega_0 t+\frac{2\pi}{3}+\alpha_0+\frac{\mu_0}{2}\right)-s\frac{4\pi}{3}}\Big] \tag{4.6}$$

where m is $[..., -12, -6, 0, 6, 12, ...]$ for the transfers from and to the same sequence. For transfers from the positive sequence to the negative sequence and the other way around, m is $[..., -14, -8, -2, 4, 10, ...]$ and $[..., -10, -4, 2, 8, 14, ...]$ respectively. $s = +1$ for transferring ac side voltages in positive sequence, and $s = -1$ for transferring ac side voltages in negative sequence.

Figure 4.4a is a plot of the voltages across the commutation reactance in each phase, generated by multiplying the ac side voltage at fundamental frequency with the switching functions, $\Psi^{v_{com}\leftarrow v_{ac}}$, and Fig. 4.4b plots the base case waveforms of the three-phase ac currents. The ac side waveforms are truncated to the 49^{th} harmonic while its associated transfers from the ac side are truncated to the 98^{th} harmonic.

4.2.2 Base Case DC Side Voltage Spectrum

In this section, the derivation of the switching function required to generate the base case dc side voltage spectrum from the base case quantities is discussed. The dc side voltage is defined as the potential difference between the dc side terminals of the converter, and it is coupled to the ac side voltage through the converter. Thus the dc side voltage waveform is a summation of the sampled three-phase ac side voltage waveforms. Much like the ac side current waveforms, the dc side voltage waveform is also a piecewise function of time. In this case, the dc side voltage waveforms consists of two periodic subfunctions each describing its waveform during a particular interval of time, more specifically, the direct conduction period and the commutation period.

During the direct conduction period, the dc side terminals are connected to two ac side phases through the converter. Therefore the dc side voltage is equal to the ac side line-to-line voltage during this interval. During the commutation period, the two commutating phases on the ac side are connected together at the dc side terminal, and assuming the commutation reactances on the ac side are balanced in all three phases, the voltage at this common node is exactly halfway between the two corresponding line-to-ground voltages of the two commutating phases.

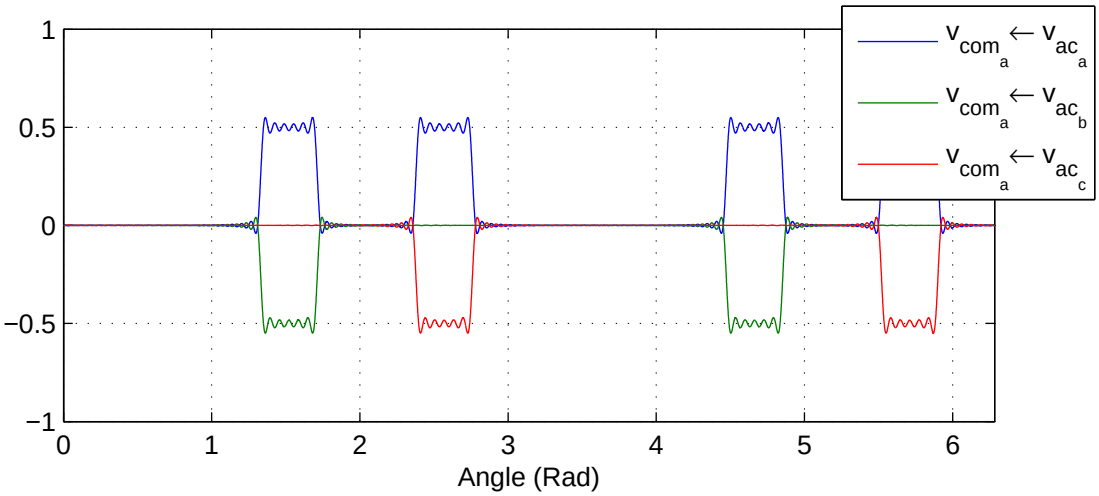

(a) Switching functions for generating the voltage across the commutation circuit in phase a.

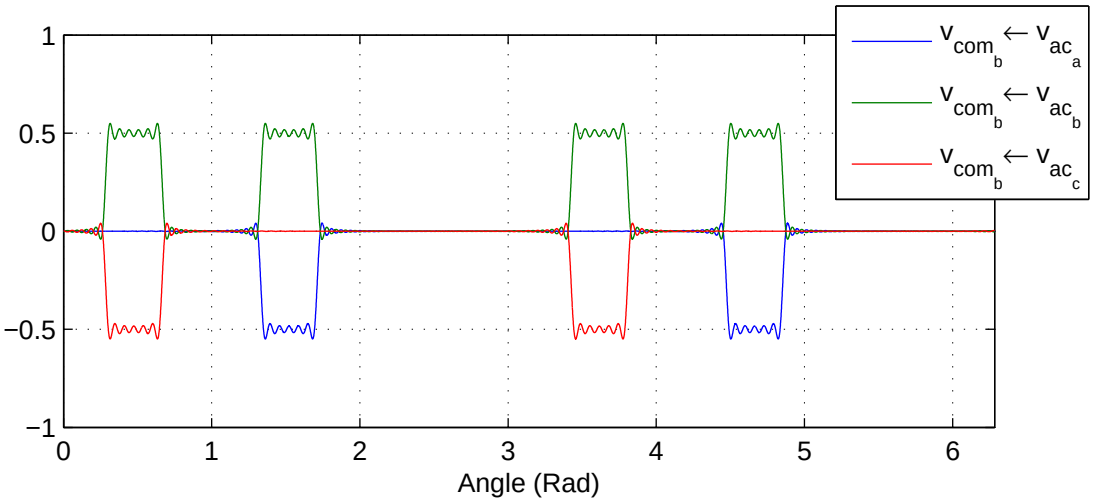

(b) Switching functions for generating the voltage across the commutation circuit in phase b.

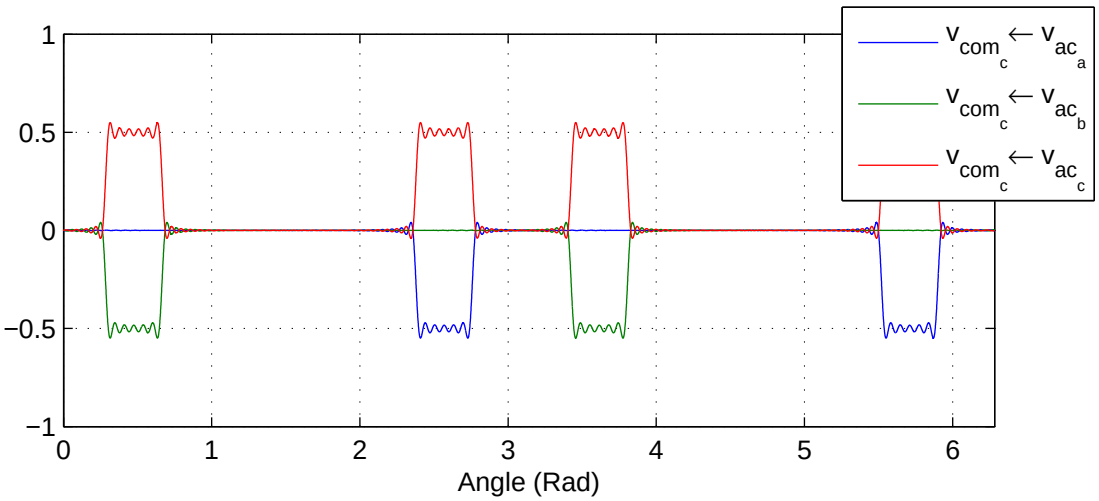

(c) Switching functions for generating the voltage across the commutation circuit in phase c.

Figure 4.3: Switching functions for transferring the three-phase ac side voltage, $v_{ac,1}$, to the voltage across the commutation circuit, v_{com}.

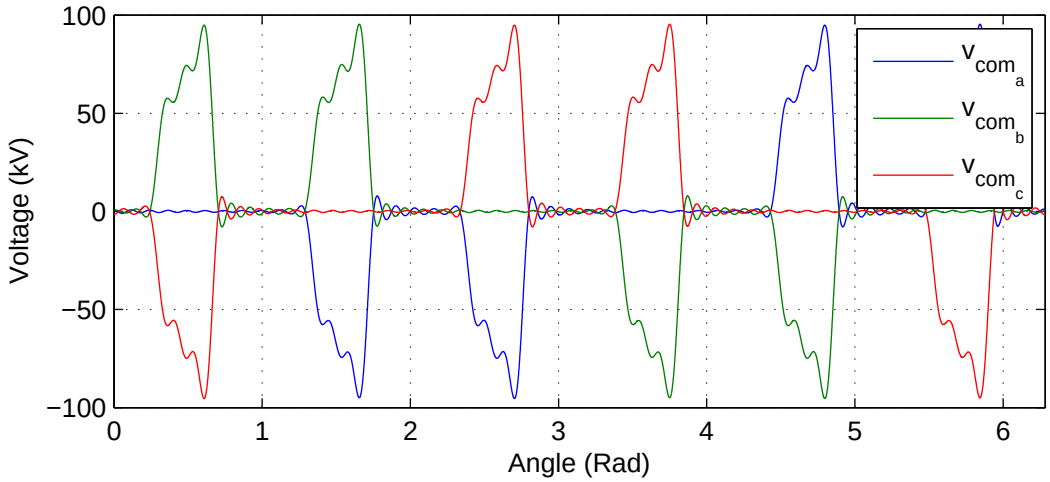

(a)

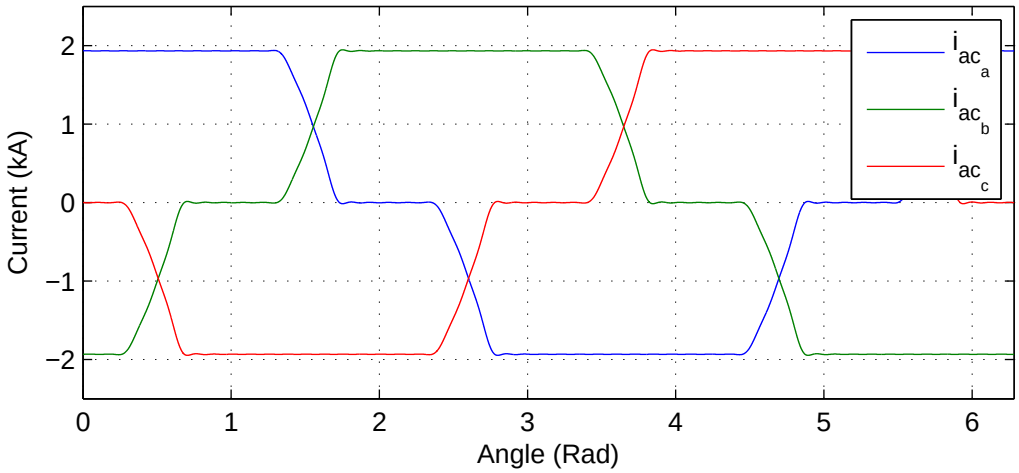

(b)

Figure 4.4: Base case ac side waveforms: (a) The voltage across the commutation circuit in each phase. (b) The base case ac side current waveforms.

Thus, the overall switching pattern can be described by the sum of two switching functions where one switching function represents the ac side to dc side thyristor bridge connection during the direct conduction period while the other switching function represents the ac side to dc side thyristor bridge connection during the commutation period. Finally, the base case dc side voltage waveform can be generated by multiplying the base case fundamental ac side voltage by the overall switching function and summed over the three phases, this can be written as

$$v_{dc}(t) = \sum_{\phi} \left(\Psi^{v_{dc} \leftarrow v_{ac}}_{direct_{\phi}}(t) + \Psi^{v_{dc} \leftarrow v_{ac}}_{commutation_{\phi}}(t) \right) v_{ac,1_{\phi}}(t) \tag{4.7}$$

where $\phi = 0, \frac{2\pi}{3}, \frac{4\pi}{3}$ for phase a, b, c respectively.

The two switching functions in (4.7) are dependent on the base case switch-on instants and

the base case switch-off instants. During the direct conduction period, the associated switching function has rectangular sampling pulses of height 1 for the positive half of the fundamental cycle, and -1 for the negative half of the fundamental cycle. This switching function can be written as

$$\Psi^{v_{dc}\leftarrow v_{ac}}_{\phi,direct}(t) = \sum_{m=-\infty}^{\infty} \frac{2}{m\pi} \sin\left(\frac{m\pi}{3}\right) e^{-jm(\omega_0 t+\alpha_0+\phi)} \tag{4.8}$$

where m is all integers excluding zero. During the commutation period, the associated switching function has rectangular sampling pulses of height $\frac{1}{2}$ for the positive half of the fundamental cycle, and $-\frac{1}{2}$ for the negative half of the fundamental cycle. This can be written as

$$\Psi^{v_{dc}\leftarrow v_{ac}}_{\phi,commutation}(t) = \sum_{m=-\infty}^{\infty} \frac{2}{m\pi} \sin\left(\frac{m\mu_0}{2}\right) \sin\left(\frac{m\pi}{3}\right) e^{-jm\left(\omega_0 t+\alpha_0+\frac{\mu_0}{2}+\phi\right)-j\frac{\pi}{2}} \tag{4.9}$$

where m is all integers excluding zero, and $\mu_0 = \beta_0 - \alpha_0$. Rewriting (4.8) and (4.9) using symmetrical components yields

$$\Psi^{v_{dc}\leftarrow v_{ac}}_{d\leftarrow p,n_{direct}}(t) = \sum_{m} \frac{2}{m\pi} \sin\left(\frac{m\pi}{3}\right) e^{-jm(\omega_0 t+\alpha_0)} \tag{4.10}$$

$$\Psi^{v_{dc}\leftarrow v_{ac}}_{d\leftarrow p,n_{commutation}}(t) = \sum_{m} \frac{2}{m\pi} \sin\left(\frac{m\mu_0}{2}\right) \sin\left(\frac{m\pi}{3}\right) e^{-jm\left(\omega_0 t+\alpha_0+\frac{\mu_0}{2}\right)-j\frac{\pi}{2}} \tag{4.11}$$

where $m = [..., -13, -7, -1, 5, 11, ...]$ for the transfer from positive sequence ac side voltage to the dc side voltage, and $m = [..., -11, -5, 1, 7, 13, ...]$ for the transfer from negative sequence ac side voltage to the dc side voltage. Figure 4.5a is a plot of both switching functions for the direct conduction period and the commutation period summed together while Fig. 4.5b shows the base case dc side voltage waveform resulting from the equation in (4.7). The dc side voltage waveform is truncated to the 48^{th} harmonic while its corresponding switching function from the ac side voltage is truncated to the 97^{th} harmonic.

4.3 TRANSFERS AROUND THE BASE CASE OPERATING POINT

In a small-signal analysis, small-signal variations are introduced at the system inputs, causing the operating point to vary about its base case operating point, and induces changes to its associated waveforms. The variation in the operating point has to be kept small, and more importantly its trajectory from the base case operating point to the new conditions has to be linear. This is the key feature of a linearised model, and allows the use of the base case operating point to approximate the behaviour of the system upon small-signal variations. The effects of the ac side voltage and the dc side current perturbations are described separately, and the overall converter model is simply the sum of all the effects resulting from every perturbation at the system inputs.

In this section, the small-signal linearised transfers for an uncontrolled HVdc converter are

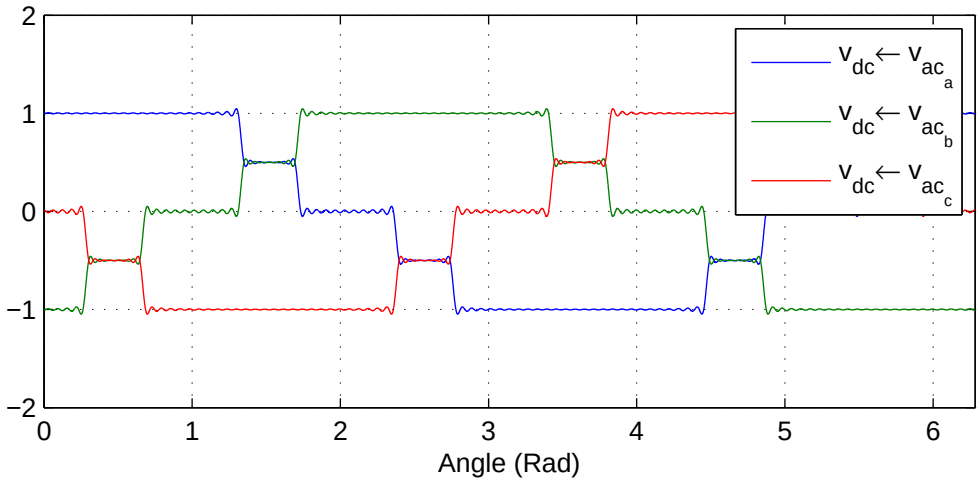

(a)

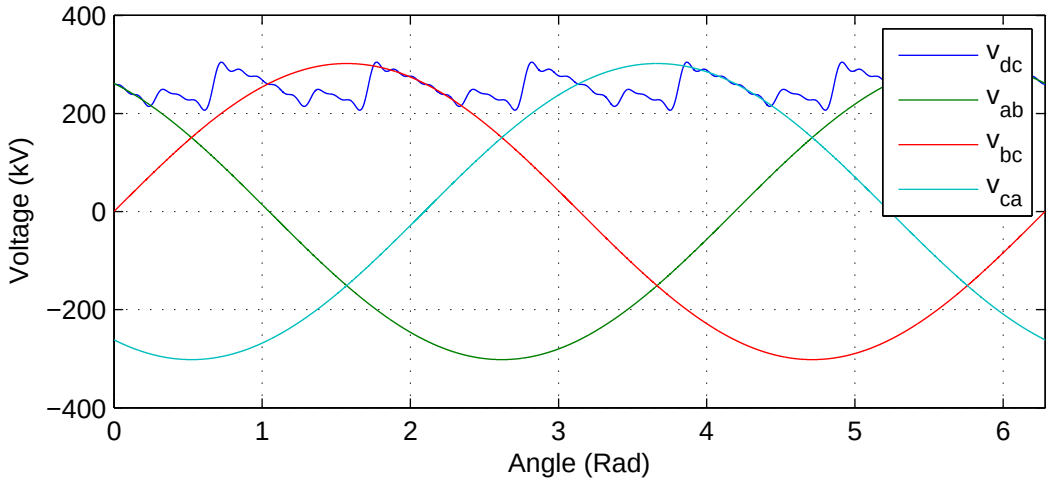

(b)

Figure 4.5: Base case dc side waveforms: (a) The switching functions required to sample the ac side voltage waveforms for the dc side voltage waveform. (b) The base case dc side voltage waveform.

derived. More specifically, the transfers from a small-signal ac side voltage variation to the ac side current and the dc side voltage, and the transfers from a small-signal dc side current variation to the ac side current and the dc side voltage. Due to the small-signal variations on system inputs, the system experiences *switching instant variation* (SIV), thus its associated effects must be implemented in the model for a correct representation of the system. The method of incorporating SIV in the HSS model is presented in the upcoming sections. Note that the dc side current is assumed to be an external input to the system during the derivation of the small-signal transfers, however, it is eventually replaced by the current flowing through the dc side circuit. The dc side circuit receives the voltage across the dc side terminals of the converter as an input and generates the dc side current and its derivative as outputs which are coupled

back to the ac side through their associated small-signal transfers.

4.3.1 Small-Signal AC Side Current Spectrum

In an uncontrolled HVdc converter circuit, the small-signal ac side current, Δi_{ac}, receives contributions from two input variables, the small-signal ac side voltage, Δv_{ac}, and the small-signal dc side current, Δi_{dc}. Given that the circuit is linearised around a base case operating point, the contribution from the two independent input variables can be examined independently.

A small variation in the base case ac side voltage produces a small change to the voltage across the commutation circuit, causing a slight increase or decrease in the rate at which the ac side current rises to the base case dc side current level or falls to zero level. This changes the length of the commutation period from its base case condition, and therefore a direct cause of SIV. Similarly, a small variation in the base case dc side current has an effect on the ac side current value at the start of the commutation off process and the final ac side current value at the end of the commutation on process; it changes the time required to complete the commutation process. This is again a source of SIV. Given that the firing angle is fixed in this open-loop converter model, the SIV resulting from small-signal injections is strictly associated with the end of the commutation period.

4.3.1.1 AC Side Voltage Variation

The effect that a small-signal ac side voltage injection has on the ac side current spectra is confined to the commutation period. The ac side current spectrum is not directly affected by the ac side voltage injection during the direct conduction period where it must equal to the current flowing on the dc side, and similarly in the non-conduction period where the ac side current must be zero. It is clear that the ac side voltage transferred to the dc side does have a consequential effect on the dc side current, which is dealt with by the dc side state variable equation set when a dc side inductor is connected.

The transfer from the small-signal ac side voltage to the associated small-signal voltage across the commutation circuit can be described by the base case switching function in (4.4), and the same approach is used to generate the resulting small-signal ac side current spectra where the switched small-signal ac side voltage serves as the input to state-space equations of the ac side commutation circuit in (4.2). The only difference is that this small-signal transfer to the ac current spectra must incorporate the effect of SIV.

Figure 4.6 demonstrates the exaggerated effect of SIV on a linearised converter model with its switching instants fixed at the base case values. The solid black line represents the base case ac side current, i_{ac}, during a portion of the fundamental period, while the thick dashed line

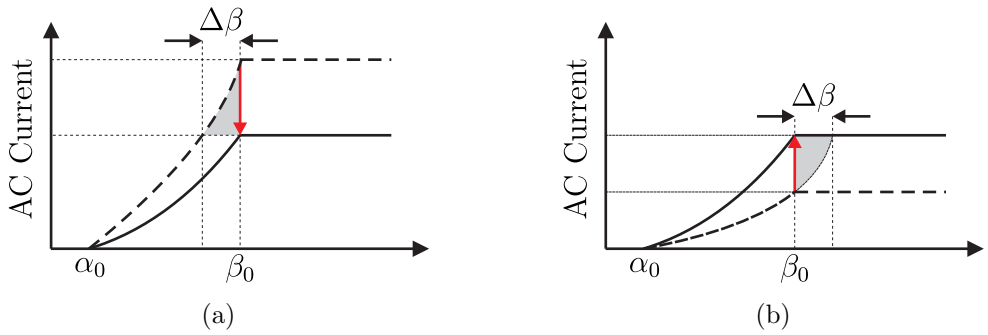

Figure 4.6: Graphical illustration of the consequences associated with an autonomous SIV on the ac side current waveform: (a) The end of commutation period is brought forward in time. (b) The end of the commutation period is postponed in time.

represents the sum of the base case ac side current with the small-signal ac side current, Δi_{ac}, resulting from an ac side voltage injection. The thin dashed lines illustrate the SIV at the end of the commutation period, and the shaded region represents the incorrect current-time[1] area caused by this SIV if the perturbed ac side current is reset at the base case thyristor switch-off instant indicated by the red arrow.

As the small-signal injection increases (or decreases) the ac side voltage and consequently the voltage across the commutation circuit, the ac side current rises (or falls) at a faster (or slower) rate during the commutation period compared to its base case waveform. Thus the ac side current exceeds (or does not reach) the base case dc side current (or zero) at the end of the base case commutation period, and results in an incorrect current-time area in its waveform. If the ac side current is reset to the correct condition at the end of every commutation period, i.e. the ac side current is reset to the dc side current at the beginning of every direct conduction period, and it is also reset to zero at the beginning of every non-conduction period, then the only incorrect current-time area is the shaded region shown in Fig. 4.6.

This current-time area is referred as the *indirect area* in [Hume 2002]. Hume states that both the horizontal and vertical dimensions of the indirect area are proportional to the small-signal injection, and thus the area is proportional to the square of the voltage injection. This linearised model must exclude this higher order effect. The current-time area is important in harmonic or HSS studies as the conversion of a waveform to its spectrum always involves its integration. As long as the ac side current can be reset to its correct value at the end of each commutation period, the model will be an accurate linearisation of the HVdc converter characteristics. For example, in Fig. 4.6a, the ac side current should be reset downwards to the dc side current at β_0, whereas in Fig. 4.6b, the ac side current should be reset upwards to the dc side current at β_0.

[1] All of the integrating operations presented in this thesis were performed with time, hence the current-time area. If the integrations were performed with angle then the operation calculates a current-angle area.

In the HSS framework, any current flowing through an inductor is represented by a state variable, similarly any voltage measured across a capacitor is also represented by a state variable. Each state variable is governed by a state dynamic equation, thus it is not possible to assign its value at any instant in time. In order to reset a state variable, in this case the ac side current, a voltage must be applied across the commutation circuit, and in this thesis, an *area modulated impulse train* (AMIT) spectrum is used to achieve that.

The AMIT spectrum is equivalent to a *Dirac comb* or a *sampling function*. In the frequency domain, the AMIT spectrum does not exhibit the high frequency roll-off property as other common periodic waveforms, which could be a source of error due to the frequency truncation, but the immediate integration of the AMIT spectrum by the commutation circuit reduces the dependence on its high frequency components for an accurate model since an integrator behaves like a low-pass filter. The AMIT spectrum can be described as

$$\delta(t) = \frac{1}{T} + \sum_{m=-\infty}^{\infty} \frac{1}{T} e^{-jm(\omega_0 t + t_1)} \tag{4.12}$$

for an periodic impulse placed at time t_1, where m is all integers excluding zero, and T is the fundamental period.

The AMIT spectrum is used to sample the perturbed small-signal ac side current at the end of the base case commutation period, β_0, and converts the sample to a voltage impulse with the correct voltage-time area. The voltage impulse is applied across the commutation circuit at that same instant in time, which induces a step in the ac side current waveform to reset it to the correct condition. Since a voltage impulse is infinitely tall and narrow, the associated voltage drop across the resistive component of the commutation circuit can be assumed to be zero, therefore the voltage impulse appears across the commutation reactance only. The approach can be described by the block diagram in Fig. 4.7. This updates the first order ODE in (4.1) to

$$\frac{di_{ac_\phi}(t)}{dt} = \left[\frac{-R}{L} + \frac{K_d \delta(t)}{L}\right] i_{ac_\phi}(t) + \frac{1}{L} v_{com_\phi}(t) \tag{4.13}$$

where K_d is a constant required to convert the current samples to voltage impulses.

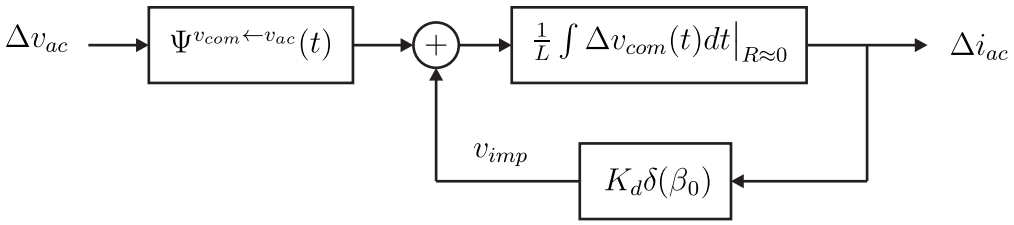

Figure 4.7: The AMIT feedback loop is a method to reset the ac side current to the correct condition.

Strictly speaking, a waveform with steps can not be defined at the instant of the step, it can

be anywhere between the initial value of the step and the final value of the step. However, a frequency truncation to a stepped waveform makes it defined everywhere as shown in Fig. 4.8. The step in the waveform along with the ringing associated with frequency truncation means that the sample made at the step instant is not at the desired value. For example, if a frequency truncated periodic switching function is sampled at the instant it steps, the sampled value would be exactly half of the step size. This is because the ringing on both side of the step are of equal magnitude, i.e. the function exhibits half-wave symmetry. Figure 4.8 illustrates a frequency truncated waveform stepping 1 unit at time t_1 results in a sample of $\frac{1}{2}$ unit at t_1.

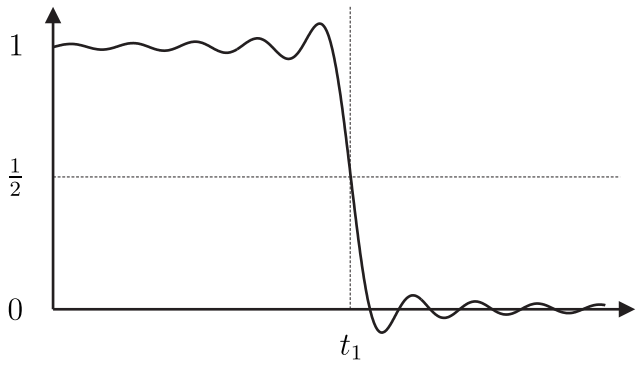

Figure 4.8: Sampling at a step results half of the desired value.

Therefore in this particular case of sampling the small-signal ac side current, and generating appropriately scaled voltage impulses from the current samples to reset the small-signal ac side current to zero, the associated constant K_d required can be determined by the following calculations. For any given phase, the voltage impulse resulting from a ac current sampled at β_0 is written as

$$\begin{aligned} v_{imp}(t) &= K_d \delta(t-\beta_0) i_{ac}(t) \\ &= K_d i_{ac}(\beta_0) \delta(t-\beta_0) \end{aligned} \tag{4.14}$$

and the current step generated by applying this voltage impulse across the commutation reactance is given by

$$\begin{aligned} i_{v_{imp}}(t) &= \frac{1}{L} \int K_d i_{ac}(\beta_0) \delta(t-\beta_0) dt \\ &= \frac{K_d i_{ac}(\beta_0)}{L} H(t-\beta_0) \end{aligned} \tag{4.15}$$

where $H(t-\beta_0)$ is a Heaviside step function. Given that the sample is midway between the

initial and final values of the step,

$$\begin{aligned} i_{v_{imp}}(\beta_0) &= \frac{K_d i_{ac}(\beta_0)}{2L} \\ K_d &= 2L\frac{i_{v_{imp}}(\beta_0)}{i_{ac}(\beta_0)} \\ &= -2L \end{aligned} \tag{4.16}$$

since the ratio between $i_{v_{imp}}(\beta_0)$ and $i_{ac}(\beta_0)$ is designed to be -1.

There are four commutations in any given phase in a 6-pulse converter, therefore the AMIT spectrum in each phase requires four sampling impulses at the base case end of commutation instants, β_0. Each impulse has a voltage-time area of unity so that when it is modulated by the mismatch in ac side current at the end of the base case commutation period, $\Delta i_{ac}|_{\beta_0}$, and integrated by the commutation reactance circuit, it corrects the mismatch and ensures zero current beyond the base case thyristor switch-off instants.

Each commutation process is associated with two phases on the ac side, one phase is commutating to the direct conduction state while the other phase is commutating to the non-conduction state, and they must complete the commutation process at the same instant. Therefore for any SIV observed in one of the commutating phases, its associated effects must also be present in the other commutating phase, i.e. an ac side current overshooting the target dc side current at the end of the base case commutation period means that the current in the other commutating phase overshoots its target zero current in the negative direction.

Due to the *Gibbs phenomenon* from harmonic truncation, sampling both currents in the two commutating phases separately may introduce unequal voltage impulses on the two commutating phases and cause a discrepancy between the offsets in the two commutating currents at the end of the commutation period. Sampling one of the two commutating phases and applying the negative of the sample to the other commutating phase ensures equal voltages across the two commutating reactances. That is, the samples of the small-signal ac side current mismatch should be obtained from either the phase that is commutating to a direct-conduction period or the phase that is commutating to a non-conduction period at the base case end of commutation instant β_0 as labelled in Fig. 4.9. Thus this approach requires only two sampling impulses per phase separated by π, the associated impulse train in symmetrical components can be written as

$$\delta_{p,n\leftarrow p,n}(t) = \sum_m \frac{1}{T}\left[e^{-jm(\omega_0 t+\beta_0)} + e^{-jm(\omega_0 t+\beta_0+\pi)}\right] \tag{4.17}$$

where m is $[..., -12, -6, 0, 6, 12, ...]$ for the transfers from and to the same sequence. For transfers from the positive sequence to the negative sequence and the other way around, m is $[..., -14, -8, -2, 4, 10, ...]$ and $[..., -10, -4, 2, 8, 14, ...]$ respectively. The corresponding FTM for

the AMIT can be written as

$$\Delta_{\beta_0} = \frac{1}{T}\left[\mathcal{T}\{e^{-jm(\beta_0)}\} + \mathcal{T}\{e^{-jm(\beta_0+\pi)}\}\right] \tag{4.18}$$

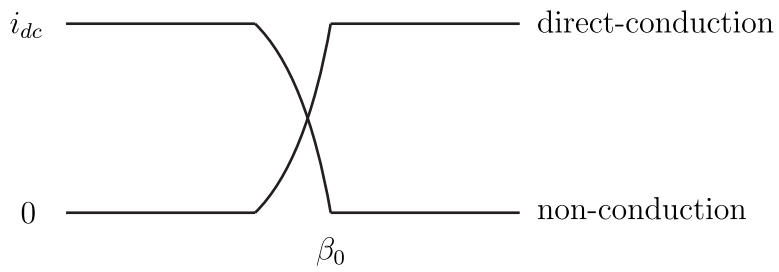

Figure 4.9: The base case instants at the end of the commutation period.

Given that there are two impulses associated with any phase, two more impulses are generated for either the previous or the subsequent phase. If the commutating on phase was sampled then the two generated impulses are for the previous phase, and similarly if the samples are of the commutating off phase then the two generated impulses are for the subsequent phase. The transfer to generate voltage impulses for the commutating on phases from the samples of the commutating off phase at β_0 can be described as a matrix multiplication such that

$$\begin{bmatrix} v_{a,\text{on}}(t) \\ v_{b,\text{on}}(t) \\ v_{c,\text{on}}(t) \end{bmatrix} = \begin{bmatrix} 0 & 0 & -1 \\ -1 & 0 & 0 \\ 0 & -1 & 0 \end{bmatrix} \cdot \begin{bmatrix} v_{a,\text{off}}(t) \\ v_{b,\text{off}}(t) \\ v_{c,\text{off}}(t) \end{bmatrix} \tag{4.19}$$

Note that this is only a phase interchanging operation, it does not alter the phase sequence nor does it frequency shift. Similarly, the transfer to generate voltage impulses for the commutating off phases from the samples of the commutating on phases at β_0 can be described as

$$\begin{bmatrix} v_{a,\text{off}}(t) \\ v_{b,\text{off}}(t) \\ v_{c,\text{off}}(t) \end{bmatrix} = \begin{bmatrix} 0 & -1 & 0 \\ 0 & 0 & -1 \\ -1 & 0 & 0 \end{bmatrix} \cdot \begin{bmatrix} v_{a,\text{on}}(t) \\ v_{b,\text{on}}(t) \\ v_{c,\text{on}}(t) \end{bmatrix} \tag{4.20}$$

Rewriting the transfers in (4.19) and (4.20) in symmetrical components yields

$$\begin{bmatrix} v_{p,\text{on}}(t) \\ v_{n,\text{on}}(t) \\ v_{z,\text{on}(t)} \end{bmatrix} = \begin{bmatrix} -e^{+j\frac{2\pi}{3}} & 0 & 0 \\ 0 & -e^{-j\frac{2\pi}{3}} & 0 \\ 0 & 0 & -1 \end{bmatrix} \cdot \begin{bmatrix} v_{p,\text{off}}(t) \\ v_{n,\text{off}}(t) \\ v_{z,\text{off}}(t) \end{bmatrix} \tag{4.21}$$

and

$$\begin{bmatrix} v_{p,\text{off}}(t) \\ v_{n,\text{off}}(t) \\ v_{z,\text{off}}(t) \end{bmatrix} = \begin{bmatrix} -e^{-j\frac{2\pi}{3}} & 0 & 0 \\ 0 & -e^{+j\frac{2\pi}{3}} & 0 \\ 0 & 0 & -1 \end{bmatrix} \cdot \begin{bmatrix} v_{p,\text{on}}(t) \\ v_{n,\text{on}}(t) \\ v_{z,\text{on}}(t) \end{bmatrix} \tag{4.22}$$

where p, n, and z denote for postive, negative, and zero sequence components respectively. Remembering that there should not be any zero sequence currents flowing on the ac side of the converter therefore the zero sequence components can be removed from these transfers. Thus the FTM for the phase interchanging operation in symmetrical components can be defined as

$$\mathbf{\Lambda}_S = \begin{bmatrix} \mathcal{D}\{-e^{+jk\frac{2\pi}{3}}\} & 0 \\ 0 & \mathcal{D}\{-e^{-jk\frac{2\pi}{3}}\} \end{bmatrix} \tag{4.23}$$

where $k = 1$ for shifting the impulses to the subsequent phase and $k = -1$ for shifting the impulses to the previous phase. In this thesis, the small-signal ac side current is sampled from the commutating on phases.

The process of making two samples of the mismatch in the small-signal ac side current at the end of the base case commutation period, and converting them to four voltage impulses per phase each with a voltage-time area to step the small-signal ac side current to the correct condition at β_0 can be incorporated into the HSS equation in (4.2) and written in symmetrical components as

$$sI_{ac_{p,n}} = \left(\frac{-R}{L}\mathcal{I} + K_d \left(\mathbf{\Lambda}_S + \mathcal{I} \right) \Delta_{\beta_0} - \mathcal{N} \right) I_{ac_\phi} + \frac{1}{L}\mathcal{I}V_{com_{p,n}} \tag{4.24}$$

Figure 4.10 shows an example of resetting the small-signal ac side current at the end of the base case commutation period resulting from a one percent ac side voltage increase; the ac side waveforms are truncated to the 49^{th} harmonic. The rise of current is due to the faster commutation process, and the step back to zero is the result of the AMIT feedback loop given that there is no change in the dc side current.

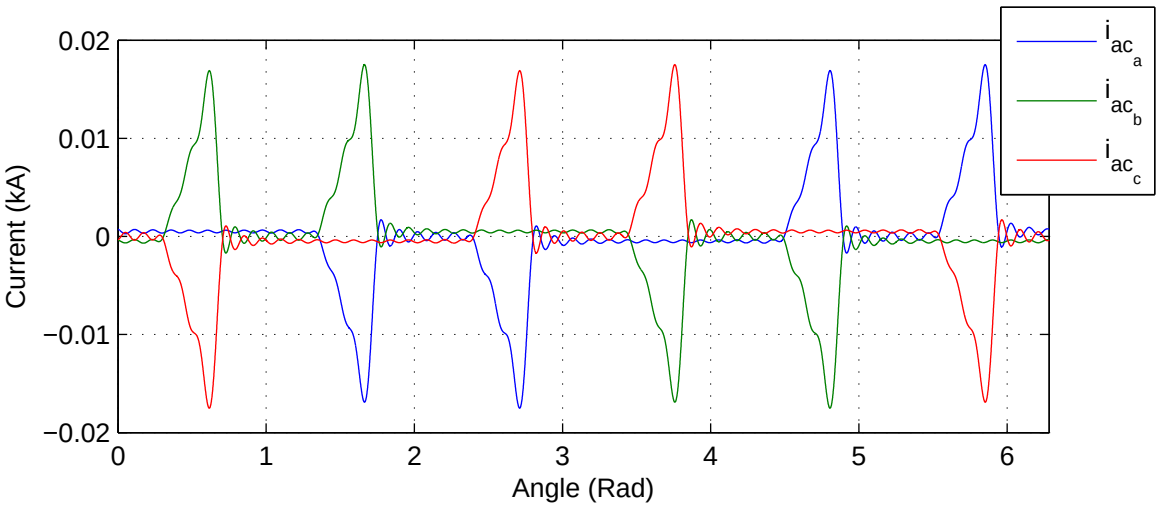

Figure 4.10: Small-signal ac side current waveforms resulting from a one percent ac voltage increase.

4.3.1.2 DC Side Current Variation

During the direct conduction period, the small-signal ac side current must equal the small-signal dc side current, but directly defining the ac side current state variable with the dc side current input is not allowed in a state-space environment. The current through an inductor posed as a state variable is governed by a unique state dynamic equation, and when two state variables are set to equal each other, in this case the current through the commutation reactance on the ac side and the current through the smoothing reactor on the dc side, they effectively share the same state dynamic equation, and one of these state variables becomes redundant. This makes the state matrix singular, and therefore it cannot be used to solve for the steady-state solution. The only way to make the ac side current and the dc side current equal is to create a voltage across the commutation circuit to force the ac side current to behave like the dc side current.

The time interval during which the small-signal dc side current injection has an influence over the ac side current spectra spans from the instant when the ac side phase begins to conduct till the instant that the ac side phase is disconnected from the dc side terminal. During this period, the small-signal dc side current interacts with the ac side commutation circuit through its associated impedance, more specifically the gradient of the small-signal dc side current, $\frac{d\Delta i_{dc}}{dt}$, induces a voltage across the commutation reactance, and the current itself, Δi_{dc}, creates a voltage across the resistive component of the commutation circuit.

During the direct conduction period, the voltage across the commutation circuit is the sum of the two voltages induced by the small-signal current injection on the dc side, and it can be described as

$$v_{com}(t) = L\frac{d\Delta i_{dc}(t)}{dt} + R\Delta i_{dc}(t) \tag{4.25}$$

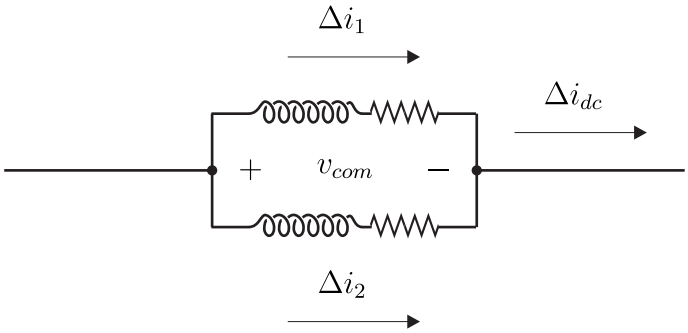

Figure 4.11: Commutation circuit configuration during the commutation period resulting from a small-signal dc side current injection and zero ac side voltage.

During the commutation period, the configuration of the commutation circuit is illustrated in Fig. 4.11, and summing up the voltages along the top half of the circuit yields,

$$v_{com}(t) = L\frac{d\Delta i_1(t)}{dt} + R\Delta i_1(t) \tag{4.26}$$

and similarly summing up the voltages along the bottom of the circuit yields,

$$v_{com}(t) = L\frac{d\Delta i_2(t)}{dt} + R\Delta i_2(t) \tag{4.27}$$

Remembering that,

$$\Delta i_{dc}(t) = \Delta i_1(t) + \Delta i_2(t) \tag{4.28}$$

and

$$\frac{d\Delta i_{dc}(t)}{dt} = \frac{d\Delta i_1(t)}{dt} + \frac{d\Delta i_2(t)}{dt} \tag{4.29}$$

while assuming the resistive and inductive components are of the same size in all three phases, the voltage drop across the commutation circuit in one of the commutating phase can be written in terms of the small-signal dc side current injection as

$$v_{com}(t) = \frac{1}{2}\left(L\frac{d\Delta i_{dc}(t)}{dt} + R\Delta i_{dc}(t)\right) \tag{4.30}$$

The voltage drop across the commutation circuit during the commutation period is half of the voltage drop during the direct conduction period. This can be encapsulated in a switching function that has rectangular sampling pulses at height $\pm\frac{1}{2}$ during the commutation period, but with height ± 1 during the direct conduction period. Hence the voltage across the commutation circuit induced by a small-signal dc side current injection can be described as

$$v_{com_\phi}(t) = \Psi_\phi^{v_{com}\leftarrow i_{dc}}(t)\left(L\frac{d\Delta i_{dc}(t)}{dt} + R\Delta i_{dc}(t)\right) \tag{4.31}$$

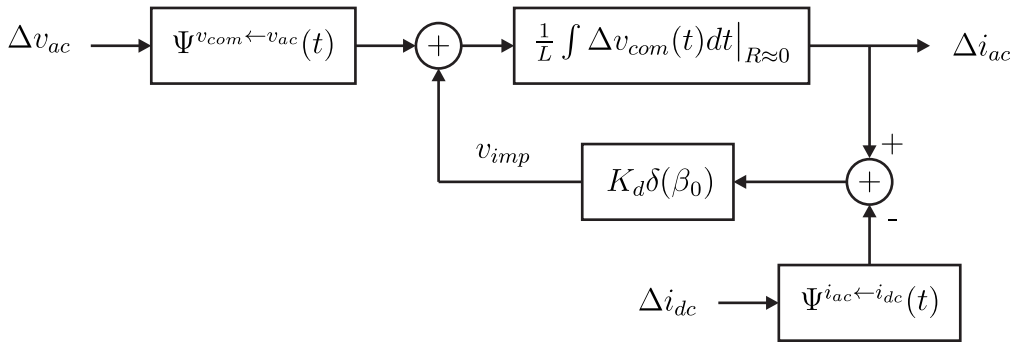

Figure 4.12: The AMIT feedback loop is updated to reset the ac side current waveforms to the sampled small-signal dc side current injection.

where the switching function can be written in the time domain with symmetrical components as

$$\Psi_{p,n\leftarrow d}^{v_{com}\leftarrow i_{dc}}(t) = \sum_m \frac{2}{m\pi}\left[\sin\left(\frac{m\pi}{3}\right)e^{-jm(\omega_0 t+\alpha_0)} + \sin\left(\frac{m\mu_0}{2}\right)\sin\left(\frac{m\pi}{3}\right)e^{-jm\left(\omega_0 t+\alpha_0+\frac{\mu_0}{2}\right)-j\frac{\pi}{2}}\right] \tag{4.32}$$

where $m = [..., -11, -5, 1, 7, 13, ...]$ for the transfer from the dc side current injection to the positive sequence components of the voltage across the commutation circuit on the ac side, and $m = [..., -13, -7, -1, 5, 11, ...]$ for the same transfer but to the negative sequence components of the voltage across the commutation circuit on the ac side.

The voltage derived from the sampled small-signal dc side current injection that is applied across the ac side commutation circuit only ensures that the shape of the ac side current is correct, but it does not guarantee the correct condition at the beginning of the direct conduction period. Given that the ac side current is sampled on the phases that are commutating to direct conduction, the AMIT process that resets the ac side current spectra to zero at the end of the base case commutation period must now be updated to reset the ac side current to the dc side current to ensure that the two currents are equal at the beginning of the direct conduction period. This requires the dc side current to be sampled and subtracted from the ac side current, and the difference is fed into the AMIT feedback loop. The updated block diagram is illustrated in Fig. 4.12.

The small-signal dc side current injection is sampled at the end of the base case commutation period for the phase that is beginning its direct conduction, and at each consecutive instant (separated by π) its sampled polarity is reversed. In order to obtain a consecutively reversed sample and reduce the ringing effect associated with frequency truncation, the dc side current is sampled with a sinusoidal waveform at fundamental frequency with an amplitude of 1, and crossing its peak at β_0. The sinusoidal sampling waveform is simply written in symmetrical

components as

$$\Psi_{p,n\leftarrow d}^{i_{ac}\leftarrow i_{dc}}(t) = e^{-jm(\omega_0 t+\beta_0)} \tag{4.33}$$

where $m = 1$ for a transfer from the small-signal dc side current injection to a positive sequence sample, and $m = -1$ to a negative sequence sample.

Overall, the approach to ensure the ac side current is the same as the dc side current during the direct conduction period does not directly define the ac side current state variable to equal the dc side current state variable, therefore it does not invoke the complication of creating a dependent state variable. Instead, one state variable is set to track the other, i.e. the ac side current is tracking the dc side current by providing a correct condition through the AMIT feedback loop at the beginning of the direct conduction period, and a subsequent voltage applied across the commutation circuit to manage the shape of the ac side current.

Figure 4.13 gives an example of resetting the ac side current to the dc side current at the beginning of the direct conduction period, and the ac side waveforms are truncated to the 49^{th} harmonic while the switching function for a dc side to ac side transfer is truncated to the 97^{th}*harmonic*. The small-signal ac side current results solely from a 0.1 kA/s ramp increase on the dc side current. It can be observed in Fig. 4.13c that the ac side current ramps up at the same rate as the dc side current injection during the direct conduction period as expected.

At the beginning of the commutation period, the ac side current state variable starts from where it was at the end of the direct conduction period, i.e. the condition of the state variable is preserved, and the ac side current continues to ramp but at a reduced rate. This is due to the fact that the dc side current injection is shared evenly across the two commutating phases, and consequently the ramping of the ac side current is at 0.05 kA/s during the commutation period. However, due to the ringing associated with frequency truncation this is difficult to observe from Fig. 4.13c. At the end of the commutation period the impulses in the feedback loop samples the difference between the dc side current and the current in the next commutating on phase to generate the voltage impulses shown in Fig. 4.13b. The voltage impulses are used to reset the current in the commutating off phase to zero, and step the current in the commutating on phase to be the same as the dc side current.

4.3.2 Small-Signal DC Side Voltage Spectrum

The overall small-signal variation in the dc side voltage is the sum of each contribution from the small-signal ac side voltage injection, the small-signal dc side current injection, and the effects associated with SIV resulting from the small-signal injections.

A small-signal variation in the ac side voltage generates a small-signal dc side voltage in the same way as the base case ac side voltage generates the base case dc side voltage spectrum.

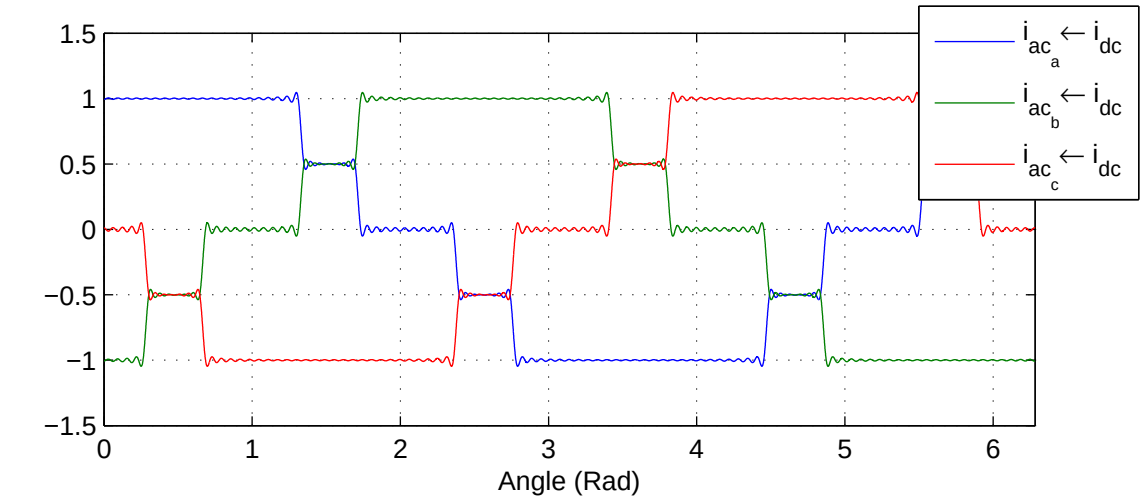

(a)

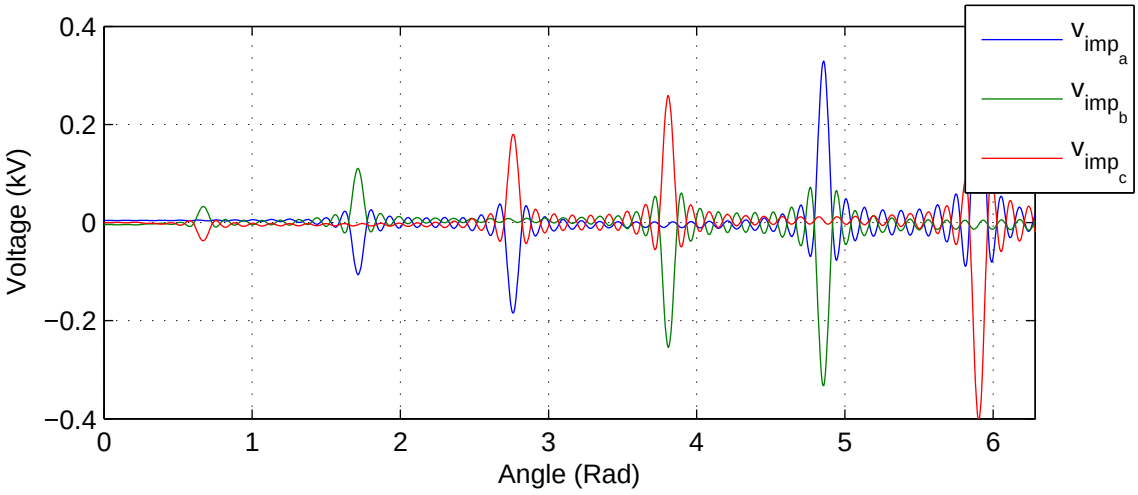

(b)

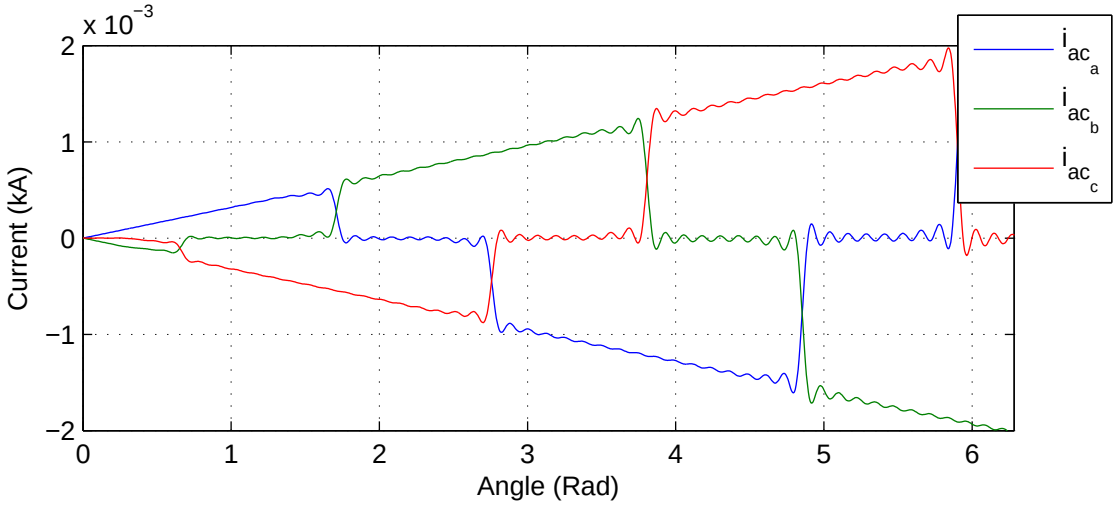

(c)

Figure 4.13: Generating the small-signal ac side current waveforms resulting from a dc side current injection: (a) The switching functions to transfer the dc side current injection to ac side quantities. (b) The voltage impulses generated from the AMIT feedback loop. (c) The small-signal ac side current waveforms resulting from a ramp increase in the dc side current.

The difference is that the SIV associated with the small-signal ac side voltage injection must be incorporated appropriately. In the case of a small variation in the dc side current, small-signal voltages are induced across the ac side commutation circuit which contribute to a voltage change on the dc side. Similarly, the SIV associated with a small-signal dc side current injection must also be included in the transfer to the dc side voltage.

4.3.2.1 AC Side Voltage Variation

The transfer from the small-signal variation in ac side voltage to the small-signal dc side voltage is identical to the base case. Therefore, the equations in (4.8) and (4.9) are reused to describe the switching function during the direct conduction period and the commutation period respectively. The small-signal dc side voltage resulting from a small-signal variation in ac side voltage is written as

$$\Delta v_{dc} = \sum_{\phi} \left(\Psi_{\phi,direct}^{v_{dc} \leftarrow v_{ac}}(t) + \Psi_{\phi,commutation}^{v_{dc} \leftarrow v_{ac}}(t) \right) \Delta v_{ac}(t) \tag{4.34}$$

where ϕ denotes phase a, b, and c respectively.

The SIV associated with a small-signal ac side voltage injection only affects the end of the commutation period in this uncontrolled converter model. If the small-signal injection increases the voltage across the commutation circuit, the current through the commutation reactance changes at a faster rate, thus the end of commutation period is brought forward in time, and results in a shorter commutation period. The opposite happens if the small-signal injection decreases the voltage across the commutation circuit, i.e. the end of the commutation period is postponed in time.

The advance or delay of the end of the commutation period results in a significant gain or loss of voltage-time area in the small-signal dc side voltage spectrum. Figure 4.14 illustrates the exaggerated effect of an SIV occurring at the end of the base case commutation period on the dc side voltage. The solid line represents the base case dc side voltage while the thick dashed line represents the dc side voltage resulting from a perturbed ac side voltage. The shaded area represents the gain or loss in voltage-time area due to the SIV.

The shaded area is again referred as the *indirect area* in [Hume 2002], but this time, this indirect area has a horizontal dimension that is proportional to the injection and a fixed vertical dimension, therefore it does contribute to the linearised transfer. Subtracting the base case dc side voltage from the perturbed dc side voltage, it is clear that advancing the end of commutation period results in a positive voltage-time area, likewise delaying the end of the commutation period results in a negative voltage-time area, and as the change in the switching instant tend towards a small value, the voltage-time area resembles an impulse. This suggests that once again the AMIT spectrum can be applied to mimic the effect of SIV on the dc side voltage waveform.

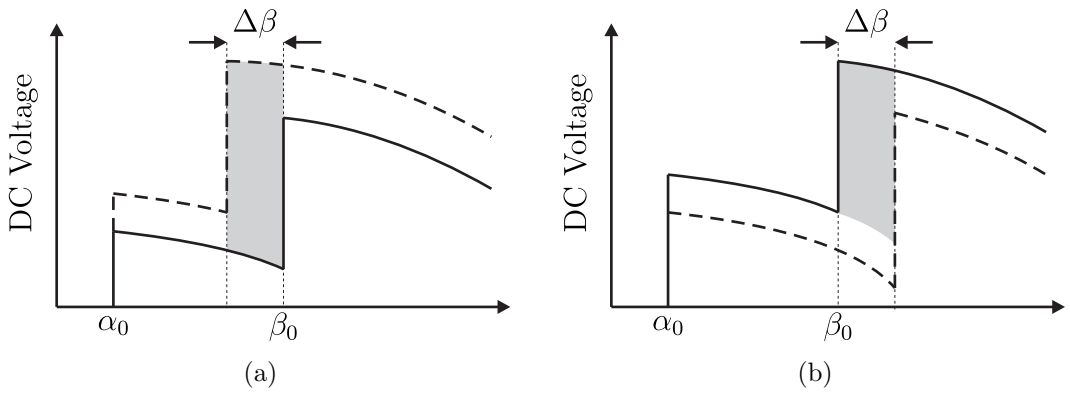

Figure 4.14: Graphical illustration of the consequences associated with an autonomous SIV on the dc side voltage waveform: (a) The end of the commutation period is brought forward in time. (b) The end of the commutation period is delayed in time.

In a later section, this voltage impulse is applied across a dc side smoothing reactor, resulting in a correct change in the dc side current through the equation set associated with the dc side circuit.

The voltage-time area has a height close to half of the ac side line-to-line voltage at the end of the base case commutation period between the two commutating phases, and a width of the change in the end of the commutation period, this voltage-time area, $A_{indirect}$, can be approximated by

$$A_{indirect} = \frac{\Delta\beta}{\omega_0} \cdot \frac{v_1|_{\beta_0} - v_2|_{\beta_0}}{2} \tag{4.35}$$

where v_1 and v_2 are the base case line-to-ground voltages of the two commutating phases, and the base case end of commutation instant β_0 is measured in radians. Assuming that each impulse in the AMIT spectrum integrates to an area equal to unity, they must be modulated by the indirect area and summed to the dc side voltage spectrum to model the change in voltage-time area due to SIV.

The change in the end of the commutation period, $\Delta\beta$, can be approximated by the use of the AMIT feedback loop given that the gradient of the ac side current at the end of the base case commutation period is known *a priori*. Consider a small-signal ac side voltage distortion that forces a faster commutation process; the resulting ac side current flowing in the phase that is commutating to a non-conduction period in this linearised model overshoots zero before a voltage impulse resets it back to zero at the end of the commutation period. Figure 4.15 demonstrates an exaggerated illustration of this scenario. If the size of the offset in the ac side current is known at the end of the base case commutation period, along with its base case gradient, the change in the commutation period can be approximated as

$$\Delta\beta \approx \omega_0 \, \Delta i_{ac}(t)|_{\beta_0} \cdot \left.\frac{dt}{di_{ac}(t)}\right|_{\beta_0} \tag{4.36}$$

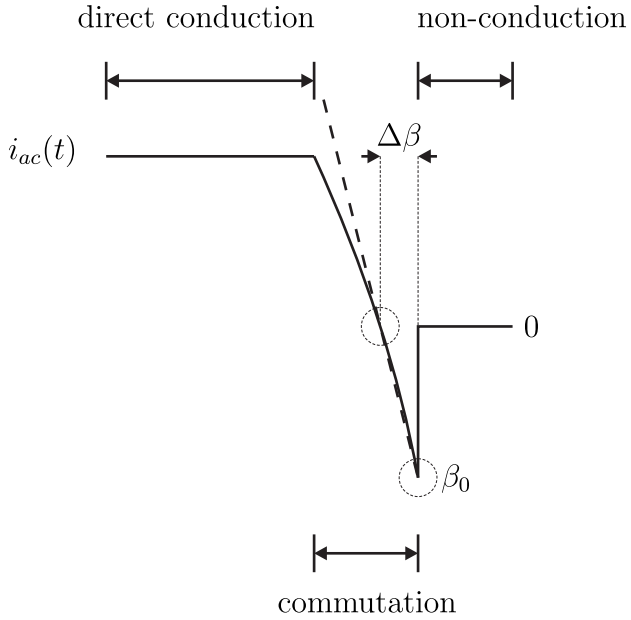

Figure 4.15: Using the base case rate of change of the ac side current to approximate the size of SIV at the end of the commutation period.

Therefore, the same AMIT feedback loop as described in Sec. 4.3.1.2 can be used to sample the small-signal ac side current at the end of the base case commutation period.

The gradient at the end of the base case commutation period can be calculated from the base case line-to-ground voltages of the commutating phases as

$$\left.\frac{di_{ac}(t)}{dt}\right|_{\beta_0} = \frac{v_1|_{\beta_0} - v_2|_{\beta_0}}{2L} \tag{4.37}$$

Substituting (4.36) and (4.37) into (4.35) yields the voltage-time area that needs to be summed to the dc side voltage spectrum. This is written as

$$\begin{aligned} A_{indirect} &= \frac{\cancel{2}L}{v_1|_{\beta_0} - v_2|_{\beta_0}} \cdot \frac{v_1|_{\beta_0} - v_2|_{\beta_0}}{\cancel{2}} \Delta i_{ac}(t)|_{\beta_0} \\ &= L\ \Delta i_{ac}(t)|_{\beta_0} \end{aligned} \tag{4.38}$$

This is exactly the same as the voltage impulse applied across the commutation circuit at the end of the base case commutation period to reset the ac side current spectrum. Thus, the voltage impulse train applied across the commutation circuit can be transferred to the dc side through a switching function, and the transferred voltage impulses are summed to the dc side voltage to incorporate the effect of SIV on the dc side.

The switching function used to transfer the voltage impulses across the commutation circuit to the dc side is again a sinusoidal function at fundamental frequency with an amplitude of 1, and crossing its peak at the end of the base case commutation period. This sinusoidal sampling

spectrum is written in symmetrical components as

$$\Psi_{d\leftarrow p,n}^{v_{imp_{dc}}\leftarrow v_{imp_{ac}}}(t) = e^{-jm(\omega_0 t+\beta_0)} \tag{4.39}$$

where $m = -1$ for the transfer from the positive sequence components of the ac side voltage impulses, and $m = 1$ for the transfer from the negative sequence components of the ac side voltage impulses. While these voltage impulses are not a perfect representation of the effect of SIV, they are integrated by the dc side smoothing inductor and result in a correct dc side current trajectory.

As an example, a one percent increase on the ac side voltage is modelled. This results in a shorter commutation period compared to the base case, and therefore positive voltage impulses appear on the small-signal dc side voltage spectrum. Figure 4.16 shows a plot of the dc side voltage spectrum resulting from the small-signal ac side voltage injection without the effect of SIV, a plot of the dc side voltage impulses resulting from the SIV associated with the small-signal distortion, and finally, a plot of the contributions combined to form the overall small-signal dc side voltage spectrum. These dc side waveforms are truncated to the 48^{th} harmonic. This concludes the analysis of the effect of SIV resulting from a small-signal ac side voltage injection on the dc side voltage spectrum.

4.3.2.2 DC Side Current Variation

This section describes the transfer from the small-signal dc side current injection to the dc side voltage spectrum. The dc side current injection is assumed to be flowing in the same direction as the base case dc side current, that is the currents on the ac side are flowing into the converter while the current on the dc side is flowing out of the converter. When a small-signal current variation is introduced on the dc side, the dc side voltage is affected by the voltage drop across the commutation circuit.

During the direct conduction period, two ac side phases are connected in series through the dc side as illustrated in Fig. 4.2a, and during the commutation period, the two commutating ac side phases are joined together at the dc side terminal, in series with the third direct conducting circuit as illustrated in Fig. 4.2b. The small-signal voltage change on the dc side due to these two circuit configurations can be written as

$$\Delta v_{dc}(t) = -2L\frac{d\Delta i_{dc}(t)}{dt} - 2R\Delta i_{dc}(t) \tag{4.40}$$

and

$$\Delta v_{dc}(t) = -\frac{3}{2}L\frac{d\Delta i_{dc}(t)}{dt} - \frac{3}{2}R\Delta i_{dc}(t) \tag{4.41}$$

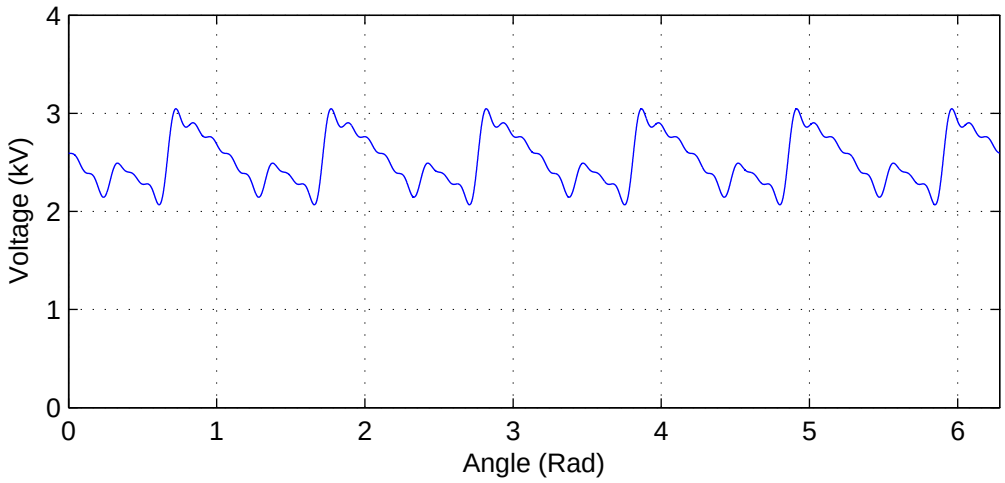

(a)

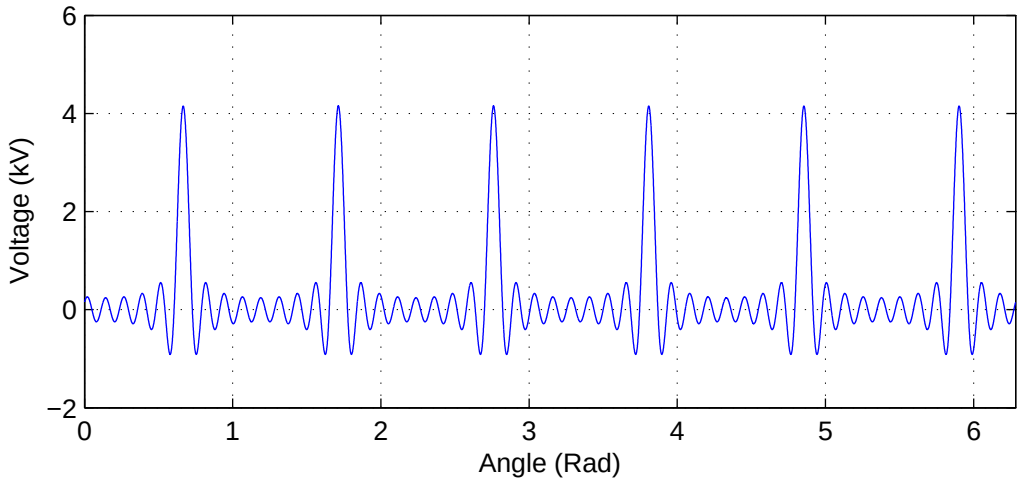

(b)

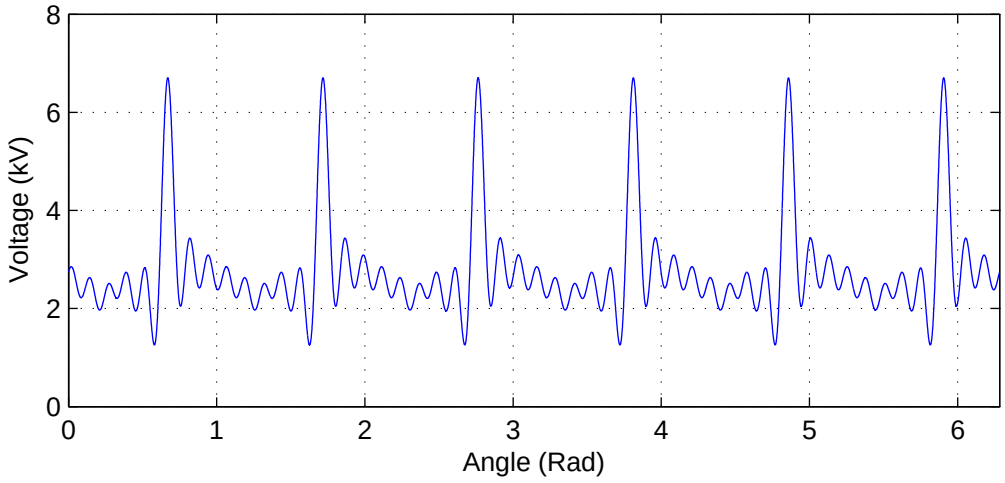

(c)

Figure 4.16: The small-signal dc side voltage waveform is a sum of the transfer from the small-signal ac side voltage injection, and the effect associated with SIV: (a) The dc side voltage waveform solely resulting from the small-signal ac side voltage injection. (b) The voltage impulses on the dc side associated with SIV. (c) The overall dc side voltage waveform resulting from a one percent increase in ac side voltage.

where (4.40) is valid during the direct conduction period while (4.41) is valid during the commutation period.

Thus the small-signal transfer from dc side current distortion to the dc side voltage can be written as

$$\Delta v_{dc}(t) = -\Psi^{v_{dc}\leftarrow i_{dc}}\left(L\frac{d\Delta i_{dc}(t)}{dt} + R\Delta i_{dc}(t)\right) \tag{4.42}$$

where $\Psi^{v_{dc}\leftarrow i_{dc}}$ is a switching function that describes the two circuit configurations discussed previously.

The switching function requires a rectangular sampling pulse with a height of 2 during the direct conduction period and a rectangular sampling pulse with height of $\frac{3}{2}$ during the commutation period. This can be written using symmetrical components, and in a piecewise manner as

$$\Psi^{v_{dc}\leftarrow i_{dc}}_{direct}(t) = 1 - \frac{3\mu_0}{\pi} - \sum_m \frac{12}{m\pi}\sin\left(\frac{m\mu_0}{2}\right)e^{-jm\left(\omega_0 t+\frac{\pi}{6}+\alpha_0\right)} \tag{4.43}$$

and

$$\Psi^{v_{dc}\leftarrow i_{dc}}_{commutation}(t) = \frac{9\mu_0}{2\pi} + \sum_m \frac{9}{m\pi}\sin\left(\frac{m\mu_0}{2}\right)e^{-jm\left(\omega_0 t+\frac{\pi}{6}+\alpha_0\right)} \tag{4.44}$$

where $m = [..., -12, -6, 0, 6, 12, ...]$ for both equations. Figure 4.17 shows a plot of the switching function to transfer the small-signal dc side current injection to the dc side voltage, and this switching function is truncated to the 96^{th} harmonic.

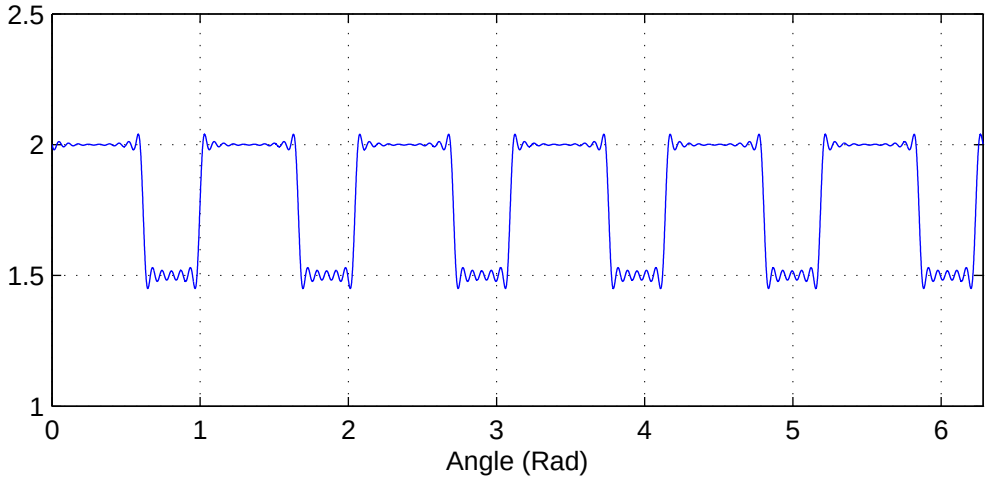

Figure 4.17: Switching function to transfer the small-signal dc side current injection to the dc side voltage.

Any small-signal dc side current injection introduces a SIV at the end of the commutation period, and its associated effect is the same as the SIV resulting from a small-signal ac side voltage injection. Therefore, the same analysis also applies in this case, and as it is already discussed in detail in the transfer from the small-signal ac side voltage injection to the dc side

voltage spectrum, it is not repeated here.

4.3.3 DC Side Circuit

Any analysis associated with the dc side current till this point have assumed an open circuit across the dc side terminals, thus the dc side current that is leaving the converter flowing into the dc side and its derivative have been treated as system inputs in the model. In order to complete the converter system as shown in Fig. 4.1, the dc side terminals must be connected to a dc side circuit which consists of a resistor and inductor (RL) in series.

The dc side series RL circuit can be modelled by the same state dynamic equation in (4.2) for the ac side commutation circuit, but the measurement equation has to be updated to include the dc side current derivative as an output of the dc side subsystem. The state dynamic equation for the dc side RL circuit is written in the HSS as

$$sI_{dc} = \left(-\frac{R_{dc}}{L_{dc}}\mathcal{I} - \mathcal{N}\right) I_{dc} + \frac{1}{L_{dc}}\mathcal{I}V_{dc} \tag{4.45}$$

while its associated measurement equation is written as

$$\begin{bmatrix} I_{dc} \\ \dot{I}_{dc} \end{bmatrix} = \begin{bmatrix} \mathcal{I} \\ -\frac{R_{dc}}{L_{dc}}\mathcal{I} \end{bmatrix} I_{dc} + \begin{bmatrix} 0 \\ \frac{1}{L_{dc}}\mathcal{I} \end{bmatrix} V_{dc} \tag{4.46}$$

where $\mathcal{I}$ is the identity matrix, and $\mathcal{N}$ is the Toeplitz matrix consisting of the dc side harmonics $[..., -6, 0, 6, ...]$ up to the maximum harmonic truncation, which in this case is the 48^{th} harmonic on the dc side.

This completes the development of a small-signal HSS model for the 6-pulse HVdc converter without active control; this open-loop model is described by the block diagram shown in Appendix B. The HSS model is expected to capture the correct response of the uncontrolled converter system upon a small-signal input, and the following section presents some examples of the results generated by the model.

4.4 OPEN-LOOP MODEL VALIDATION

In order to validate the modelling procedure described in the preceding sections, an HSS model truncated up to the 49^{th} harmonic on the ac side and 48^{th} harmonic on the dc side is programmed in MATLAB while an equivalent time domain model is built using PSCAD/EMTDC with a solution time step of 20 microseconds. The small-signal response of the time domain model is the difference between two separate responses generated using two set of inputs, the first set of inputs are the base case quantities, and the second set of inputs are the base case quantities plus

distortion. On the other hand, the HSS model directly outputs the small-signal response from the distortion. The small-signal results are compared in terms of time domain plots as well as magnitude and angle plots of the harmonics in steady-state.

4.4.1 Positive Sequence AC Side Voltage Variation

In this test, a one percent increase in the base case ac side voltage is chosen as the small-signal input. Figures 4.18 and 4.19 show the resulting time domain plots of the ac side and the dc side signals produced from both the HSS model and an equivalent PSCAD/EMTDC simulation. The HSS model generates results for each individual harmonics modelled and the corresponding time domain plot is the sum of all these harmonics whereas the PSCAD/EMTDC simulation naturally produces time domain results. The results from the HSS model are plotted in thin black lines while the results from the PSCAD/EMTDC simulation are plotted in thick grey lines. These plots are zoomed in to the first three fundamental cycles to highlight the good agreement between the two models during the transient period.

It is clear in Fig. 4.18 that the voltage impulses described in Sec. 4.3.1 resets the ac side currents to the correct condition at the end of each commutation period, and this suggests a correct model of SIV. There may seem to be some discrepancies in the magnitude of the voltage impulses between the dc side voltage waveforms shown in Fig. 4.19a upon glance, but as discussed in Sec. 4.3.2 it is the voltage-time area of the voltage impulses that is important in producing a correct dc side current waveform. The good agreement between the dc side currents produced by the two models shown in Fig. 4.19b implies that the HSS model produces a correct voltage-time area in the dc side voltage waveform.

Figures 4.20 and 4.21 are time domain plots of the ac side and the dc side signals zoomed in to highlight a single fundamental period in steady-state. The steady-state harmonics of the response from the HSS model is directly produced through the use of the *harmonic transfer function* as described in Sec. 3.9, and again the time domain plots are generated as a sum of the steady-state harmonics. The magnitude and phase angle of each individual steady-state harmonic of the responses are also compared in Fig. 4.22, 4.23, 4.24, and 4.25. It can be seen that the magnitude and phase angle of each steady-state harmonics produced by the HSS model is consistent with the results from PSCAD/EMTDC which are generated through a Fast Fourier Transform (FFT) of its steady-state time domain waveforms.

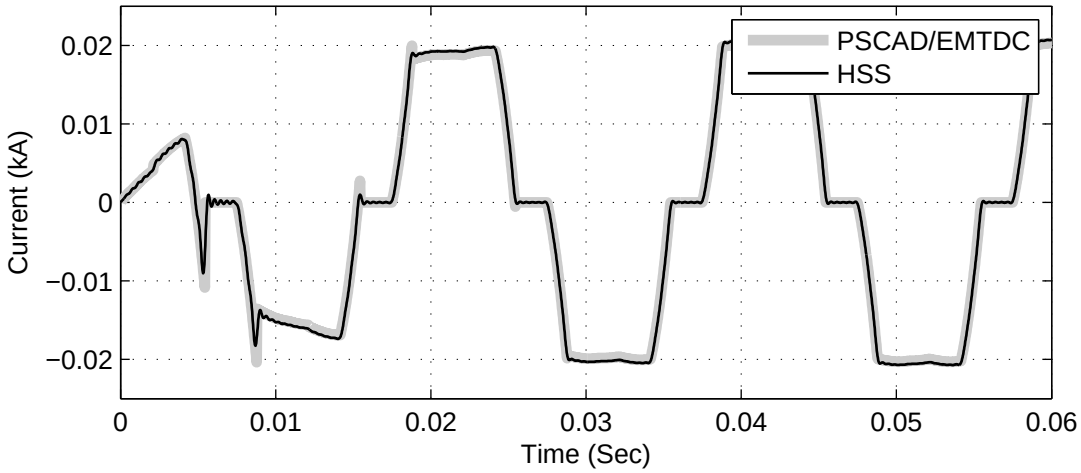

(a)

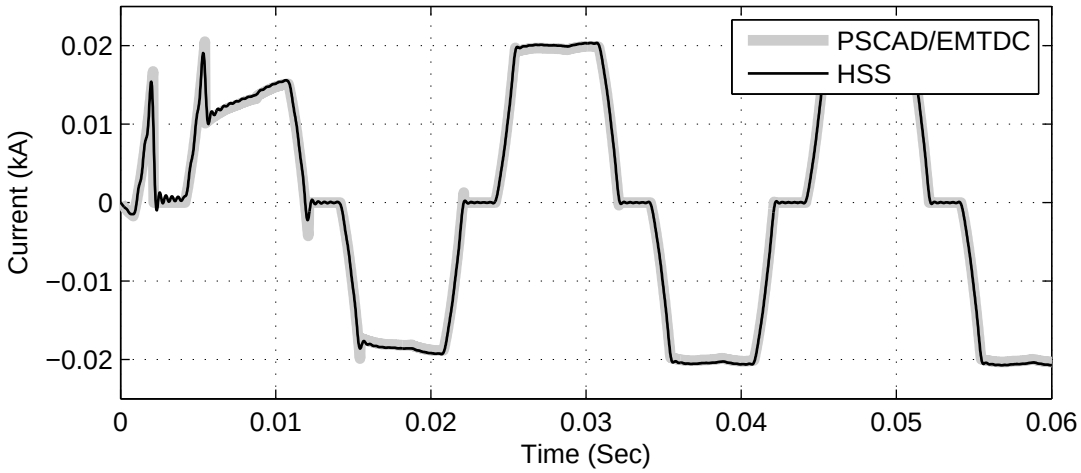

(b)

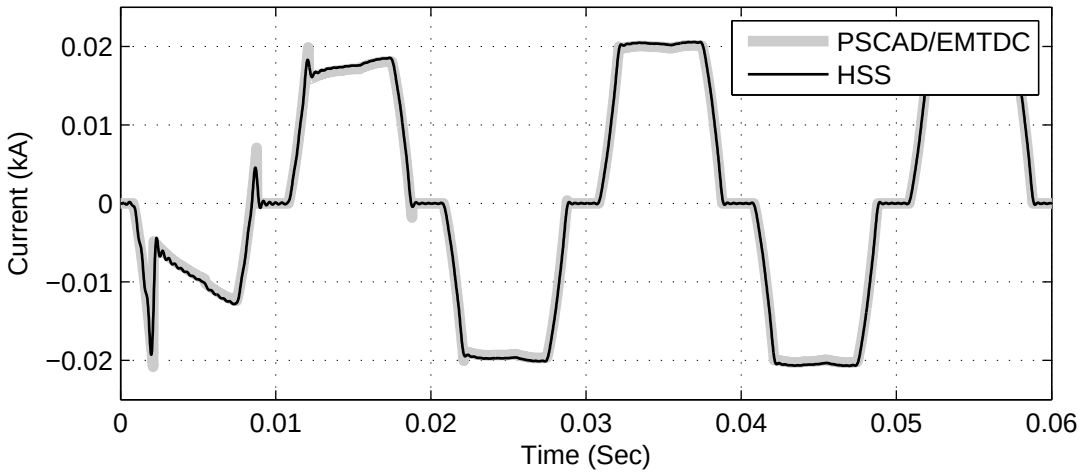

(c)

Figure 4.18: The transient response of the small-signal ac side currents resulting from a one percent increase in the base case ac side voltage: (a) The resulting phase a current waveform. (b) The resulting phase b current waveform. (c) The resulting phase c current waveform.

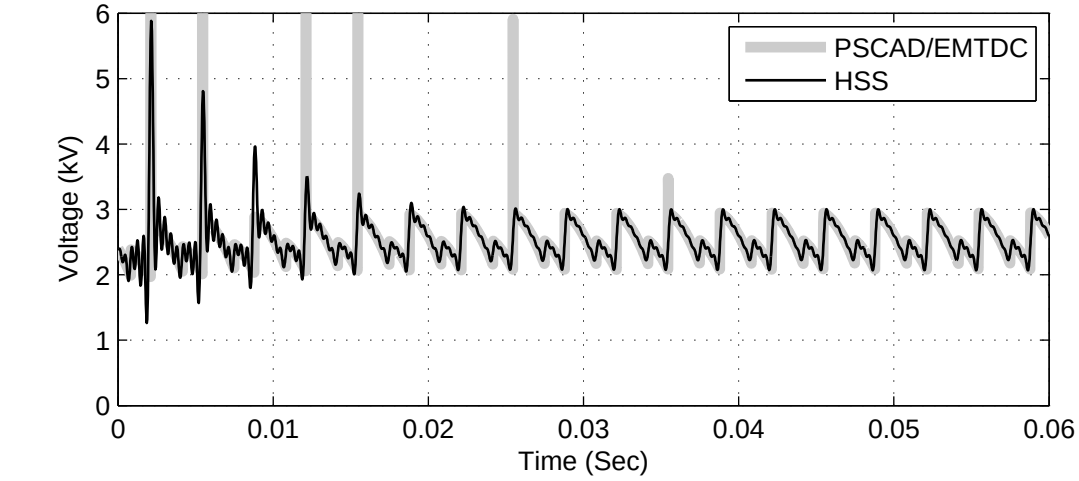

(a)

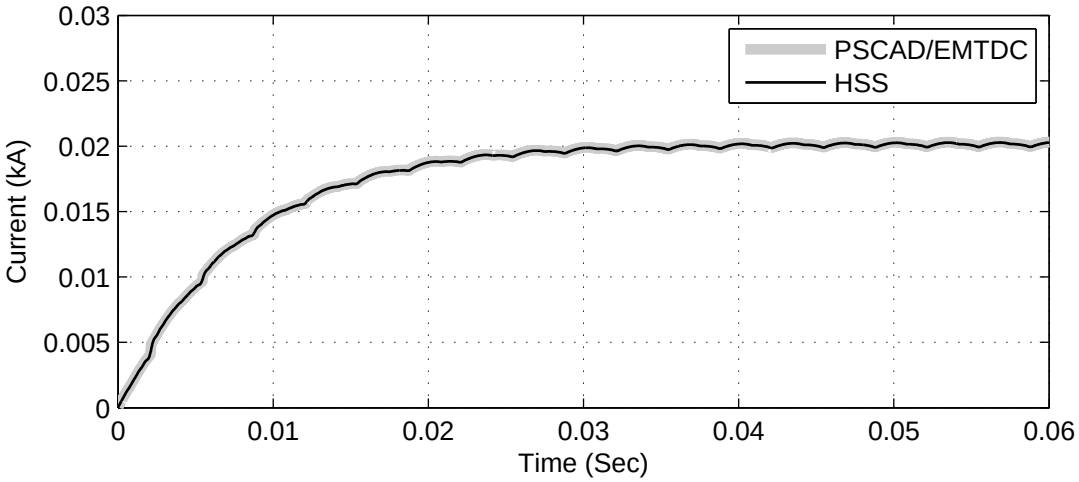

(b)

Figure 4.19: The transient response of the small-signal dc side voltage and current resulting from a one percent increase in the base case ac side voltage: (a) The resulting dc side voltage waveform. (b) The resulting dc side current waveform.

4.4.2 Negative Sequence AC Side Voltage Variation

To further validate the HSS model, a one percent negative sequence voltage at the fundamental frequency is injected on the ac side. In the HSS model, this is achieved by modulating the two fundamental frequency components of the small-signal input. The +1 harmonic is modulated by $e^{-j2\omega_0 t}$ as it is treated as a positive sequence in the system transfers, and similarly, the -1 harmonic is modulated by $e^{+j2\omega_0 t}$. The resulting waveforms of the ac side and the dc side signals are plotted in Fig. 4.26 and 4.27. The plots are zoomed in on the first three fundamental cycles to highlight the transient response of the signals. These time domain plots again confirm the accuracy of the HSS model. In particular, it is clear that the voltage impulses applied across the commutation circuit resets the ac side current correctly which results in practically zero current

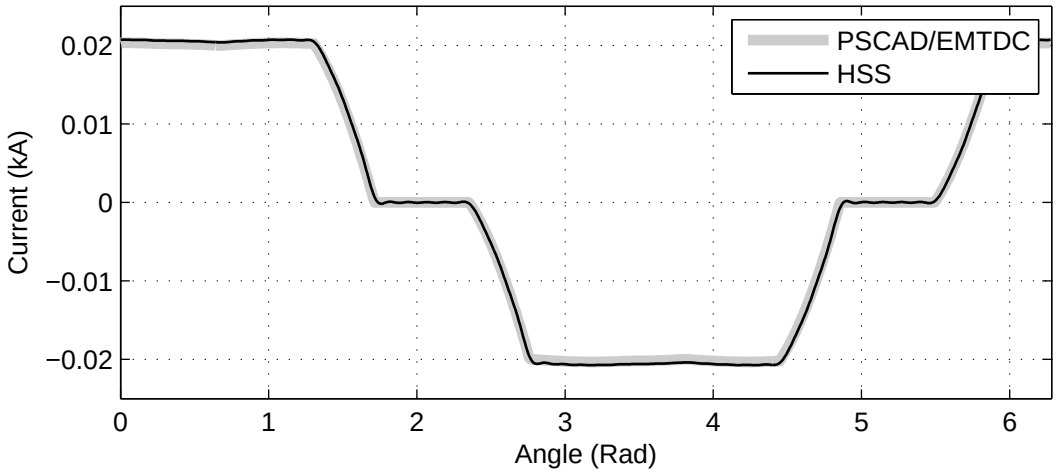

(a)

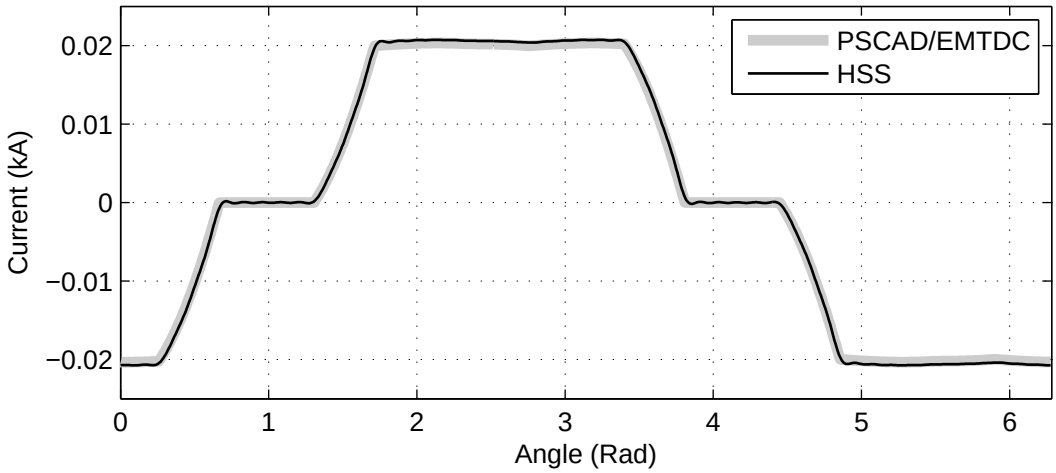

(b)

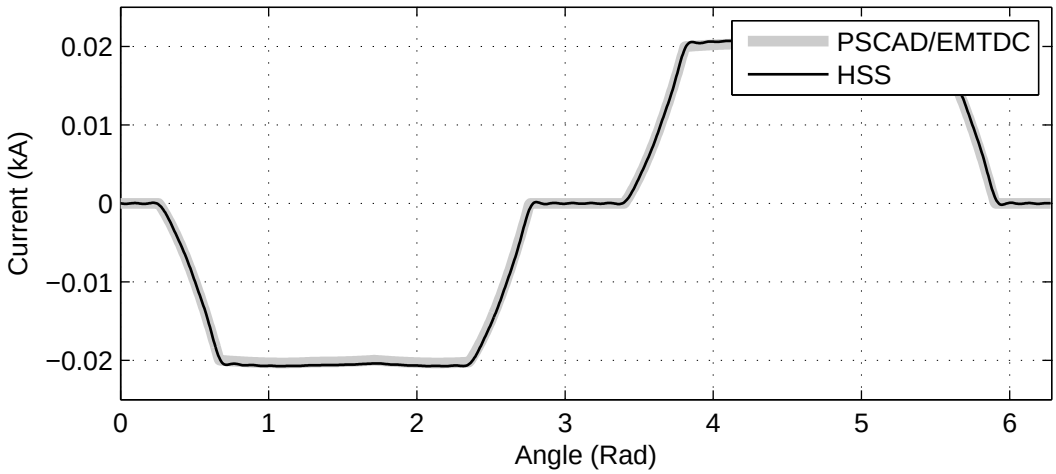

(c)

Figure 4.20: The steady-state small-signal ac side current waveforms resulting from a one percent increase in the base case ac side voltage: (a) The resulting phase a current waveform. (b) The resulting phase b current waveform. (c) The resulting phase c current waveform.

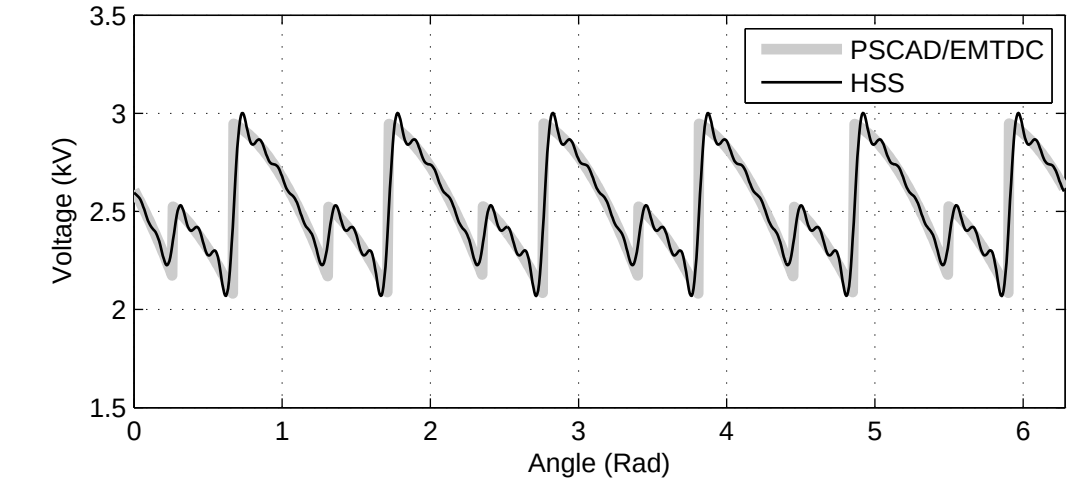

(a)

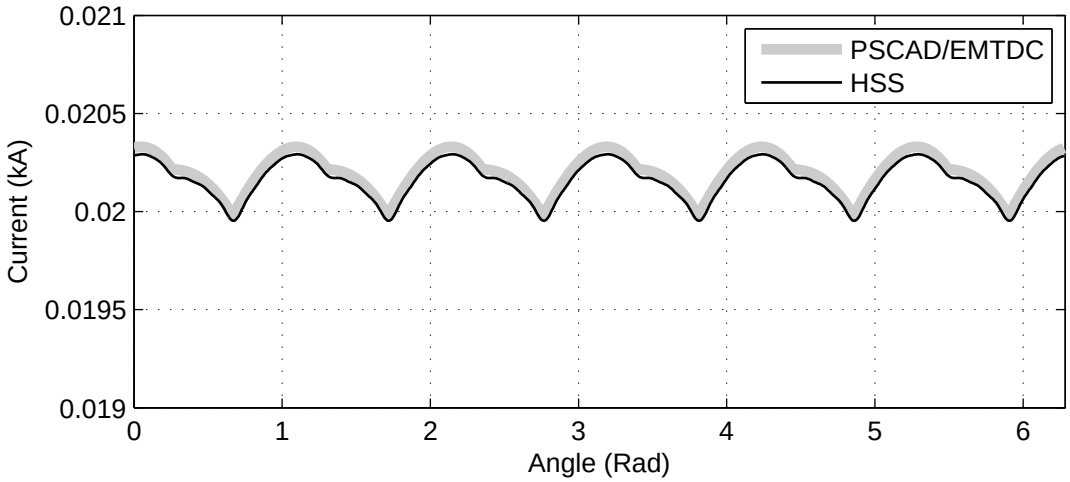

(b)

Figure 4.21: The steady-state small-signal dc side voltage and current waveforms resulting from a one percent increase in the base case ac side voltage: (a) The resulting dc side voltage waveform. (b) The resulting dc side current waveform.

during the non-conduction period as shown in Fig. 4.26. Furthermore, the same set of voltage impulses are transferred and summed to the dc side voltage which produces a correct trajectory of the dc side current during the transient period as shown in Fig. 4.27. These are evidences to the correct modelling of the effects associated with SIV.

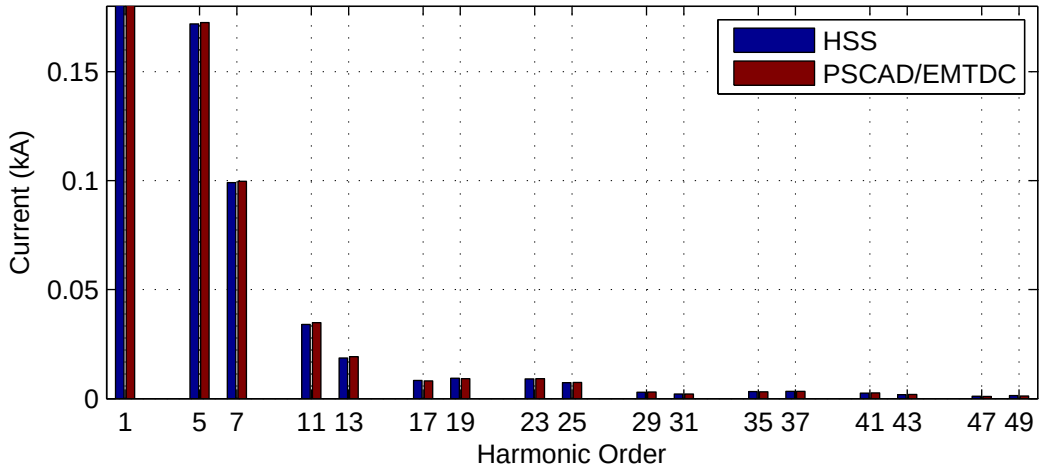

(a)

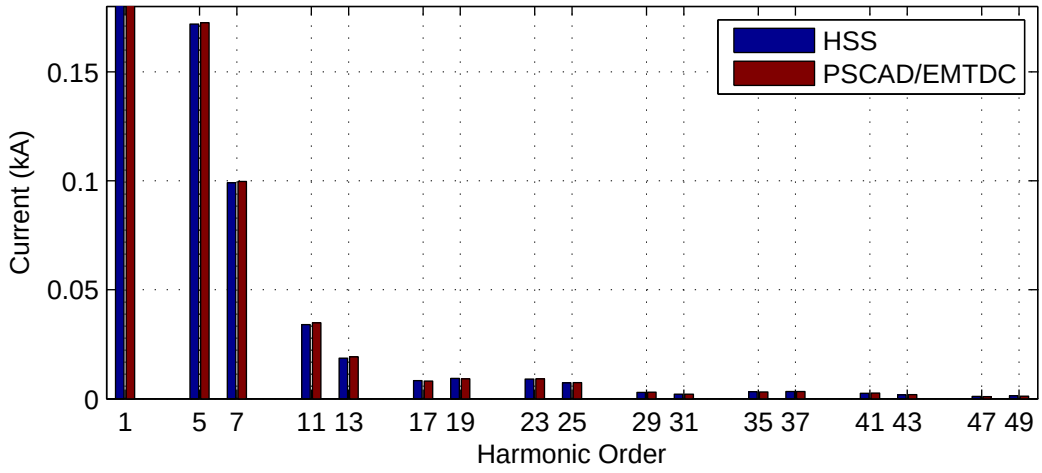

(b)

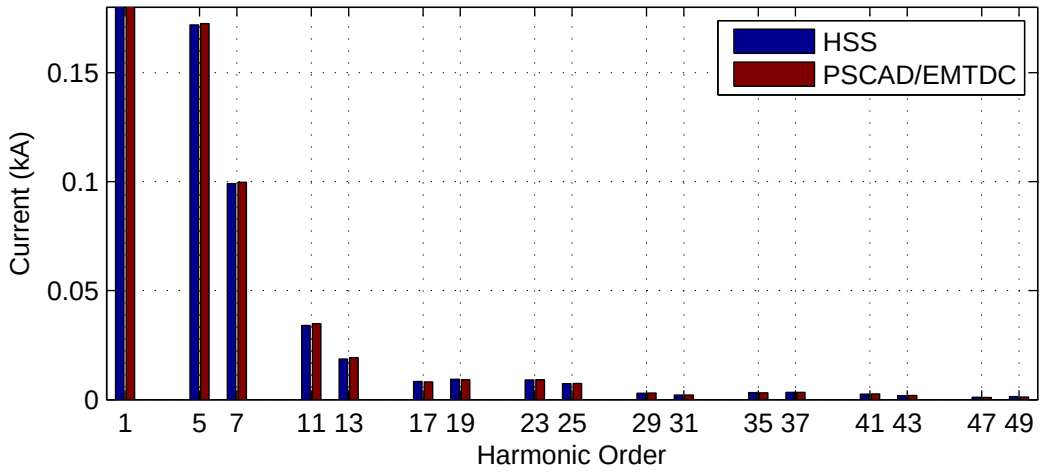

(c)

Figure 4.22: The magnitude of the small-signal ac side current harmonics resulting from a one percent increase in the base case ac side voltage (normalised to the fundamental component): (a) The resulting magnitude of the phase a current harmonics. (b) The resulting magnitude of the phase b current harmonics. (c) The resulting magnitude of the phase c current harmonics.

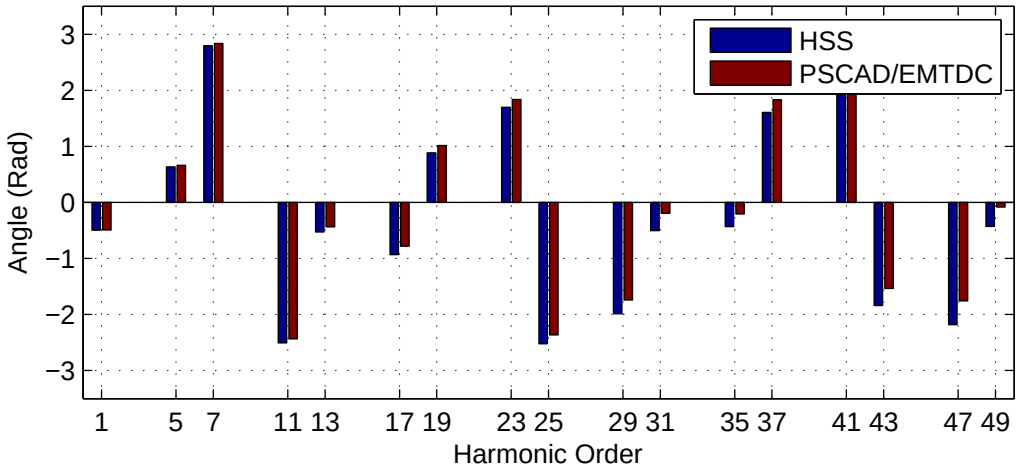

(a)

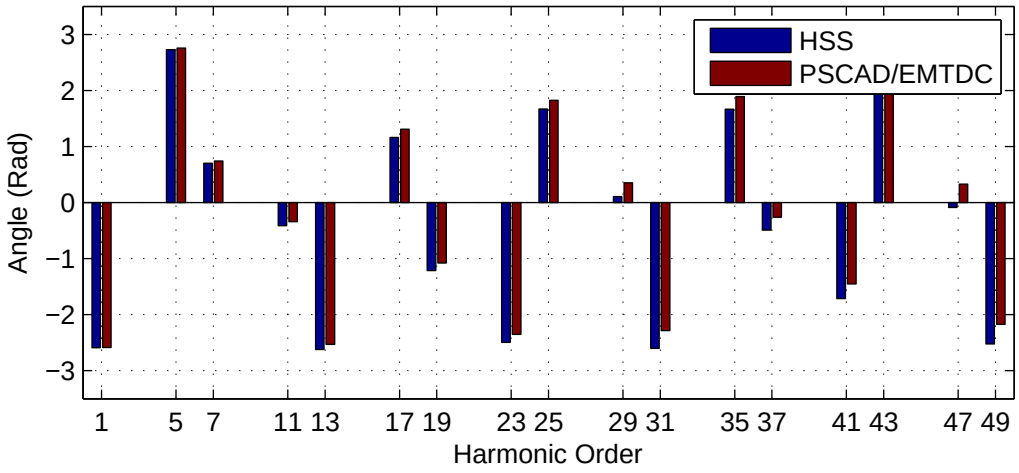

(b)

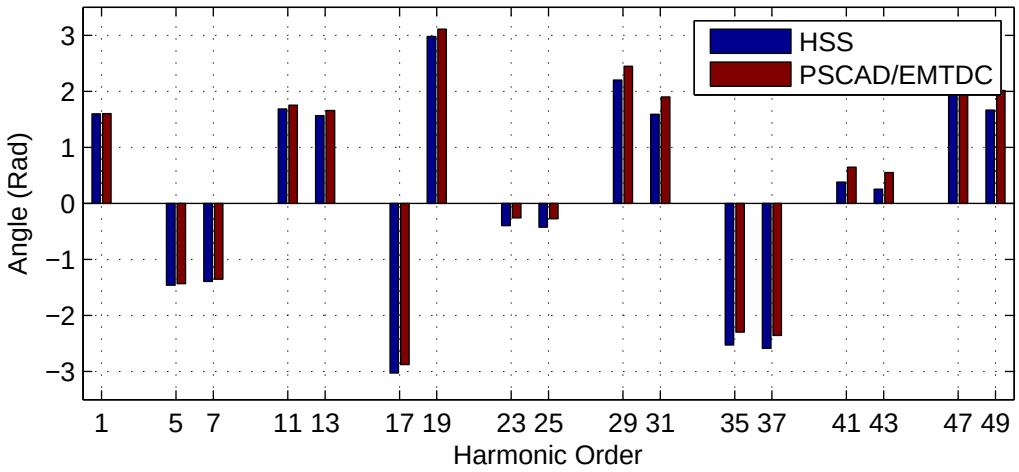

(c)

Figure 4.23: The angle of the small-signal ac side current harmonics resulting from a one percent increase in the base case ac side voltage: (a) The resulting angle of the phase a current harmonics. (b) The resulting angle of the phase b current harmonics. (c) The resulting angle of the phase c current harmonics.

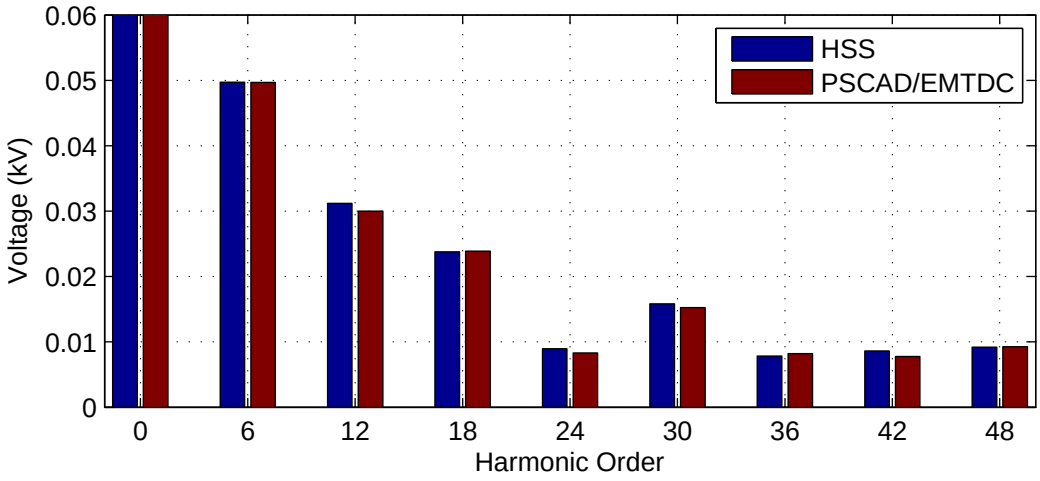

(a)

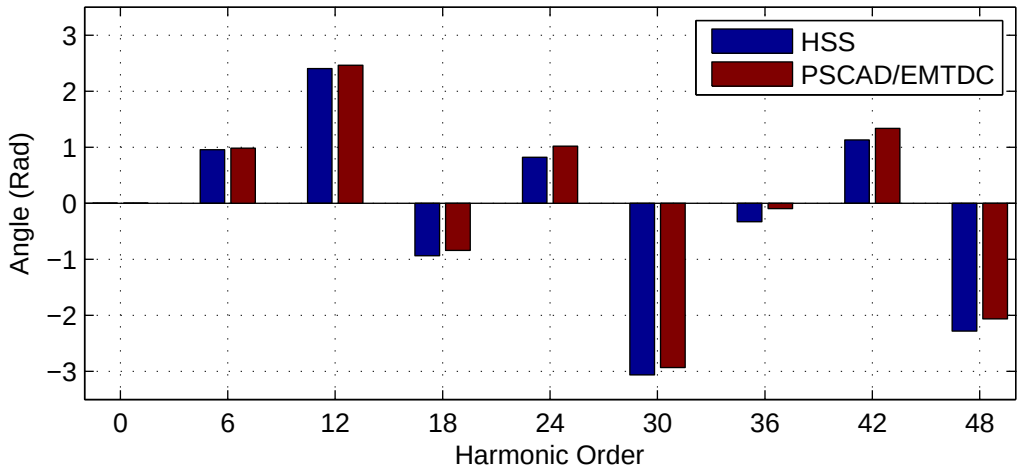

(b)

Figure 4.24: The magnitude and angle of the small-signal dc side voltage harmonics resulting from a one percent increase in the base case ac side voltage: (a) The resulting magnitude of the dc side voltage harmonics normalised to the dc component. (b) The resulting angle of the dc side voltage harmonics.

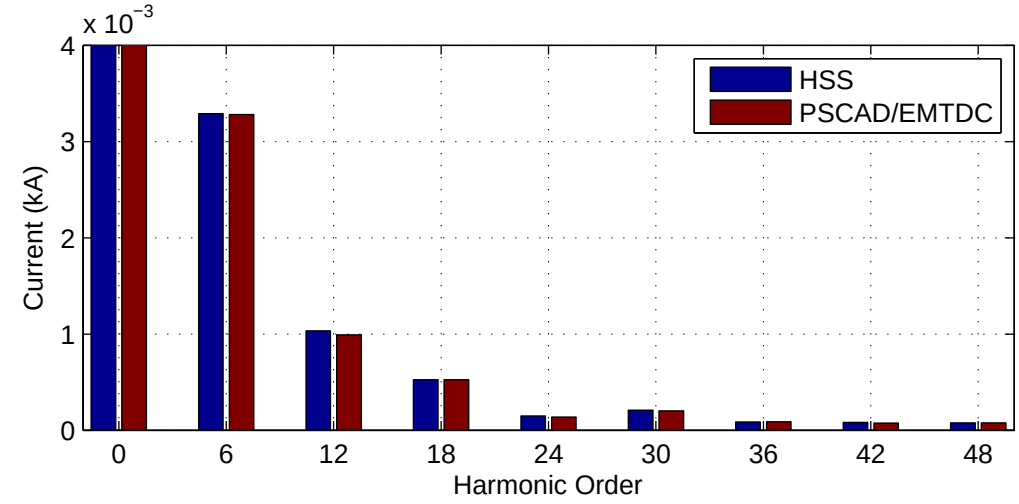

(a)

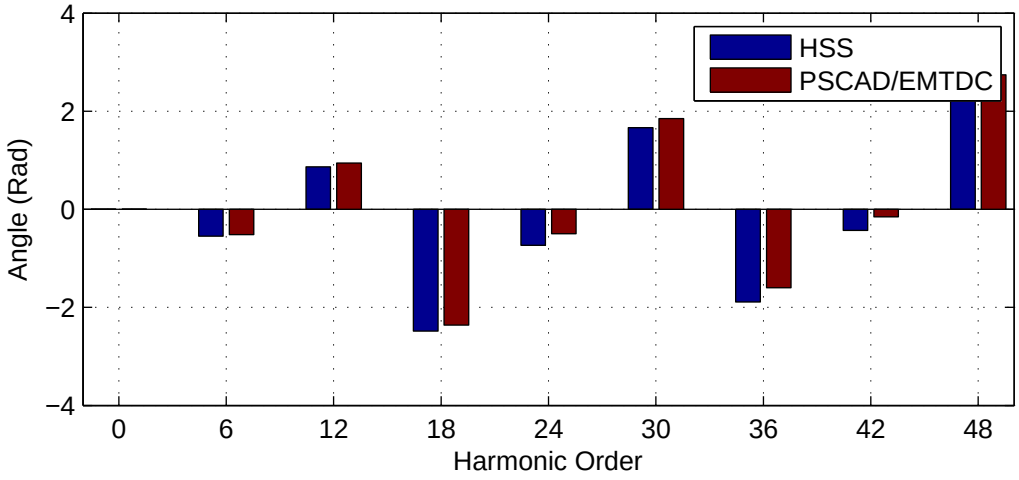

(b)

Figure 4.25: The magnitude and angle of the small-signal dc side current harmonics resulting from a one percent increase in the base case ac side voltage: (a) The resulting magnitude of the dc side current harmonics normalised to the dc component. (b) The resulting angle of the dc side current harmonics.

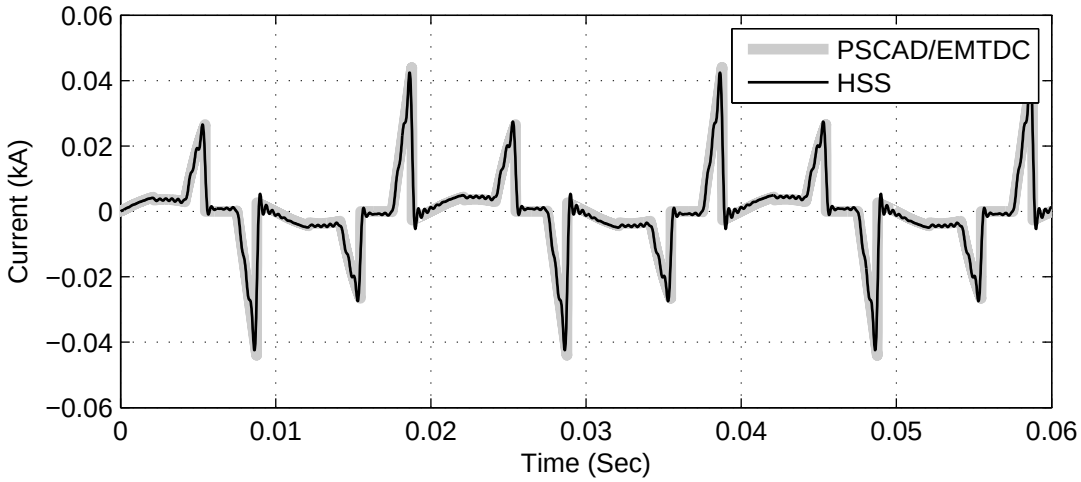

(a)

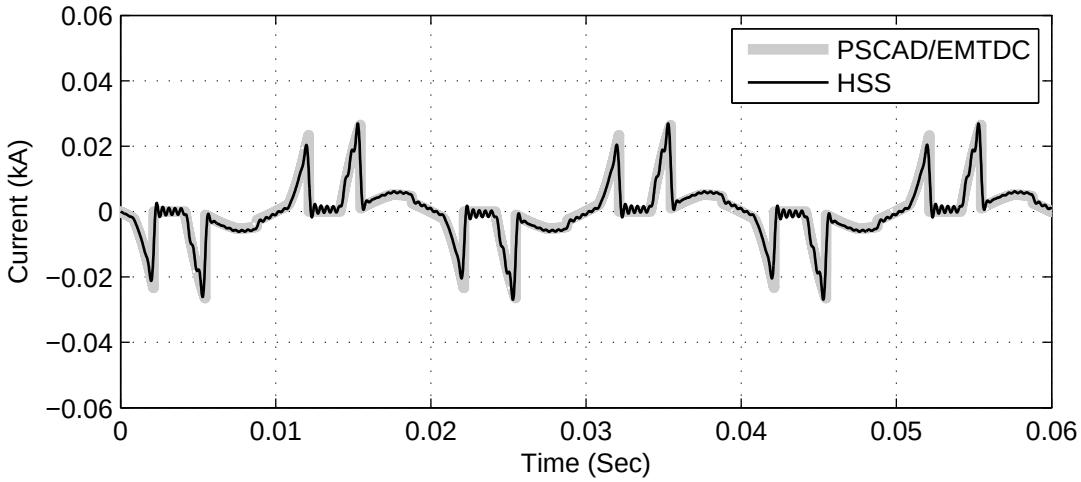

(b)

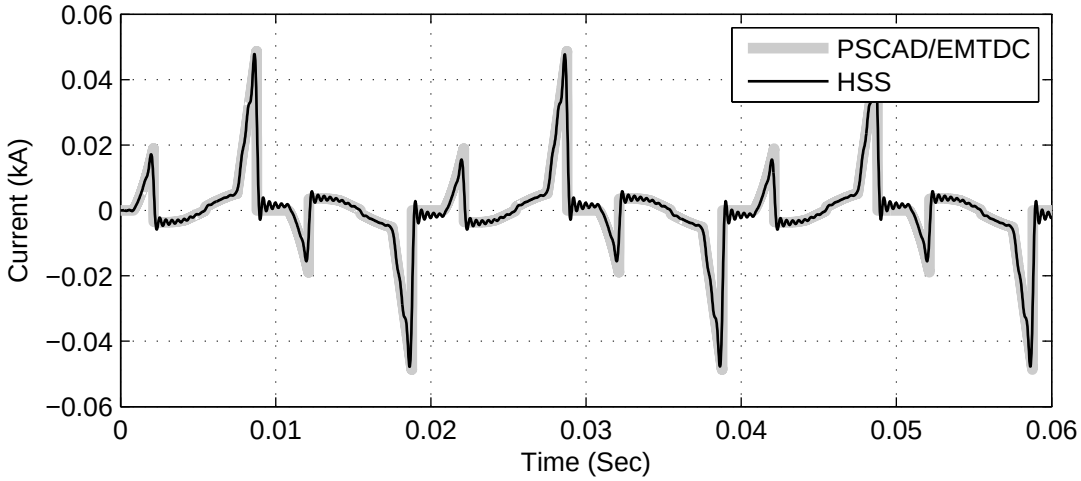

(c)

Figure 4.26: The transient response of the ac side currents resulting from a one percent negative sequence voltage injection at fundamental frequency: (a) The resulting phase a current waveform. (b) The resulting phase b current waveform. (c) The resulting phase c current waveform.

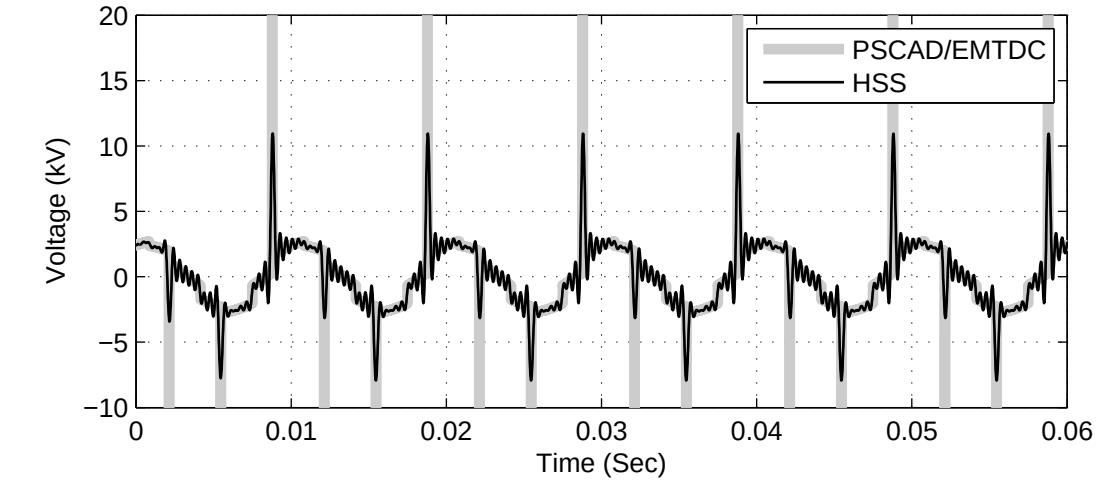

(a)

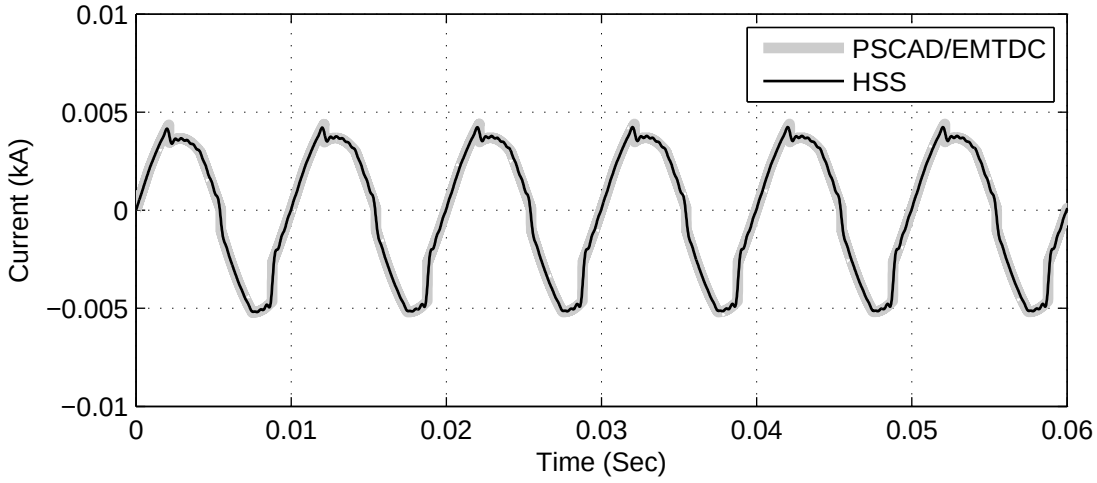

(b)

Figure 4.27: The transient response of the dc side voltage and current resulting from a one percent negative sequence voltage injection at fundamental frequency: (a) The resulting dc side voltage waveform. (b) The resulting dc side current waveform.

4.5 CONCLUSIONS

In this chapter, the development of an HSS model for a 6-pulse HVdc converter without active control is described. The frequency cross-coupling characteristic of the converter has been derived analytically and implemented as transfers between voltage and current signals. The state variables (inductor currents) in the HSS model have also been managed carefully, resetting them at particular switching instants to ensure correct time domain waveform trajectory.

A modular approach has been adopted in the construction of the HSS model, treating each system transfer as a separate subsystem, and the overall converter system is formed by connecting the inputs and outputs of each subsystem appropriately which is consistent with the classical description of an LTI system. This also allows the overall converter system to be examined systematically.

The HSS model is truncated to a relatively high harmonic order (up to the 49^{th} harmonic on the ac side and up to the 48^{th} harmonic on the dc side), and it only includes the characteristic harmonics of the converter. This way, the size of the model is significantly reduced, but the model still fully captures the frequency cross-coupling nature of the converter. Any harmonics not included in the model can be represented by an appropriate harmonic modulation from any reference frame as described in Sec. 3.10.

The accuracy of the HSS model has been demonstrated through some validations against a purely time domain model built using PSCAD/EMTDC. The results show good agreement between the two models under both steady-state and transient conditions. The subsequent chapter extends this HSS model to include an active controller exercising constant current control on the dc side.

Chapter 5

HARMONIC STATE-SPACE MODEL OF A CONTROLLED HVDC CONVERTER

5.1 INTRODUCTION

Active controls are often required for power electronic circuits to ensure their operation is as intended, this is true for the HVdc converter and all FACTS devices. The controllers associated with the power electronic circuits have a significant effect on the system steady-state and dynamic performance, thus it is of great importance to incorporate the associated controllers into the models of power electronic circuits.

Recent literature on the modelling of power electronic circuits has established that traditional steady-state models can be extended to capture the transient evolution of each individual harmonic through the use of *extended harmonic domain* (EHD), *dynamic harmonic domain* (DHD), or the *harmonic state-space* (HSS), but only a few of the models published attempt to incorporate feedback control.

In 2000, Mollerstedt published a HSS model of an inverter locomotive for a study of a harmonic instability that occurred in Switzerland [Mollerstedt 2000b]; this was perhaps the first dynamic model that includes multiple frequency coupling and a feedback control. Since then, both Garcia *et al.* and Orillaza *et al.* have published dynamic models of a controlled TCR through the use of DHD, and the HSS in [Garcia *et al.* 2011] and [Orillaza and Wood 2013] respectively. However, the prior uses numerical integration substitution (NIS) to solve for the exact thyristor switching instants and thus the model is time-variant. Orillaza *et al.* assumed fixed switching instants to gain a time-invariant representation in state-space, and used modulated impulses to incorporate the effects associated with switching instant variation (SIV). This approach enables the application of existing techniques in classical control theory to analyse the linear time-invariant (LTI) HSS, and is the direction taken up in this thesis.

In the previous chapter, an HSS model of a 6-pulse HVdc converter was presented, however there was no attempt to incorporate active feedback control. This chapter continues to build

on the uncontrolled converter model by incorporating a constant current controller on the dc side, and a simple ac system including a harmonic filter on the ac side. The pole-zero map of the overall system is observed, and an attempt to explain the dominant poles through the use of the concept of composite resonance is presented.

5.2 CHARACTERISTIC OF AN HVDC LINK

Typically for a HVdc link operating with a number of active controls, its dc side voltage-current characteristic can be best described by Fig. 5.1. The solid line represents the characteristic of the rectifier while the dashed line represents the characteristic of the inverter. The line AB corresponds to the rectifier operation when the firing angle is set to its minimum possible value, and it can be described by the following equation,

$$v_{dc} = \frac{3\sqrt{2}}{\pi} v_{ll} \cos\alpha - \frac{3X_{com}}{\pi} i_{dc} \tag{5.1}$$

where v_{ll} is the line-to-line voltage and X_{com} is the commutation reactance. The slope of this line is dictated by the commutation reactance at fundamental frequency, and it is an indication of the strength of the ac side system. The steeper this slope is, the weaker the ac side system. The minimum firing angle is typically set between 2 to 5 degrees to guarantee a minimum positive voltage for the thyristor valves to switch on [Sood 2004].

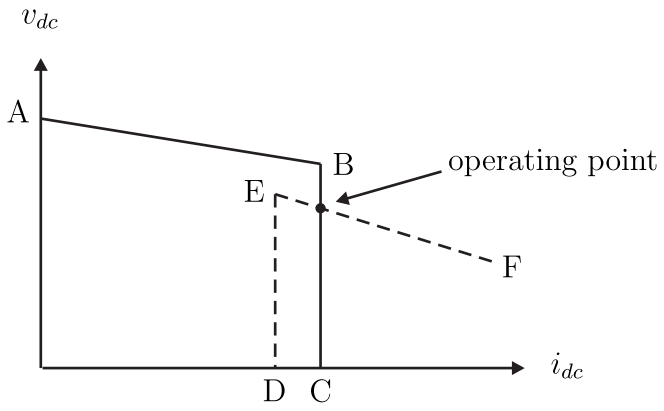

Figure 5.1: Typical dc side voltage-current characteristic of a HVdc link.

For a firing angle greater than the minimum firing angle, the constant current control becomes active and results in the vertical profile described by line BC in Fig. 5.1. When the firing angle is pegged at its minimum value, the current control on the inverting end takes over and the inverter operates somewhere along the dashed line DE. Normally, the inverter operates in constant extinction angle control which is described by the dashed line EF. Where the solid line and the dashed line intersects is the operating point of the HVdc link, and in order to create a unique operating point of the HVdc link, a current margin is maintained between the

rectifier and the inverter. For the purpose of this thesis, only the dynamics associated with the rectifier exercising constant current control is of interest, therefore the operating point of the rectifier may be chosen from any point along the line BC, and it is this chosen operating point that the small-signal model is linearised about. More importantly, Fig. 5.1 is merely a static representation of the operating point while the small-signal model captures the dynamic voltage-current relationship as the operating point varies with input distortion. The subsequent sections describe the development of an HSS model of a HVdc converter with constant current control that accurately captures its corresponding dynamic voltage-current characteristic.

5.3 VALVE-FIRING CONTROL

The modelling of the thyristor firing process is twofold, the first is associated with the thyristor firing controller, and the second is associated with the main converter controller[1]. Following its introduction in [Ainsworth 1968], the phase-locked oscillator (PLO) has become an essential component of the thyristor firing controller. The PLO tracks the fundamental component of the ac side terminal voltage, and generates equidistant timing references for the thyristor gate firing pulses. In general, harmonic distortion in the ac side terminal voltage has no influence to a well designed PLO, since its associated time constant is of the same order as the fundamental frequency [Arrillaga and Smith 1998][2]. In this thesis, the thyristor firing pulses are assumed to be perfectly separated by $\frac{\pi}{3}$ from each other, and consequently the PLO is not included in this model.

The constant current control strategy is often employed on the rectifying end of the HVdc link to regulate the dc side current, this ensures that the dc side current is maintained at a level that does not exceed the current rating of the thyristor valves even in the event of a dc side fault occurring [Adamson and Hingorani 1960]. If the dc side current varies due to some distortion at the system inputs, the main converter controller responds by adjusting the firing angle to give a dc side voltage such that the dc side current remains constant. Basically, decreasing the firing angle increases the dc side voltage, resulting in a larger dc side current, and similarly, the dc side current can be lowered by increasing the firing angle.

The main converter controller that regulates the dc side current consists of a current transducer with a low-pass filter, and a first-order compensator of the proportional integral type as illustrated in Fig. 5.2. The primary task for the current transducer is to provide a measurement of the actual dc side current, and compare it with the ordered dc side current. As the ordered dc

[1] This is a simplified control model, a practical converter system has considerably more complexity and employs multiple control schemes, namely, alpha minimum, constant voltage, and commutation margin control.

[2] In 1999, Jovcic *et al.* showed that the dynamics associated with a PLO can have significant impact on the stability of the system [Jovcic *et al.* 1999]. However, this was not pursued in this research and is considered as a possible future extension to the HSS model.

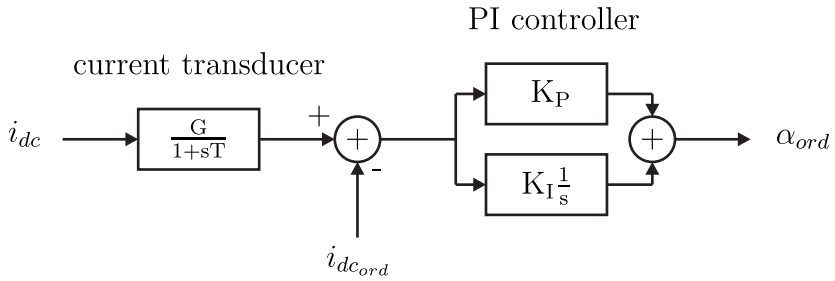

Figure 5.2: The main converter controller for constant current regulation.

side current is pre-specified in the control algorithm, and is most likely to be a steady dc signal during the normal operation of the main converter controller, the measurement of the actual dc side current is low-pass filtered to provide a relevant comparison between the two variables.

The difference between the two dc currents, also referred as the *current error*, is fed to the first-order compensator, and the compensator tries to generate an output control signal that eliminates this error. The control signal, also referred as the *ordered firing angle*, α_{ord}, is the input to the actuator which generates corresponding thyristor firing pulses that are fed to the gate of the thyristor valves to trigger the thyristor. Thus a closed-loop system is formed by including the process of the main converter controller in a feedback loop. The converter system with closed-loop control can be illustrated by the single line diagram in Fig. 5.3.

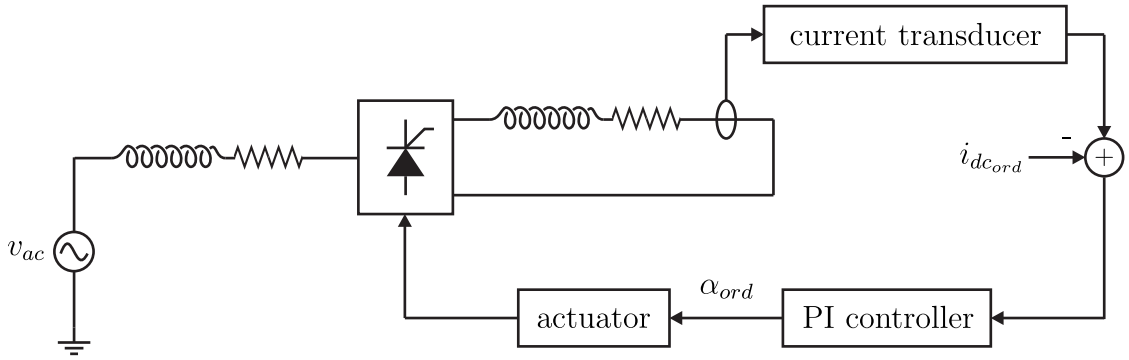

Figure 5.3: Single line diagram of a simplified HVdc converter with closed-loop control.

5.4 MODELLING OF CURRENT TRANSDUCER

The current transducer includes a first-order low-pass filter to reduce the effects of higher frequency harmonics. Its associated time domain response to a step input or an impulse input is an exponential rise or an exponential decay at the rate defined by its time constant, T_c, which corresponds to its cut-off frequency, ω_c, in the frequency domain. Hence in the frequency domain, the first-order low-pass filter attenuates the output magnitude beyond ω_c, and introduces a phase delay between the input and output signals. Note, beyond the cut-off frequency the

magnitude decays at -20 dB/dec and hence the higher frequency components that are close to the cut-off frequency may still contribute to the response of the main converter controller.

In the time domain, the first-order low-pass filter can be described by a set of state-space equations,

$$\frac{dx(t)}{dt} = -\frac{1}{T_c}x(t) + \frac{1}{T_c}u(t) \tag{5.2}$$

$$y(t) = x(t) \tag{5.3}$$

and its equivalent representation in the HSS is written as

$$sX = (-\omega_c\mathcal{I} - \mathcal{N})\,X + \omega_c\mathcal{I}U \tag{5.4}$$

$$Y = \mathcal{I}X \tag{5.5}$$

where $\omega_c = \frac{2\pi}{T_c}$ while $\mathcal{I}$ and $\mathcal{N}$ are diagonal matrices of ones and $jn\omega_0$ respectively. It can be observed that the first-order low-pass filter has a pole at the cut-off frequency, and by incorporating it in the feedback loop of the converter model, the dynamic performance of the main converter controller may be affected.

5.5 MODELLING OF PI CONTROLLER

The main purpose of the PI controller is to minimise the dynamic and steady-state difference between the measured dc side current and the ordered dc side current in this control scheme. The PI controller varies the firing angle of the thyristor valves to manage the voltage across the dc side terminals, consequently controlling the current flowing into the dc side. The proportional component of the PI controller produces an output that is proportional to the magnitude of the current error input while the integral component produces an output that is proportional to both the magnitude and the duration of the current error input. Generally, the proportional term speeds up the transient response and increases overshoot while the integral term eliminates steady-state error.

The time domain state-space equations of a PI controller for constant current control can be written as

$$\frac{dx(t)}{dt} = K_I \cdot i_{dc_{error}}(t) \tag{5.6}$$

$$y(t) = x(t) + K_P \cdot i_{dc_{error}}(t) \tag{5.7}$$

where $i_{dc_{error}}(t) = i_{dc}(t) - i_{dc_{ord}}(t)$ while K_P and K_I denote the proportional gain and the integral gain respectively. The equivalent HSS representation of the PI controller can be written

as

$$sX = -\mathcal{N}X + K_I\mathcal{I}I_{dc_{error}} \tag{5.8}$$

$$Y = \mathcal{I}X + K_P\mathcal{I}I_{dc_{error}} \tag{5.9}$$

and the output is the small-signal variation in firing angle, $\Delta\alpha$, measured in radians.

5.6 MODELLING OF ACTUATOR

In a physical actuator for the thyristor valves, its control signal input determines the timing of the initial rise of its output firing pulses which consequently controls the switching instants of the thyristor valves, more specifically, the thyristor switch-on instants. However, in this HSS model of an HVdc converter system, the switching instants of the thyristors have to be predetermined and remain unvaried during the simulation to retain an equivalent representation as an LTI system. Thus, the associated actuator in this model should not alter the switching instants used in the system transfer functions, but instead it must produce the equivalent effects associated with switching instant variation. This type of SIV that is associated with the control is referred as *controlled switching instant variation*.

Similarly to the switching instant variation occurring at the end of the commutation period discussed in Chapter 4, the effects associated with switching instant variation at the beginning of the commutation period can also be incorporated by the use of an impulse train. The impulses, also referred as an *amplitude modulated impulse train* (AMIT), are generated at the base case firing instants, and modulated to produce an appropriate voltage-time area. The resulting AMIT is added to the dc side voltage waveform directly and is also applied across the commutation circuit on the ac side to incorporate the effect associated with SIV at the beginning of the commutation period into the ac side current waveform indirectly. The subsequent sections 5.6.0.1 and 5.6.0.2 describe the associated effects of a controlled SIV on the dc side and ac side waveforms, and their implementation through the use of an AMIT spectrum.

5.6.0.1 Controlled SIV for DC Side Voltage

In order to maintain a constant current on the dc side, the main converter controller adjusts the firing angle of the thyristors to exercise control over the dc side voltage. The dc side voltage increases if the firing angle is reduced, and similarly, the dc side voltage decreases if the firing angle is increased. Figure 5.4 illustrates the effect associated with a change in the firing angle on the dc side voltage waveform assuming the commutation period remains unchanged. The thin solid line represents the base case dc side voltage waveform while the dashed line represents the dc side voltage waveform resulting from a variation in firing angle, and the shaded area

represents the resulting gain or loss of voltage-angle area at the base case thyristor switch-on instant, α_0.

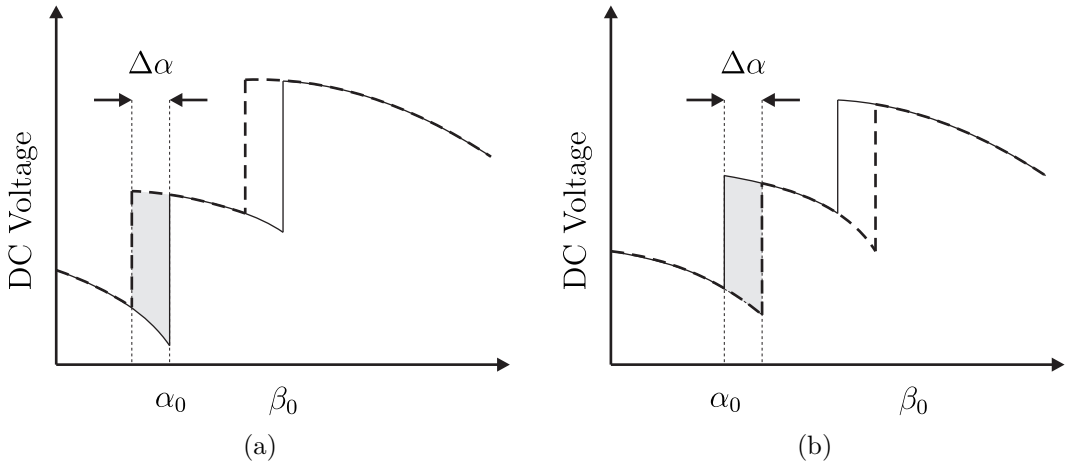

Figure 5.4: Graphical illustration of the consequences associated with controlled SIV on the dc side voltage waveform: (a) The firing angle is brought forward in time. (b) The firing angle is postponed in time.

Each fundamental period of the dc side voltage waveform of a 6-pulse converter is generated from six unique switching combinations of the thyristor bridge, and hence six voltage impulses must be incorporated into every fundamental period of the dc side voltage waveform to represent the effect associated with the firing angle variation. Given that this is a linearised model (i.e. the model is time-invariant), the voltage impulses are generated with reference to the base case firing angle of the converter, and more specifically the dc side voltage impulses resulting from a controlled SIV are fired at $\frac{\pi}{3}+\alpha_0$, $\frac{2\pi}{3}+\alpha_0$, $\pi+\alpha_0$, $\frac{4\pi}{3}+\alpha_0$, $\frac{5\pi}{3}+\alpha_0$, and $2\pi+\alpha_0$. Hence the AMIT spectrum used to generate the dc side voltage impulses can be written as

$$\begin{aligned}\delta_{d\leftarrow d}(t) = \sum_m \frac{1}{T}\Big[&e^{-jm\left(\omega_0 t+\frac{\pi}{3}+\alpha_0\right)} + e^{-jm\left(\omega_0 t+\frac{2\pi}{3}+\alpha_0\right)} \\ &+e^{-jm(\omega_0 t+\pi+\alpha_0)} + e^{-jm\left(\omega_0 t+\frac{4\pi}{3}+\alpha_0\right)} \\ &+e^{-jm\left(\omega_0 t+\frac{5\pi}{3}+\alpha_0\right)} + e^{-jm(\omega_0 t+2\pi+\alpha_0)}\Big]\end{aligned} \tag{5.10}$$

where ω_0 is the fundamental frequency measured in radians per second while T is the fundamental period measured in seconds, and $m = [..., -12, -6, 0, 6, 12, ...]$.

Each impulse of the AMIT in (5.10) needs to be modulated to give a correct voltage-time area at its associated thyristor switch-on instant which consequently results in a correct dc side current waveform through the integration done by the dc side smoothing inductor. The AMIT spectrum samples the small-signal variation in the firing angle determined by the PI controller, and the samples are modulated to give approximations to the voltage-time area (also referred as the

indirect area) indicated in Fig. 5.4. This can be written mathematically as

$$A_{indirect} \approx \frac{v_{ll}|_{\alpha_0}}{2\omega_0}\delta_{d\leftarrow d}(t)\Delta\alpha(t) \tag{5.11}$$

where $v_{ll}|_{\alpha_0}$ is the ac side line-to-line voltage at the base case thyristor switch-on instant, and the division by ω_0 is required to convert a voltage-angle area to a voltage-time area. Note that the 2 times multiplier is absent in this case of sampling with an AMIT spectrum; this is due to the fact that $\Delta\alpha(t)$ is a continuous waveform whereas in Sec. 4.3.1 the samples were made at discontinuities in the ac side current waveform (i.e. sampling at a truncated step to zero).

It is expected that this linearised model will produce a slightly different firing angle variation to that of a full nonlinear model built in a time domain environment even when the dc side current is in good agreement. This is because the linearised model modulates the impulses with the ac side line-to-line voltage at the base case firing angle, and an equivalent nonlinear model samples along the sinusoidal line-to-line voltage waveform. Therefore, if the ac side line-to-line voltage at the base case firing angle is less than the piece of a sinusoid that the nonlinear model samples, the linearised model generates a firing angle variation that is bigger than what the nonlinear model produces in order to make the corresponding voltage-time areas equal. Similarly, if the ac side line-to-line voltage at the base case firing angle is greater than what the nonlinear model samples, the linearised model produces a smaller variation in the firing angle compared to an equivalent nonlinear model.

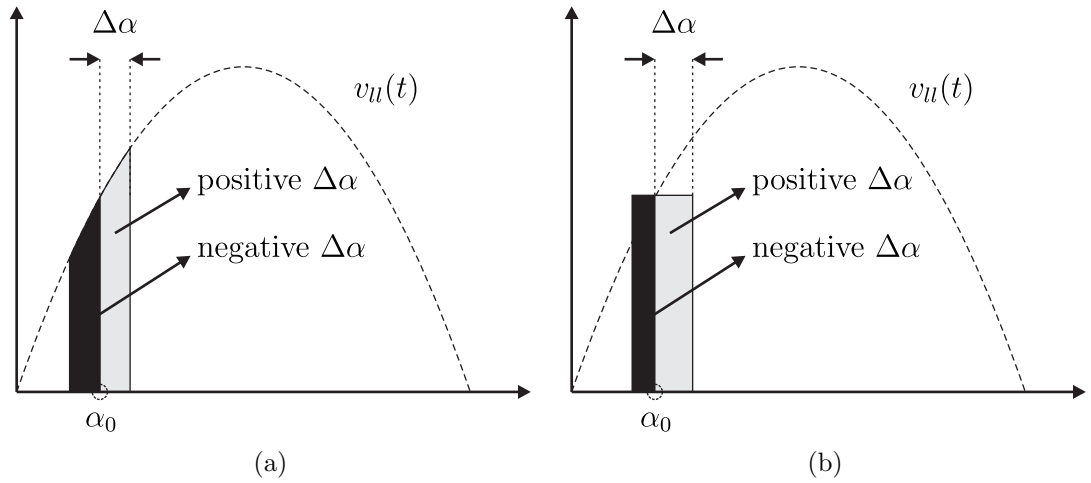

Figure 5.5: An exaggerated comparison of the voltage-time area associated with a controlled SIV produced by a nonlinear model and a linearised model: (a) Voltage-time area associated with a nonlinear model. (b) Voltage-time associated with a linearised model.

Figure 5.5 gives an exaggerated illustration of the voltage-time area resulting from a controlled SIV, and the differences between a nonlinear model shown in Fig. 5.5a and a linearised model shown in Fig. 5.5b can be identified. For an easy comparison the voltage impulses from the linearised model are time shifted, in reality, they should be centred at α_0. The dashed line

represents the ac side line-to-line voltage from 0 to π while the areas enclosed by solid lines represent the voltage-time area associated with a controlled SIV, more specifically, the light shaded areas result from a delay in firing angle, and the darker shaded areas represent an advance in firing angle. In summary, if the small firing angle variation is positive, the PI controller from the linearised model produces a bigger $\Delta\alpha$ to generate an equivalent voltage-time area for a correct dc side current waveform, and vice versa.

5.6.0.2 Controlled SIV for AC Side Current

The method of incorporating the consequences of a controlled SIV on the ac side current waveform is very similar to the case of an autonomous SIV described in Sec. 4.3.1. That is the ac side current must be reset to an appropriate condition at the base case switching instants, more specifically the base case thyristor switch-on instants. Figure 5.6 gives an exaggerated illustration of the effect of a controlled SIV on the ac side current waveform, and the reset of current required at the base case thyristor switch-on instant for a correct linearised model. The solid line represents the base case ac side current while the dashed line represents the ac side current associated with a variation in the thyristor firing angle. The shaded region indicates the excess or lack of current-time area in the waveform if the ac side current is reset at the base case instant indicated by the red arrow. The method of resetting the ac side current ensures a correct waveform beyond the base case thyristor switch-on instants.

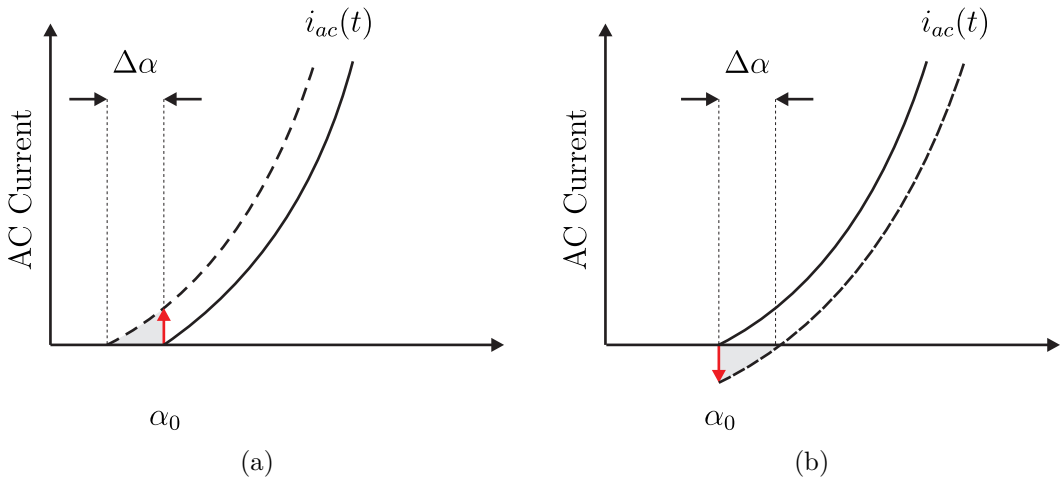

Figure 5.6: Graphical illustration of the consequences associated with controlled SIV on the ac side current waveform: (a) The firing angle is brought forward in time. (b) The firing angle is postponed in time.

The step in the ac side current waveform at the base case thyristor switch-on instant is achieved by applying a voltage impulse across the commutation circuit at that same instant. An AMIT spectrum centred at α_0 can be used to sample the variation in firing angle determined by the PI controller, and the samples are modulated to give the appropriate sized voltage impulses. The

voltage-time area required for each voltage impulse is approximated by

$$A_{v_{imp}} \approx L\frac{\Delta\alpha|_{\alpha_0}}{\omega_0} \cdot \left.\frac{di_{ac}}{dt}\right|_{\alpha_0} \tag{5.12}$$

where L is the inductive component of the commutation circuit while $\left.\frac{di_{ac}}{dt}\right|_{\alpha_0} = \frac{v_{ll}|_{\alpha_0}}{2L}$ is the slope of the ac side current at the base case thyristor switch-on instant α_0, and $\Delta\alpha|_{\alpha_0}$ is a sample of the small-signal firing angle variation at α_0.

Upon inspection, the voltage-time area calculated in (5.12) is exactly the same as the voltage-time area determined in (5.11) for the dc side voltage waveform. Thus, the dc side voltage impulses at α_0 can be applied to the commutation circuit directly. This can be done by the use of the sinusoidal sampling function described in (4.33) of Chapter 4, except in this case the sinusoidal sampling function is crossing its peak at α_0. Note, $m = 1$ for the transfer from the dc side voltage impulses to the positive sequence component of the voltage impulses while $m = -1$ for the transfer to the negative sequence component of the voltage impulses. Any consequential effect at the end of the commutation period due to a reset in the ac side current waveform at switch-on instants is taken care of by the state variable reset procedure described in Chapter 4. This concludes the analysis of the consequences associated with a controlled SIV in the ac side current and dc side voltage waveforms, and hence a complete feedback control is incorporated into the HSS model.

5.7 CLOSED-LOOP MODEL VALIDATION

In order to validate the closed-loop model built using the HSS, a time-domain model of an equivalent circuit built using PSCAD/EMTDC is simulated, and the small-signal responses are compared. The HSS model remains truncated to the 49^{th} harmonic on the ac side (48^{th} harmonic on the dc side) while the PSCAD/EMTDC simulation is conducted with a solution time step of 20 microseconds.

The base case quantities used in this simulation are essentially the same as the ones outlined in Table 4.1. However, due to the addition of the main converter controller a new set of base case switching instants have been obtained from a time domain simulation at the steady-state. The new set of base case switching instants along with the main converter controller settings are summarised in Table 5.1. In particular, the controller settings are chosen based on the *Cigre Benchmark Model for HVDC Controls*; as it is not the focus of this study, there was no attempt to optimise the performance of the main converter controller.

In this test, a one percent step decrease in the ac side voltage is applied to the closed-loop system. Figures 5.7 shows plots of the small-signal ac side currents resulting from the step change while

Table 5.1: Controlled 6-Pulse HVdc Converter Model Specifications

Parameter	Value	Unit
Base Case Firing Angle (α_0)	16.20	deg
Base Case Commutation Period (μ_0)	21.96	deg
Current Transducer Time Constant (T_C)	0.01	sec
Controller Proportional Gain (K_P)	62.9623	deg/A
Controller Integral Time Constant (T_I)	1.9059×10^{-4}	sec

Fig. 5.8 shows plots of the dc side voltage and current. The plots are zoomed in to the first three fundamental cycles to highlight the good agreement between the transient responses from the HSS model and the PSCAD/EMTDC model.

It is expected, in this case of decreasing the ac side voltage input, that the main converter controller would bring the firing angle forward in time to maintain the voltage across the dc side terminals and produce a consistent dc side current. This control action is clearly captured by the linearised HSS model as the positive voltage impulses at the base case firing angle α_0 shown in Fig. 5.8a which results in the correct dc side current waveform shown in Fig. 5.8b.

As described in Sec. 5.6.0.1, the PI controller in the HSS model is expected to produce a slightly different firing angle to the purely time domain model due to the linearisation of SIV. More specifically, the HSS model is expected to produce a smaller change in the firing angle than the time domain model when the firing angle is advanced and vice versa, but both models should have very similar transient response for the current error signal (the difference between i_{dc} and $i_{dc_{ord}}$) and eliminates steady-state error. This is clearly shown in Fig. 5.9a that the HSS model produces a smaller $\Delta\alpha$ in steady-state, and in Fig. 5.9b both models produces the same trajectory during the dynamic state and zero steady-state error. As a comparison, the small-signal response of the firing angle variation and the dc side current error due to a one percent increase in the ac side voltage is plotted in Fig. 5.10a and Fig. 5.10b respectively. In this case, the small-signal firing angle variation generated from the linearised model is greater than that of the time domain model at steady-state; this corresponds well to the discussion in Sec. 5.6.0.1.

This concludes the validation of the closed-loop HSS model, and in the succeeding section an ac side system with harmonic filters is implemented into the model to introduce a system resonance.

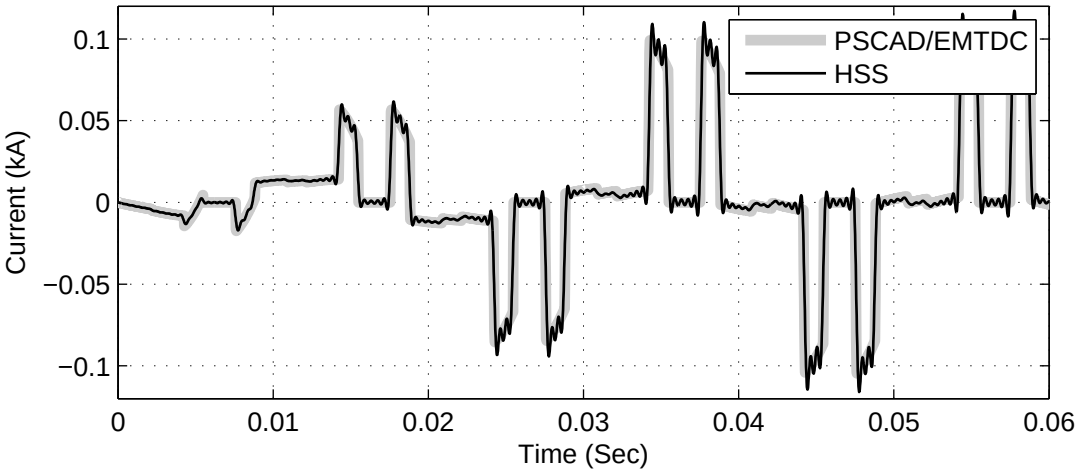

(a)

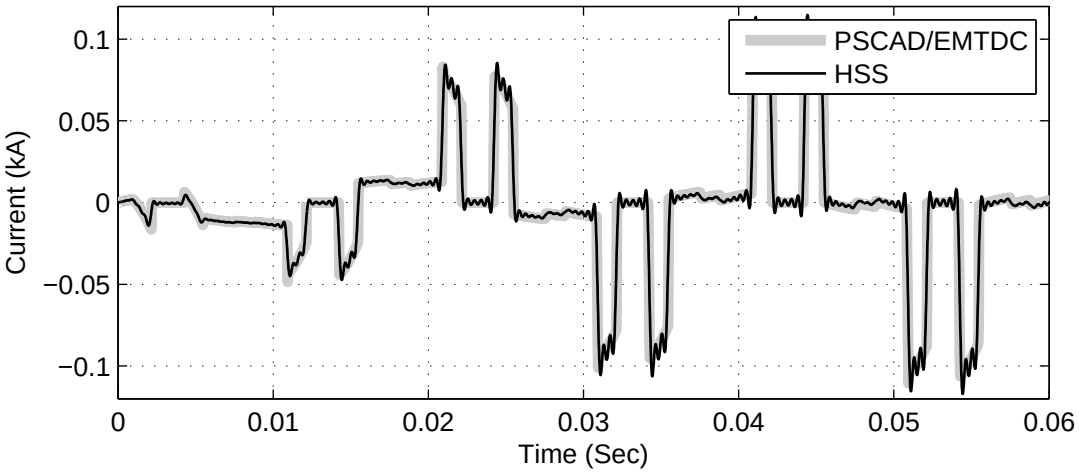

(b)

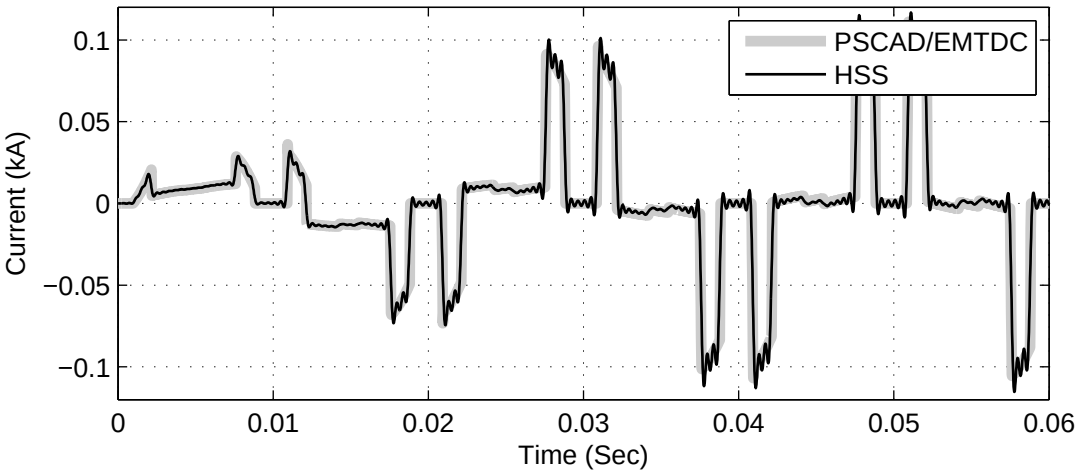

(c)

Figure 5.7: The transient response of the small-signal ac side currents resulting from a one percent decrease in the base case ac side voltage: (a) The resulting phase a current waveform. (b) The resulting phase b current waveform. (c) The resulting phase c current waveform.

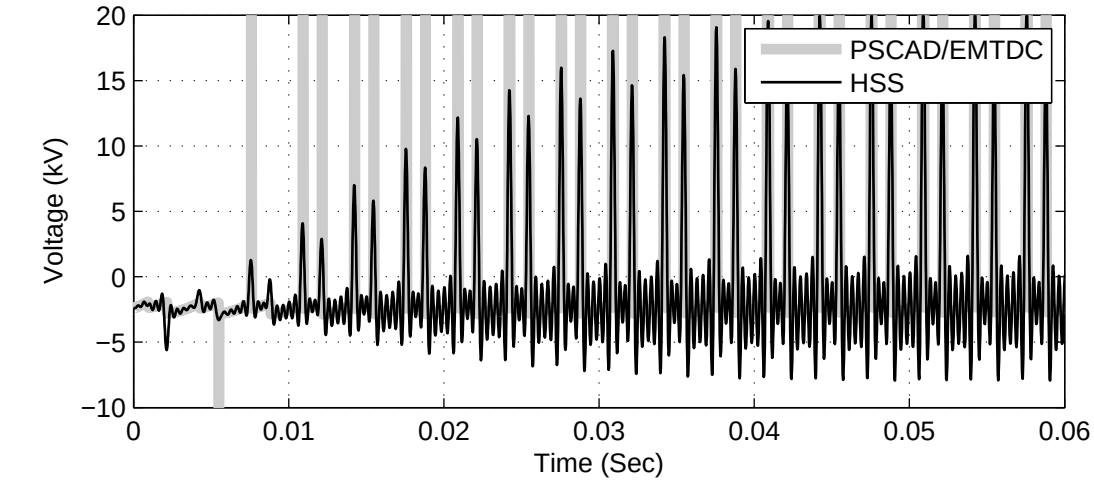

(a)

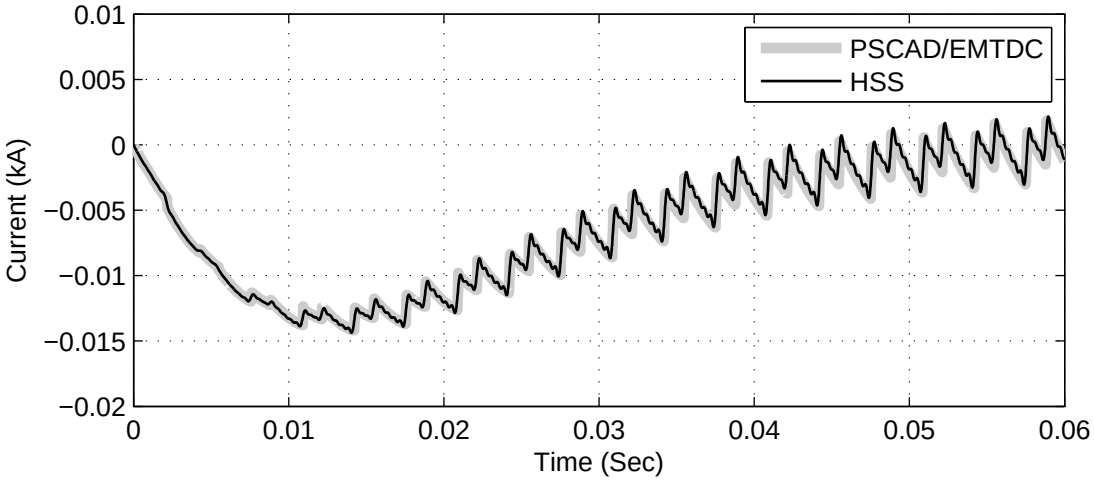

(b)

Figure 5.8: The transient response of the small-signal dc side voltage and current resulting from a one percent decrease in the base case ac side voltage: (a) The resulting dc side voltage waveform. (b) The resulting dc side current waveform.

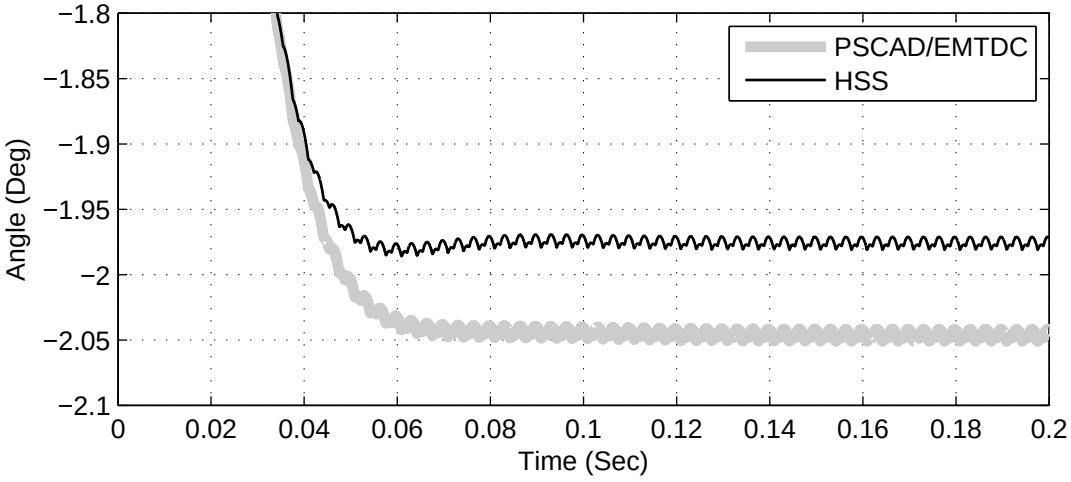

(a)

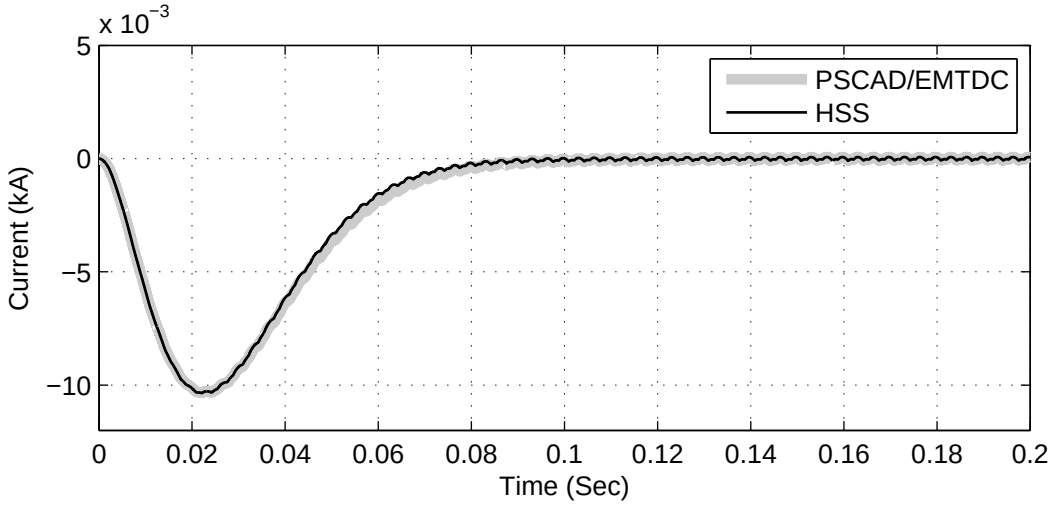

(b)

Figure 5.9: The transient response of the change in firing angle and the dc side current error resulting from a one percent decrease in the ac side voltage: (a) The resulting change in firing angle detailing the steady-state offset. (b) The resulting dc side current error.

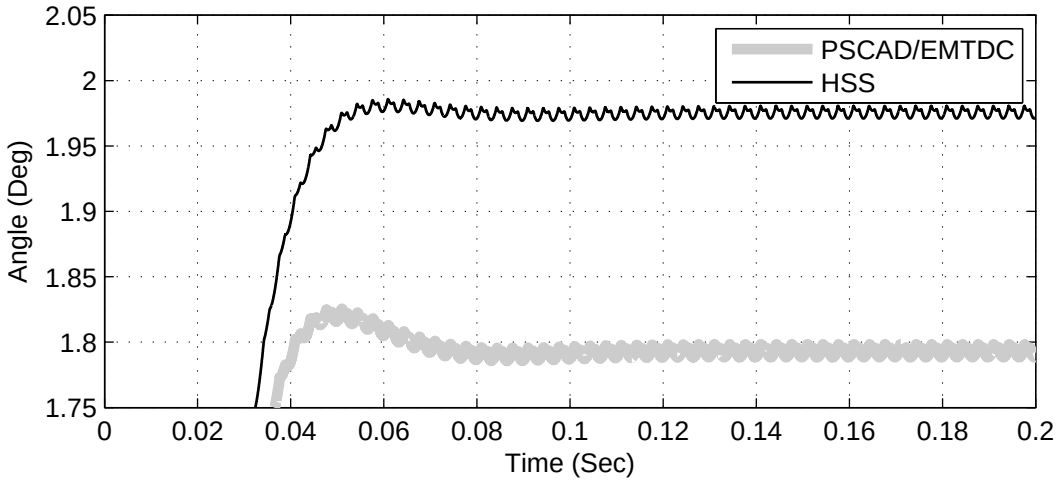

(a)

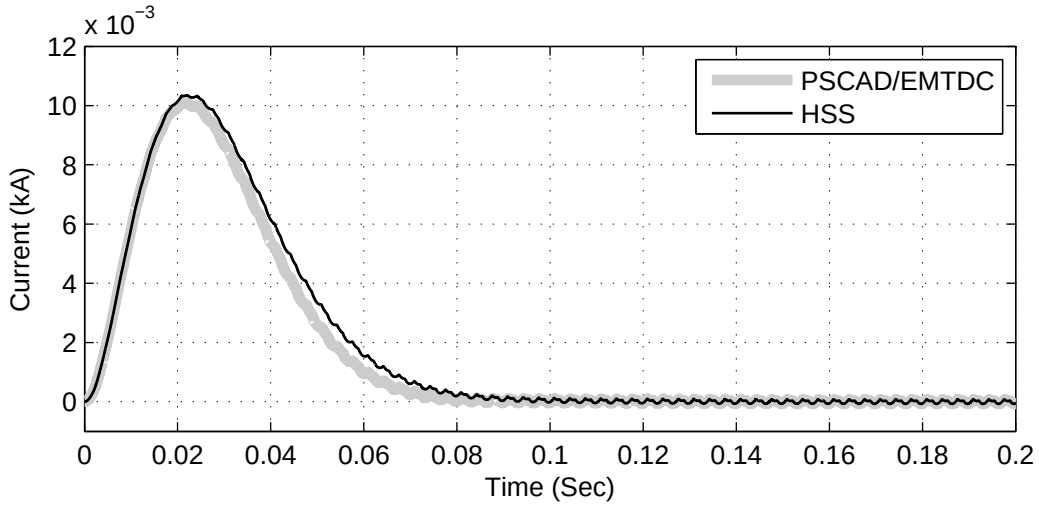

(b)

Figure 5.10: The transient response of the change in firing angle and the dc side current error resulting from a one percent increase in the ac side voltage: (a) The resulting change in firing angle detailing the steady-state offset. (b) The resulting dc side current error.

5.8 AC SIDE SYSTEM & HARMONIC FILTERS

Harmonic filters are usually installed on the ac side of a HVdc converter to provide low impedance paths for the harmonic currents to flow. This is to suppress the pollution of harmonics generated by the HVdc converter in the supply network [Sood 2004]. In this study, an ac system represented by a three-phase series RL circuit together with a three-phase 5^{th} harmonic shunt filter are installed on the supply side of the commutation circuit. Figure 5.11 shows the circuit diagram while Table 5.2 summarises the component values of the ac side system with shunt filter.

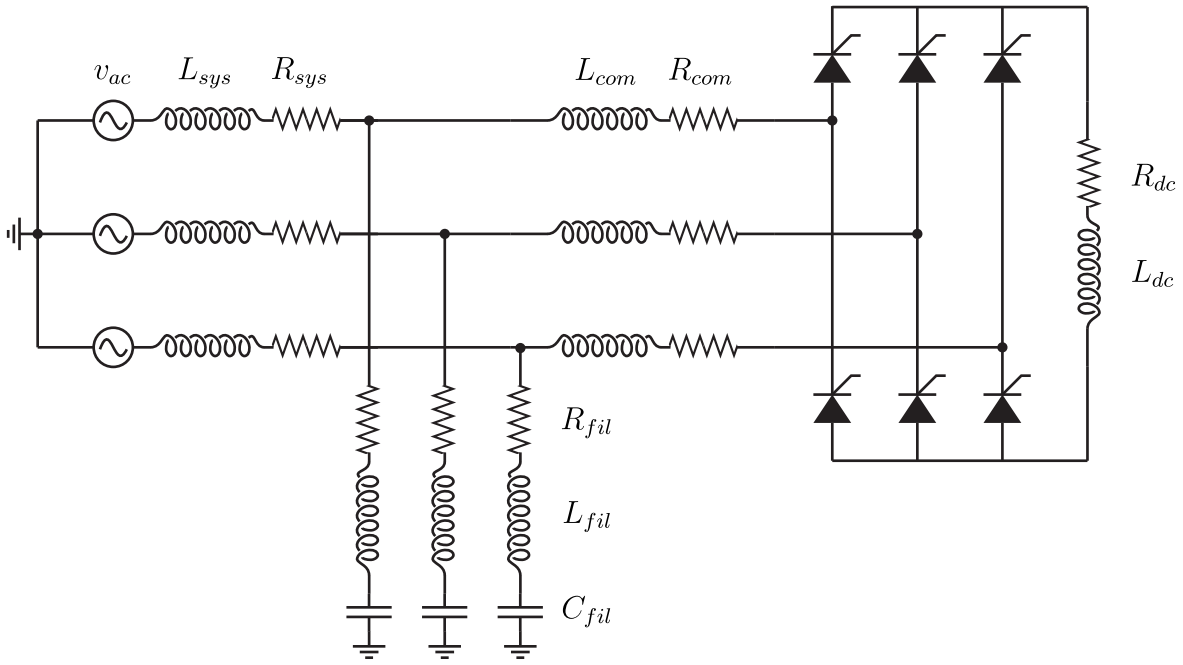

Figure 5.11: Circuit diagram of the HVdc converter model with an ac system.

Table 5.2: AC Side System and Shunt Filter Specifications

Parameter	Value	Unit
AC System Resistance (R_{sys})	1	mΩ
AC System Inductance (L_{sys})	30	mH
Shunt Filter Resistance (R_{fil})	1	Ω
Shunt Filter Inductance (L_{fil})	303	mH
Shunt Filter Capacitance (C_{fil})	1.37	μF

Traditionally, ac-dc systems with low *short circuit ratios* (SCR) are believed to be high potential candidates for system instability in the form of waveform distortion [Arrillaga *et al.* 1997]. This is because there exists a parallel resonance between the ac system inductance and the capacitor of the shunt filter, and this parallel resonance can be at a low frequency due to a high ac system impedance as indicated by a low SCR which may be excited under certain operating conditions and lead to an instability. However, this thesis presents a possible alternative cause

of waveform instability in a strong grid situation identified using the HSS model, and this is discussed throughout the succeeding sections.

5.8.1 Composite Resonance

The use of the term resonance (both series and parallel) is well established, and is commonly used to describe the peak or trough of impedance associated with a particular part of a system. In [Wood and Arrillaga 1995a], the concept of *composite resonance* is introduced specifically to approximate the overall system resonance by including the fundamental frequency conversion between the two sides of an HVdc converter.

The composite resonance of the HVdc converter system illustrated in Fig. 5.11 can be determined in two steps. First, a point near the converter is selected; in this instance it is the dc side terminals. Second, the equivalent impedances on both sides of the point are summed up, i.e. the impedance observed by looking into the dc side circuit and the impedance observed by looking into the converter. The summed impedance indicates a composite resonance at the frequency at which its imaginary component equals zero. The equivalent impedance observed from the dc side terminals looking into the converter takes into consideration of the converter characteristics, and in this case they are captured by a reduced version of the linearised three-port model presented in [Hume *et al.* 2002][3]. The model can be represented by a matrix multiplication written as

$$\begin{bmatrix} \Delta I_{acp}^{k+1} \\ \Delta I_{acn}^{k-1} \\ \Delta V_{dc}^{k} \end{bmatrix} = \begin{bmatrix} a & b & c \\ d & e & f \\ g & h & i \end{bmatrix} \begin{bmatrix} \Delta V_{acp}^{k+1} \\ \Delta V_{acn}^{k-1} \\ \Delta I_{dc}^{k} \end{bmatrix} \tag{5.13}$$

where k can be any positive real number, and the full detail of the three-port model derived by Hume *et al.* is given in Appendix C. A single resonant frequency on the ac side can be observed at two different frequencies from the dc side through the coupling to positive and negative sequence components, at higher and lower frequencies respectively.

Figure 5.12 shows a plot of both the real and imaginary components of the overall HVdc converter system impedance including both the ac side and the dc side circuits viewed from the converter dc side terminals as described above. This plot reveals the fact that there are two resonant frequencies $\omega_{n,1}$ and $\omega_{n,2}$ just below the 6^{th} harmonic when viewed from the dc side, they are shown by the zero-crossings of the imaginary component. More specifically, the first resonance occurs approximately at 287.8 Hz (12.2 Hz away from the 6^{th} harmonic) while the second resonance occurs approximately at 288.6 Hz (11.4 Hz away from the 6^{th} harmonic), and note that the damping at $\omega_{n,1}$ is higher than that of $\omega_{n,2}$. These resonances are well outside

[3] A similar model can also be found in [Larson *et al.* 1989].

the control bandwidth of the converter, and would not normally be expected to affect control dynamics.

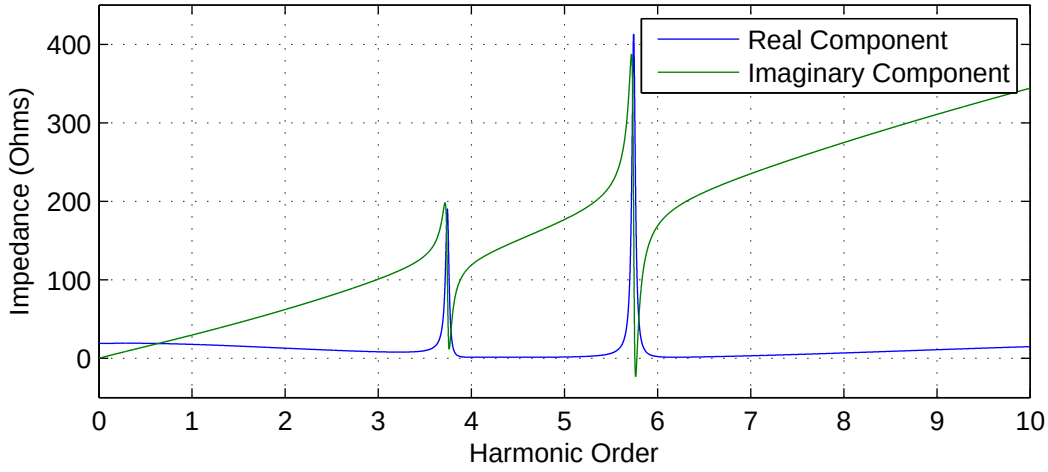

Figure 5.12: Impedance plot of the overall HVdc converter system viewed from the dc side.

5.9 OBSERVATION OF SYSTEM POLE-ZERO PLOTS

Posing the harmonics of the state variable as additional state variables introduces multiple reference frames in the HSS. This means that the same pole-pair is observable from all the reference frames that are included in the HSS model, i.e. the same pole-pair are reflected up and down along the imaginary axis in the s-domain plot. This is particularly well demonstrated by the pole-zero plot of a standalone series RL circuit, in this case the commutation circuit as shown in Fig. 5.13. The pole-pairs sit at $\frac{-R_{com}}{L_{com}} \pm jh\omega_0$ where $h = [-7, -5, -1, +1, +5, +7]$ the characteristic harmonics included in the model. The real component of each pole represents the damping while its imaginary component represents its damped frequency.

It is expected that resonant frequencies identified in the previous section can also be observed as dominant pole-pairs in the pole-zero plot for the associated HSS model. This is indeed the case, and as shown in Fig. 5.14, the two resonant frequencies $\omega_{n,1}$ and $\omega_{n,2}$ can be observed from different reference frames such that their mirror images can be found at frequencies $\omega_{p,1} = \pm\omega_{n,1} \mp h\omega_0$ and $\omega_{p,2} = \pm\omega_{n,2} \mp h\omega_0$. Unsurprisingly, the poles at $\omega_{p,2}$ are less damped compared to the poles at $\omega_{p,1}$ as they are closer to the imaginary axis which also corresponds with the composite resonance analysis. Furthermore, if the ac side system inductance is reduced from 30 mH to 20 mH, it is expected that the composite resonant frequencies will rise even closer to the 6^{th} harmonic when viewed from the dc side (or the 5^{th} harmonic when viewed from the ac side). This is clearly shown by the movement of the poles in Fig. 5.15.

As the composite resonant frequencies are very close to the 5^{th} harmonic (viewed from the ac

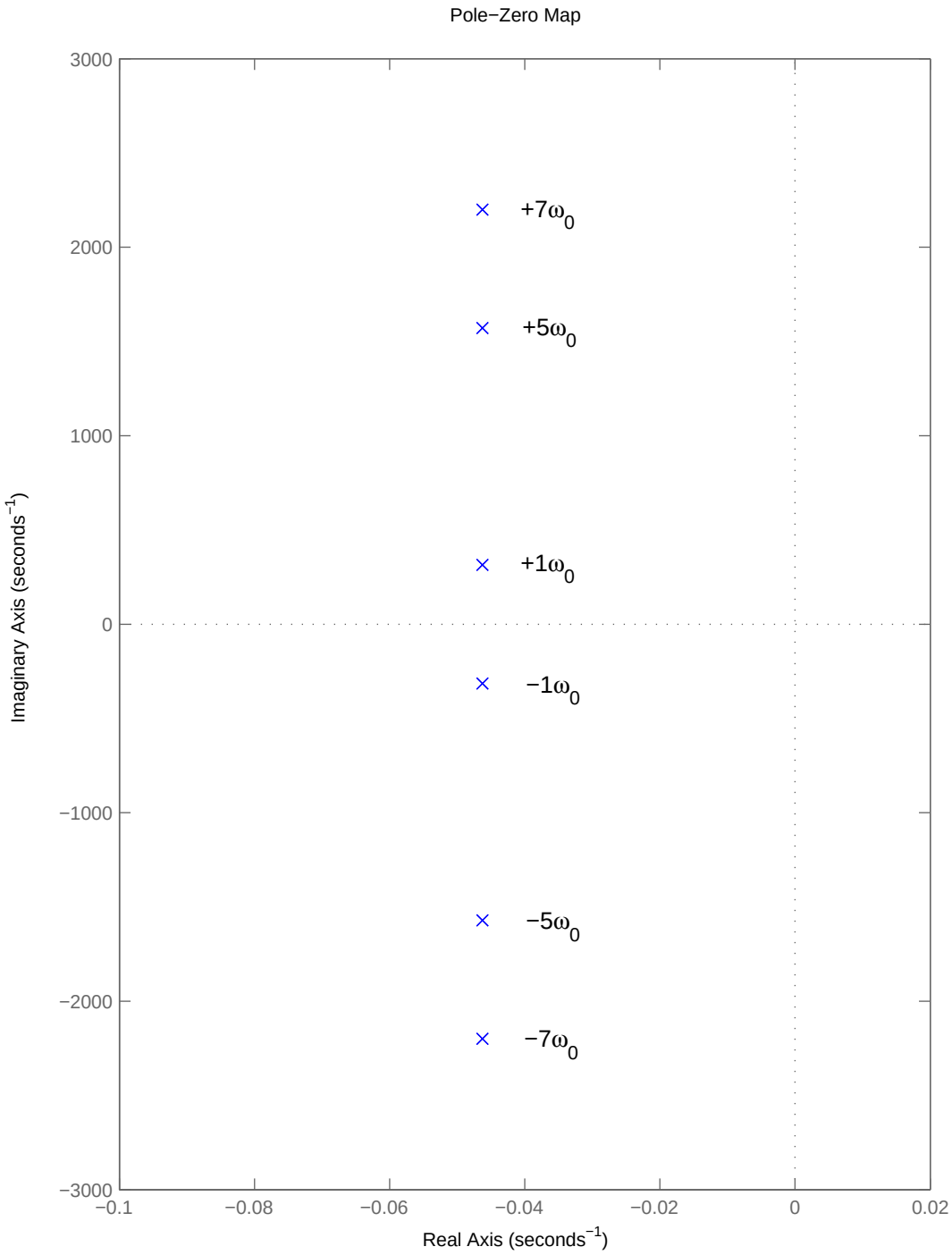

Figure 5.13: Pole-zero plot of the commutation circuit.

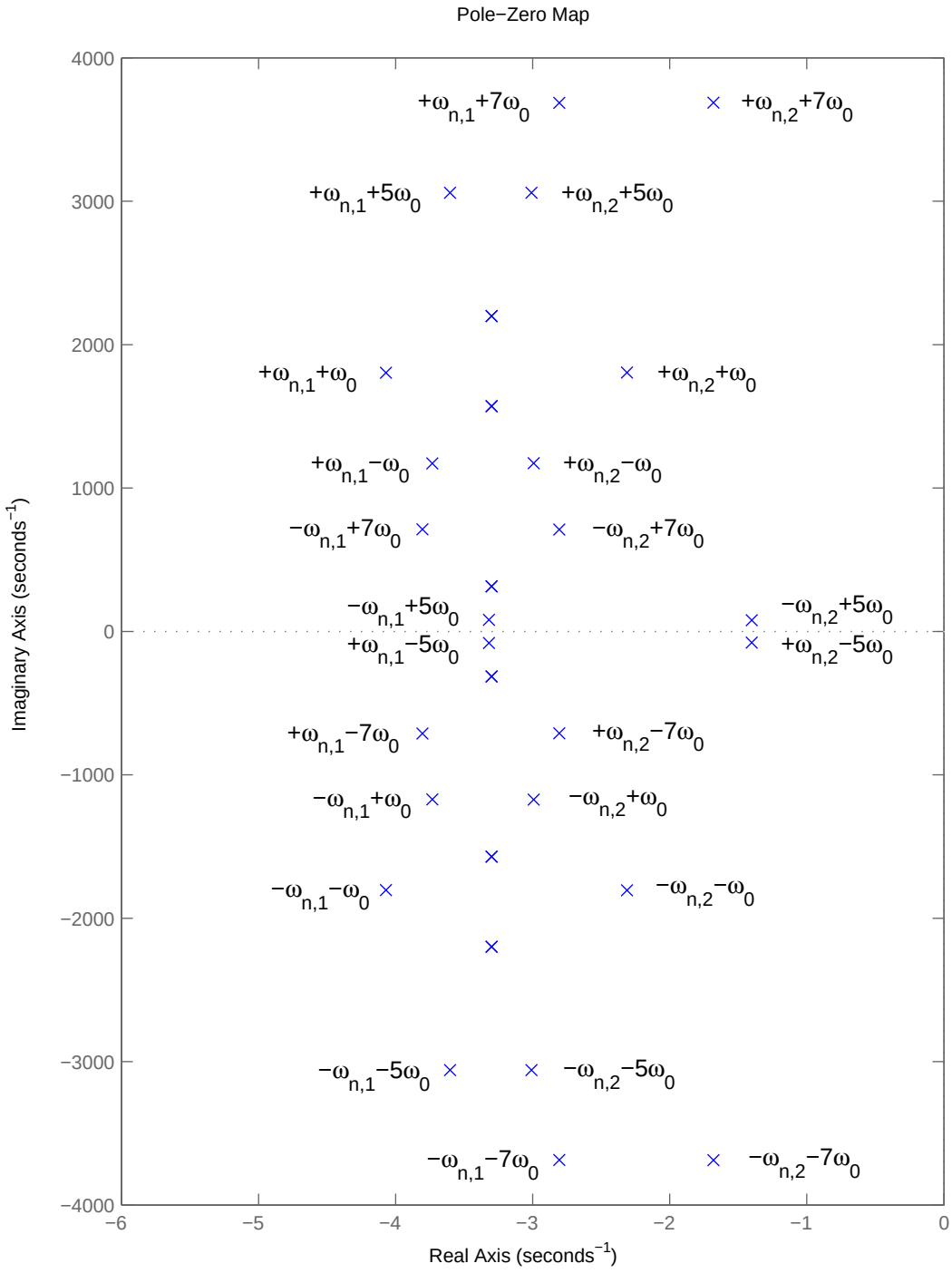

Figure 5.14: Pole-zero plot for the controlled HVdc converter model truncated to the 7^{th} harmonic and zoomed in to the dominant pole-pairs.

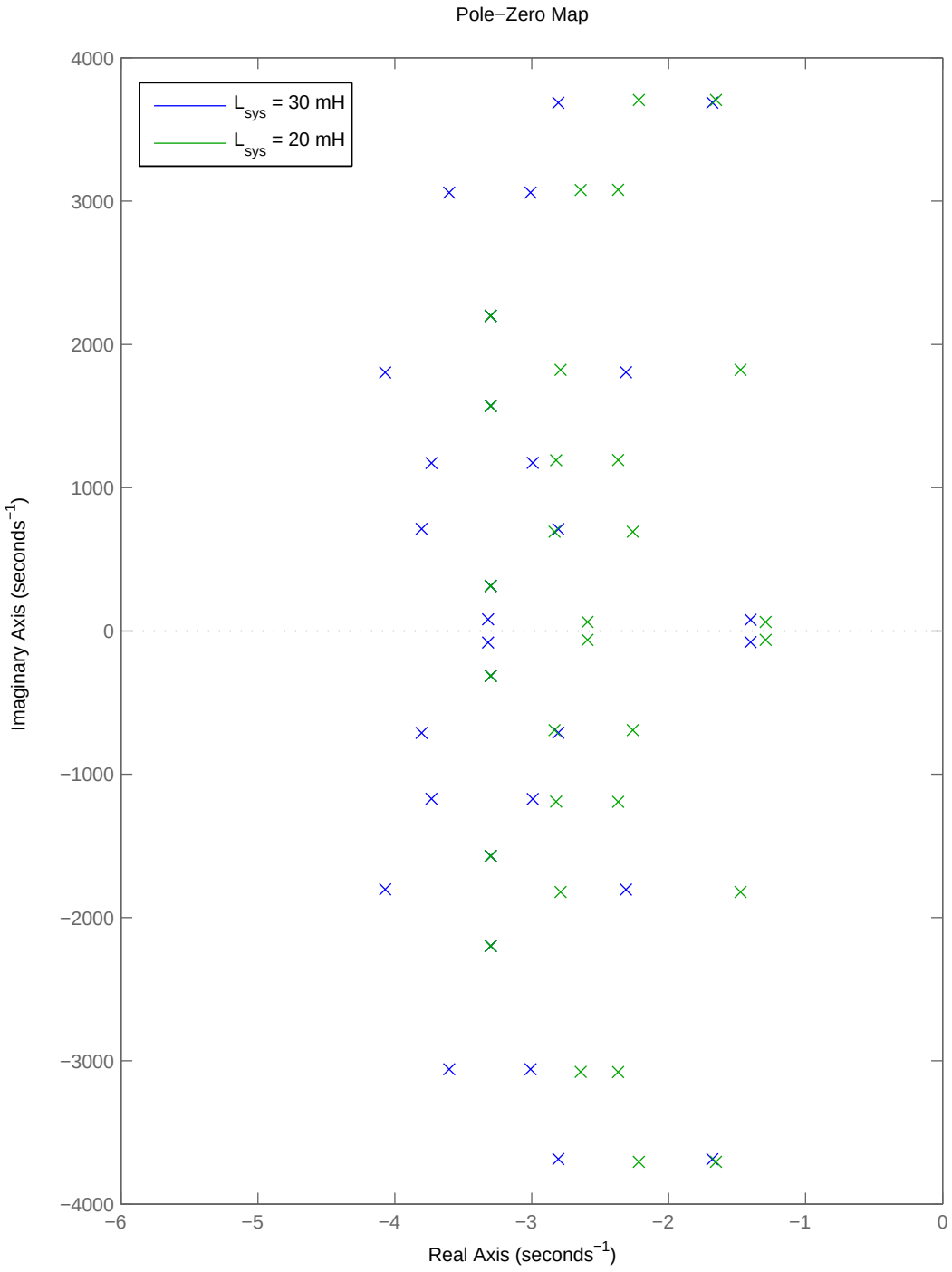

Figure 5.15: Pole-zero map showing the shift in poles due to a change in the ac side system inductance.

side) in this case, they are observed as low frequency poles from the 5^{th} harmonic reference frame. In addition, due to the strong coupling between the 5^{th} harmonic and the fundamental frequency through the 6-pulse converter, and the consequent strong coupling to the dc side zero frequency component, these low frequency poles fall within the bandwidth of the main converter controller (100 rad/s in this example). This means that the main converter controller acts on these low frequency poles and further reduces their damping through its associated gain. This can be seen from Fig. 5.14 that the poles at $\pm\omega_{n,2} \mp 5\omega_0 \approx 78.6$ rad/s (12.5 Hz) are by a considerable margin the least damped pole-pairs in the system.

The poles are the roots of the characteristic equation of the system. They each contribute to the overall system response in the form as an exponential decay of a sinusoid which can be written as

$$y(t) = Ae^{-\sigma t} sin\left(\omega_p t + \varphi\right) \tag{5.14}$$

where σ and ω_p represents the damping (real component) and frequency (imaginary component) of the pole while A and φ are determined by an initial condition. This means that the responses of each pole due to an excitation sum to generate the overall system response, and the response associated with the least damped poles should be the most visible oscillation during the transient state. This is clear by observing the small-signal response of the phase a current of the controlled HVdc converter system upon a one percent step excitation to the base case ac side voltage as shown in Fig. 5.16. Figure 5.16a shows good agreement between the responses generated from the HSS model and an equivalent PSCAD/EMTDC simulation in that a low frequency oscillation is visible from both models. Note that the HSS model is truncated to the 7^{th} harmonic on the ac side in this simulation. Figure 5.16b shows a plot of the phase a current harmonics evolving through time, a direct result from the HSS model, and all three harmonics exhibits an oscillation at approximately 12.5 Hz which is consistent with the previous discussion.

Finally, the same excitation (one percent step increase to the base case ac side voltage) is applied to an HSS model that is truncated to the fundamental frequency on the ac side. The time domain response of the phase a current is plotted in Fig. 5.17a while the transient evolution of the fundamental frequency component directly obtained from the HSS model is plotted in Fig. 5.17b. Note that in these plots the low frequency oscillation has vanished from the HSS model which proves that without including multiple reference frames (i.e. incorporating frequency coupling for the fundamental frequency only) the low frequency oscillation may be unnoticed. It also suggests that a purely fundamental frequency model built using techniques such as *dynamic phasor* or *generalised state-space averaging* cannot be used to identify the composite resonant frequency discussed in this example. This highlights the importance of modelling frequency cross-coupling for frequencies beyond the fundamental.

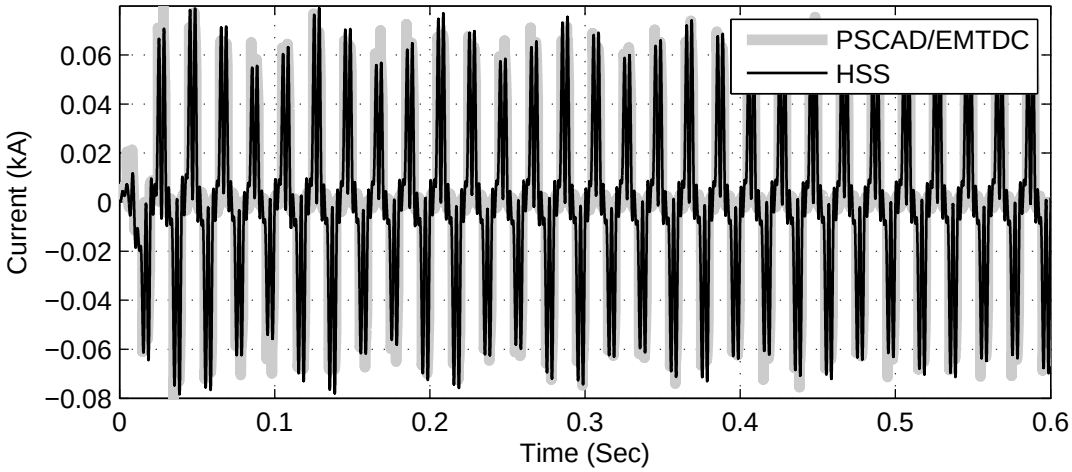

(a)

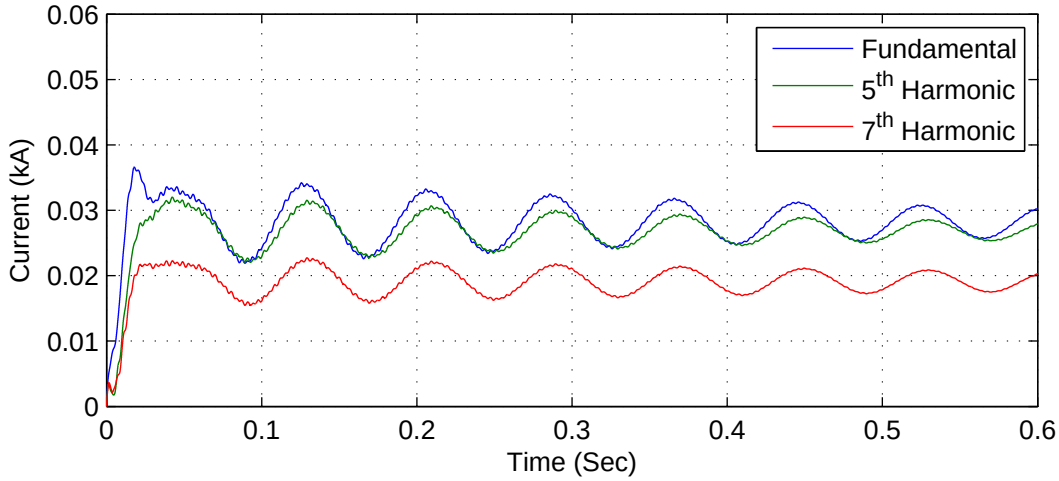

(b)

Figure 5.16: The transient response of the phase a current resulting from a one percent increase in the base case ac side voltage: (a) The time domain plot of the phase a current showing both results from an EMTDC/PSCAD simulation and the HSS model. (b) The time domain plot of the harmonics of the phase a current from the HSS model.

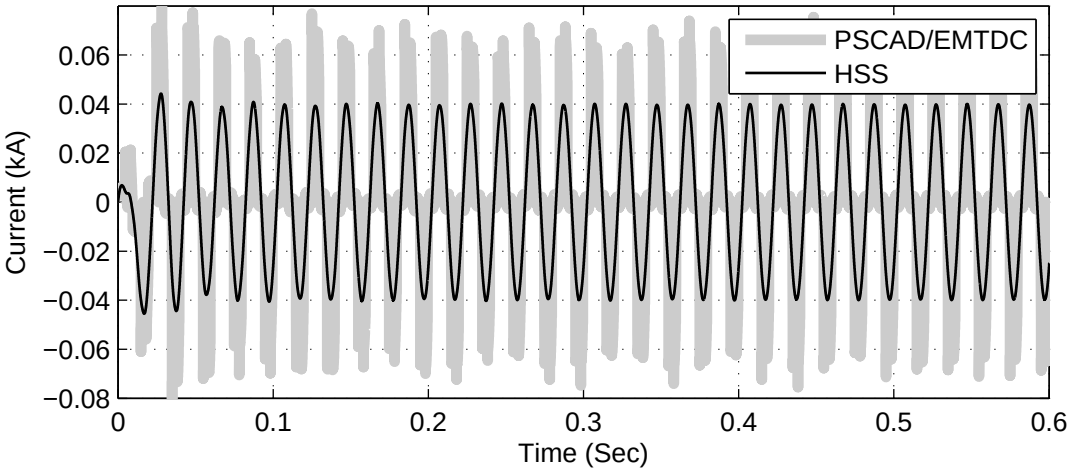

(a)

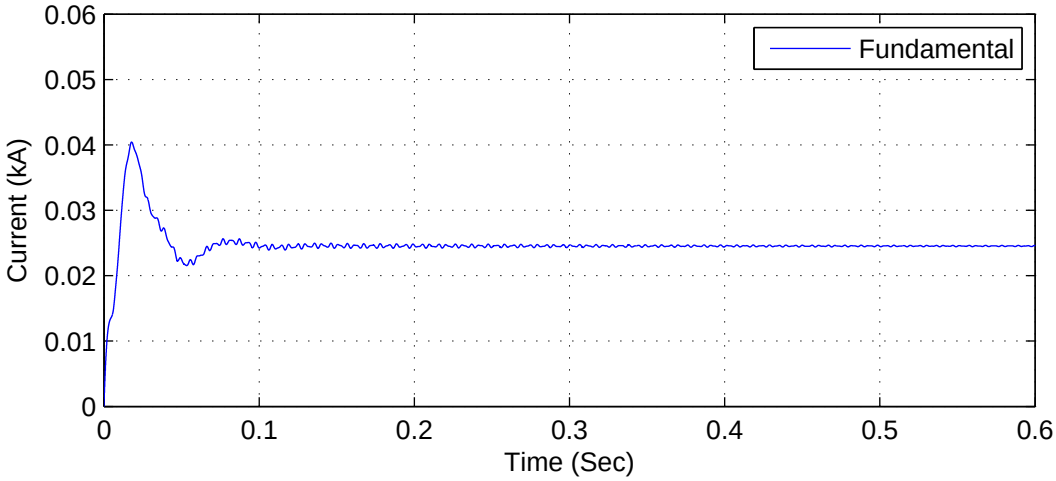

(b)

Figure 5.17: The transient response of the phase a current from an HSS model truncated to the fundamental frequency: (a) The time domain plot of the phase a current showing both results from an EMTDC/PSCAD simulation and the HSS model. (b) The time domain plot of the fundamental frequency component of the phase a current from the HSS model.

5.10 CONCLUSIONS

In this chapter, a closed-loop HSS model for an HVdc converter system with an active controller deploying constant current control has been developed. The main converter controller has been broken down into individual components; namely, the current transducer, the PI controller, and the actuator. The current transducer is modelled by a first-order low-pass filter; it provides a current error signal to the PI controller and may pose as a limitation on the bandwidth of the main converter controller. The PI controller is modelled by a set of first-order state-space equations that aims to minimise the current error through its proportional and integral gains. Finally, the actuator is modelled by applying voltage impulses to mimic the effects associated with a *controlled SIV* on the ac side current and the dc side voltage waveforms. The HSS model is validated against an equivalent model built using PSCAD/EMTDC. The step response to a one percent decrease to the base case ac side voltage was simulated, and the results show good agreement between the two models.

The concept of *composite resonance* was applied to determine the resonant frequencies of the HVdc converter with an simple ac side system including harmonic filters. The composite resonant frequencies were set up to be close to but not at the 5^{th} harmonic (a reference frame with strong frequency coupling to the fundamental), and it was shown through the pole-zero plots generated from the HSS model that the composite resonant frequencies can be identified as dominant pole-pairs in these s-domain plots. More importantly, due to the multiple reference frame environment embedded within the HSS, the composite resonant frequencies may be seen as low frequency oscillations from certain reference frames. In addition, if a strong coupling to a low frequency reference frame is present, as is true in this example, then the low frequency oscillations will also be present when viewed from a low frequency reference frame (observed from the dc side zero frequency reference frame in this case). Furthermore, if the low frequency oscillation falls within the bandwidth of the main converter controller, then the gain of the controller contributes to the reduction in the damping of the poles associated with the low frequency oscillation, amplifying their impact on the overall system response. Thus it is of great importance to incorporate the modelling of frequency coupling beyond the fundamental frequency to create a model that is useful for identifying possible system resonances.

The importance of frequency coupling for system dynamics has been shown for a simple single converter system. In the case where multiple converters may be electrically close, much more frequency coupling will occur. Whether this additional coupling has a stabilising or destabilising effect on the overall system is moot; however it is apparent that it is likely to have an effect, and should be explicitly modelled.

Chapter 6

CONCLUSIONS AND FUTURE WORK

6.1 CONCLUSIONS

As the technology in power electronics advances, it is certain that their penetration in the power system will continue to increase. Thus, it is important to understand their associated effects on system dynamics in order to ensure stable operation of the system. At the centre of this is the frequency cross-coupling characteristic of power electronic circuits. Traditional time domain based techniques, though well developed and widely accepted in software packages such as PSCAD/EMTDC or ATP-EMTP, are powerful simulation tools. However, time domain simulations are not the most suitable approach when it comes to controller design or stability analysis. Frequency domain or s-domain outshine time domain methods for these applications due to the wealth of control theory developed in these two domains. There is need for a new type of modelling technique to extend the traditional frequency domain or s-domain descriptions of a time-variant and nonlinear system to capture its dynamic evolution in the transient state while keeping a representation that is linear and time-invariant. The following subsections details the significant achievements in this thesis.

6.1.1 Linearisation Around an Operating Point

In this thesis, the procedures for developing a closed-loop HSS model of an HVdc converter operating as a rectifier with constant current control were described. The process began by defining an operating point for the converter system using thyristor switching instants. Generally speaking, these values can be obtained from a time domain based simulation or an iterative harmonic domain model. The former approach requires a time domain simulation with a three-phase ac side voltage set as the system input to process the entire transient state before the system relaxes to the steady-state; the cyclic steady-state converter waveforms are then used to extract thyristor switching instants. The latter approach requires an iterative harmonic domain model. The former approach was exploited in this thesis.

The linearisation around an operating point, defined by fixed thyristor switching instants, came at the cost of restricting the HSS model to be only applicable to small-signal analysis of the converter system[1]. However, it also meant that the model was formulated as a linear time-invariant (LTI) system in the frequency domain. This allows the application of classical control theory for stability analysis through the use of pole-zero plots and Nyquist plots, or for control design using root-locus techniques if required.

6.1.2 Harmonic Interactions Around the Converter

Frequency transfer functions have been analytically derived to capture the harmonic interactions around the HVdc converter including transfers for an active controller. Each transfer was built using time-invariant Fourier coefficients of a specific switching function that described the conduction pattern of the thyristor bridge. They each was posed in the form of a Toeplitz matrix which was also referred to as a frequency transfer matrix (FTM) in this thesis. Every FTM captured the mapping between two distinct signals, and the sum of their effects represented the overall operation of the converter. This modular approach allowed every transfer to be examined separately and that any existing switching function could be re-used. The switching functions were written in terms of the thyristor switching instants obtained from the procedure described in Sec. 6.1.1. As the switching instants were fixed throughout a simulation, the transfers remained constant even upon a distortion at a system input, and hence a linearised model was produced. Furthermore, the use of symmetrical components and characteristic harmonics ensured that the minimum set of Fourier coefficients required to fully represent the cross-coupling of frequencies around the converter was used. This was an important step in the development of the HSS framework to facilitate the modelling of a bigger power network with multiple power electronic devices.

6.1.3 Linear Time-Invariant State-Space Representation

The HSS model was represented by a linear time-invariant state-space (LTISS) system with its matrices, A, B, C, and D taking the form of a time-invariant FTM. Together with the use of the exponentially modulated periodic (EMP) signal basis, the evolution of each harmonic frequency of a system signal was tracked throughout the entire transient state as well as the steady-state. In addition, this formulation allowed the model to be applicable to standard LTI analysis techniques such as pole-zero plots, Bode plots, Nyquist plots, or root-locus. This made the HSS model a powerful tool for system stability studies and even controller design applications.

[1] According to Hume, the linearised transfers of a 6-pulse HVdc converter remain relatively accurate even when the system is experiencing waveform distortions up to 0.10 pu [Hume 2002].

6.1.4 Linearised Model for Switching Instant Variation

There is little doubt that switching instant variation (SIV) has significant effects on the converter waveforms, hence its contribution must be considered for an accurate model. It was clear from Hume's investigation that its associated effects can be linearised around an operating point [Hume 2002], and in this thesis, the approach of using the amplitude modulated impulse train (AMIT) spectrum was explored. The primary goal of an AMIT was to correct a voltage waveform in relation to a variation in the switching instants, and if that voltage was applied across an inductor, it must also correct the trajectory of the inductor current by creating a step in the waveform. The AMIT was in the form of a voltage impulse train with each impulse carrying an appropriate voltage-time area, and they centred at the same fixed switching instants as the transfer functions. Hence, this approach was also fully linearised. This way, the AMIT provided proper management for the current state variables in the model. It ensured that the thyristor current was kept to zero beyond its fixed switch-off instants, and started at the correct value at the fixed switch-on instants if there was any SIV resulting from the firing angle control.

6.1.5 Analysis of System Poles

System pole plots were used to examine the dynamics of the closed-loop converter system with a simple ac side system including a 5^{th} harmonic filter. Through the concept of composite resonance, the interaction between system impedances via the thyristor bridge was investigated and two resonant frequencies $\omega_{n,1}$ and $\omega_{n,2}$ were identified at 287.8 Hz and 288.6 Hz from the dc side. Normally these frequencies would not have been expected to affect the dynamics of the controller, but due to the cross-coupling between frequencies, they also appeared as low frequency components that fell within the bandwidth of the controller. The controller responded to these low frequency resonances and further reduced their damping. This was captured by the HSS model as the dominant pole-pairs in its s-domain plot which were reflections of the resonant frequencies up and down the imaginary axis. In addition, the poles within the control bandwidth were the least damped.

Reduction in the ac side system impedance showed a movement in the dominant pole-pairs that indicated an increase in the resonant frequencies. This confirmed that these dominant pole-pairs identified from the HSS model were associated with the resonant frequencies determined through the composite resonance analysis. It was also illustrated that if the system was truncated to only retain the cross-coupling between the fundamental and the dc component then these dominant dynamics cannot be captured. This highlighted the importance of preserving the representation of frequency coupling to a relatively high order harmonic.

6.2 FUTURE WORK

Through the HSS model presented in this thesis as well as some of the recent work published in [Love 2007] and [Orillaza 2012], it is clear that the HSS framework showed great potential in the dynamic modelling of power electronic systems. However, there are still some aspects of the HSS that requires further investigation, and a number of improvements can be made to the HVdc converter model. This section identifies some of the possible extensions to this research.

6.2.1 Gibbs Phenomenon

For a harmonically truncated model, there exists a source of inaccuracy known as Gibbs Phenomenon. This refers to the ringing on both sides of a discontinuity in the time domain waveform that is reconstructed from a frequency truncated spectrum. This means that the waveform oscillates around the actual value and the error is particularly significant at a discontinuity. In HSS modelling, sampling of current or voltage waveforms is often required at the thyristor switching instants for the modelling of SIV. Therefore, necessary approximations need to be made to produce proper samples of the steps in the current or voltage waveforms.

In this thesis, the property of half-wave symmetry was exploited and the sample made at a waveform discontinuity was approximated to be at midway of its actual value. This assumed the waveform has zero gradient before and after the step. However, this was not always the case. For example, in order to reset the state variable to ensure zero thyristor current during the non-conduction period, the thyristor current was sampled at the switch-off instant. Prior to the switch-off instant, the thyristor current was falling due to the commutation circuit, breaking the half-wave symmetry in the waveform. Worse, if there were multiple steps in the waveform, as was true for the small-signal ac side current waveform, the ringing associated with each step could have been affecting each other and making it even more difficult to approximate the actual size of the steps. An inaccurate sample of the thyristor current could have caused residual current beyond its switch-off and an error in the representation of SIV. Further investigations are required to produce better approximations at the waveform discontinuities, or alternatively ensuring the current state variables are kept zero during the non-conduction period. There is a possibility of using a square pulse instead of an impulse to reset the state variable so that further improvements can be made to the current waveform throughout the non-conduction period. An approach of eliminating Gibbs Phenomenon from switching functions proposed by de Souza and Watanabe may be investigated [de Souza and Watanabe 2009].

6.2.2 Model Extensions

The linearised HSS model of an HVdc converter presented in this thesis assumed equidistant firing pulses that were synchronised with the fundamental component of the supply side voltage and unaffected by harmonics, thus a phase-locked oscillator (PLO) was neglected from the model. However, the PLO had become an essential component in the valve-firing control since its introduction in [Ainsworth 1968], and Jovcic *et al.* have shown that the dynamic behaviour of the PLO can have significant impact on the system stability [Jovcic *et al.* 1999].

In 2004, Wood and Osauskas included a linearised model of the PLO in their frequency domain model of a STATCOM [Wood and Osauskas 2004]. It can be incorporated into the HSS model by rearranging its transfers using the HSS formulation described in Chapter 3. Furthermore, this HSS model can be extended to describe a 12-pulse converter system and eventually the full HVdc link with controls on both ends. In addition, there is a opportunity to integrate with other existing HSS models such as a TCR or a STATCOM for the study of a more complex system.

Appendix A

HVDC INSTALLATIONS BY ABB

ABB has participated in more than seventy HVdc projects around the world including the first commercial link in Gotland. A map of these links is shown in Fig. A.1 with its legends given in Table A.1.

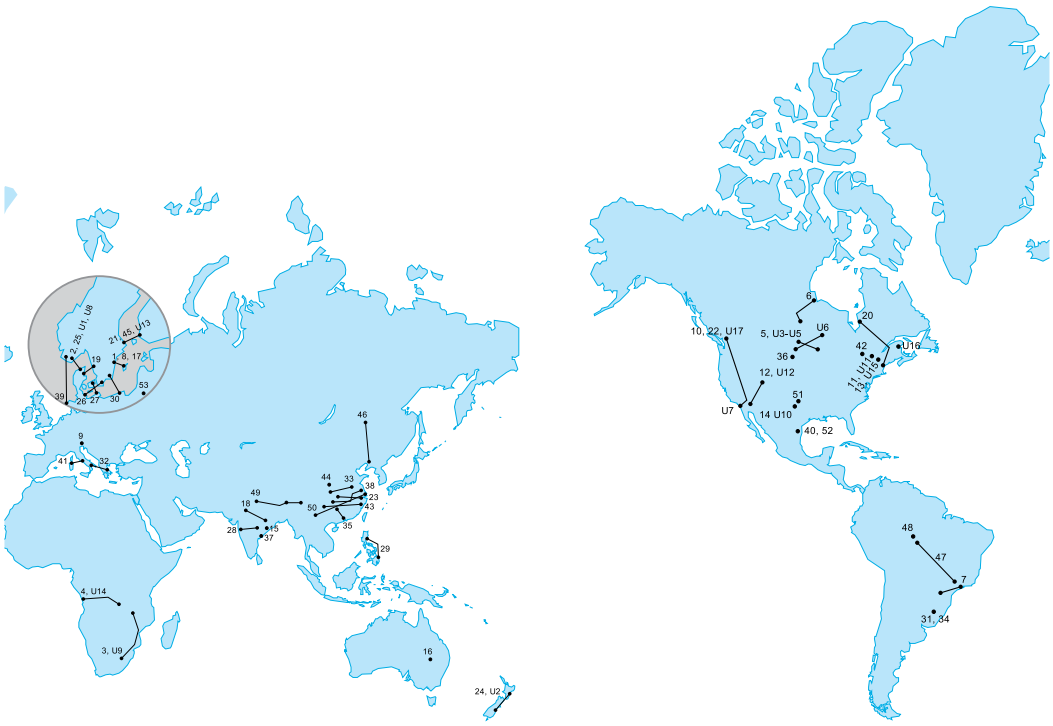

(a) Asia, Europe, Africa, and Australia. (b) North & South America.

Figure A.1: Map of HVdc installations by ABB.

Table A.1: ABB HVdc Classic Projects

Legend	Description	Legend	Description
1	Gotland	36	Rapid City DC Tie
2	Skagerrak 1 & 2	37	Vizag II
3	Cahora Bassa	38	Three Gorges - Shanghai
4	Inga-Kolwezi	39	NorNed
5	CU-project	40	Sharyland
6	Nelson River 2	41	SAPEI
7	Itaipu	42	Outaouais
8	Gotland 2	43	Xiangjiaba - Shanghai
9	Dürnrohr	44	Lingbao II Extension project
10	Pacific Intertie Upgrading	45	Fenno-Skan 2
11	Châteauguay	46	Hulunbeir - Liaoning
12	Intermountain	47	Rio Madeira
13	Highgate	48	Rio Madeira back-to-back
14	Blackwater	49	North-East Agra
15	Vindhyachal	50	Jinping - Sunan
16	Broken Hill	51	Oklaunion HVDC Replacement
17	Gotland 3	52	Railroad DC Tile (SHaryland)
18	Rihand-Delhi	53	LitPol
19	Konti-Skan 2	U1	Skagerrak 1 & 2
20	Quebec - New England	U2	New Zealand DC Hybrid Link
21	Fenno-Skan	U3-U5	CU-project
22	Pacific Intertie Expansion	U6	Square Butte HVDC Scheme
23	Gezhouba - Shanghai	U7	Pacific HVDC Intertie, Sylmar Replacement
24	New Zealand	U8	Skagerrak 1 & 2
25	Skagerrak 3	U9	Cahora Bassa, Apollo Upgrade
26	Baltic Cable	U10	Blackwater
27	Kontek	U11	Châteauguay
28	Chandrapur Padghe	U12	Intermountain Upgrade
29	Leyte - Luzon	U13	Fenno-Skan I Upgrade
30	SwePol	U14	Inga-Kolwezi Upgrade
31	Brazil-Argentina Interconnection 1	U15	Highgate Refurbishment
32	Italy-Greece	U16	Songo
33	Three Gorges - Changzhou	U17	Eel River
34	Brazil-Argentina Interconnection 2	U18	Pacific DC Intertie Celilo Upgrade
35	Three Gorges - Guangdong		

Appendix B

HARMONIC STATE-SPACE MODEL STRUCTURE

Figure B.1 shows the interconnection between the subsystems for the open-loop HSS model of an HVdc converter system.

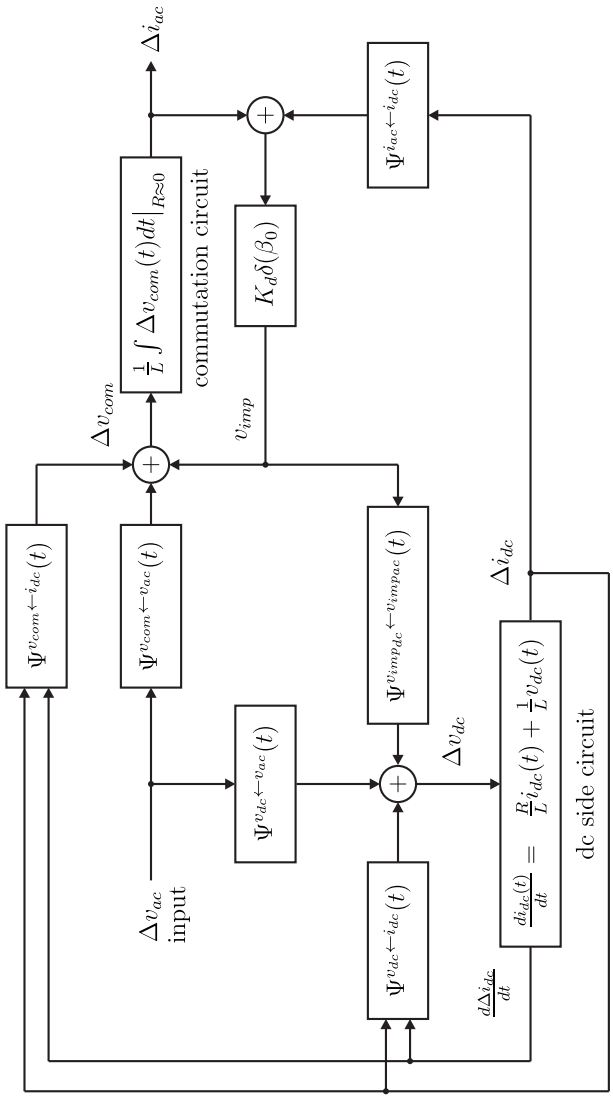

Figure B.1: HSS model structure of an uncontrolled HVdc converter system.

Appendix C

THREE-PORT TRANSFERS OF A 6-PULSE HVDC CONVERTER

The full three-port model of a 6-pulse HVdc converter including firing angle control can be described by a matrix multiplication given in C.1.

$$\begin{bmatrix} \Delta I_{acp}^{k+1} \\ \Delta I_{acn}^{k-1} \\ \Delta V_{dc}^{k} \end{bmatrix} = \begin{bmatrix} a & b & c & d \\ e & f & g & h \\ i & j & k & l \end{bmatrix} \begin{bmatrix} \Delta V_{acp}^{k+1} \\ \Delta V_{acn}^{k-1} \\ \Delta I_{dc}^{k} \\ \Delta \alpha^{k} \end{bmatrix} \tag{C.1}$$

The transfers a to l are described by the equations on the next page. The parameters V_1 and ϕ are the peak magnitude and the angle of the fundamental frequency positive sequence component of the ac side voltage respectively; α_0 is the firing angle while μ_0 is the commutation period in radians, and X is the commutation reactance in ohms. These transfers assume the current is flowing out from the converter into the dc side.

$$a = -j\frac{3\mu_0}{2\pi X(k+1)}\Big[1 - sinc\left((k+1)\mu_0/2\pi\right)\underline{/-(k+1)\mu_0/2}\Big] \tag{C.2a}$$

$$b = -j\frac{3}{2\pi X(k-1)}\underline{/-2(\alpha_0-\phi)}$$
$$\times\Big[sin(\mu_0)\underline{/-\mu_0} - \mu_0 sinc\left((k+1)\mu_0/2\pi\right)\underline{/-(k+1)\mu_0/2}\Big] \tag{C.2b}$$

$$c = -\frac{\sqrt{3}}{\pi}\underline{/-(\alpha_0-\phi)}\Big[-j - sin(\mu_0/2)\underline{/-\mu_0/2}$$
$$-(\mu_0/2)sinc\left((k+1)\mu_0/2\pi\right)\underline{/-(k+1)\mu_0/2}\Big] \tag{C.2c}$$

$$d = -\frac{3V_1\mu_0}{2\pi X}sin(\alpha_0)\underline{/-(\alpha_0)-\phi}$$
$$\times sinc\left((k+1)\mu_0/2\pi\right)\underline{/-(k+1)\mu_0/2} \tag{C.2d}$$

$$e = -j\frac{3}{2\pi X(k+1)}\underline{/+2(\alpha_0-\phi)}$$
$$\times\Big[sin(\mu_0)\underline{/+\mu_0} - \mu_0 sinc\left((k-1)\mu_0/2\pi\right)\underline{/-(k-1)\mu_0/2}\Big] \tag{C.2e}$$

$$f = -j\frac{3\mu_0}{2\pi X(k-1)}\Big[1 - sinc\left((k-1)\mu_0/2\pi\right)\underline{/-(k-1)\mu_0/2}\Big] \tag{C.2f}$$

$$g = -\frac{\sqrt{3}}{\pi}\underline{/+(\alpha_0-\phi)}\Big[+j - sin(\mu_0/2)\underline{/+\mu_0/2}$$
$$-(\mu_0/2)sinc\left((k-1)\mu_0/2\pi\right)\underline{/-(k-1)\mu_0/2}\Big] \tag{C.2g}$$

$$h = -\frac{3V_1\mu_0}{2\pi X}sin(\alpha_0)\underline{/+(\alpha_0)-\phi}$$
$$\times sinc\left((k-1)\mu_0/2\pi\right)\underline{/-(k-1)\mu_0/2} \tag{C.2h}$$

$$i = \frac{3\sqrt{3}}{\pi}\underline{/+(\alpha_0-\phi)}\Big[+j - sin(\mu_0/2)\underline{/+\mu_0/2}$$
$$+(\mu_0/2)\underline{/+\mu_0}sinc\left((k+1)\mu_0/2\pi\right)\underline{/-(k+1)\mu_0/2}\Big] \tag{C.2i}$$

$$j = \frac{3\sqrt{3}}{\pi}\underline{/-(\alpha_0-\phi)}\Big[-j - sin(\mu_0/2)\underline{/-\mu_0/2}$$
$$+(\mu_0/2)\underline{/-\mu_0}sinc\left((k-1)\mu_0/2\pi\right)\underline{/-(k-1)\mu_0/2}\Big] \tag{C.2j}$$

$$k = jkX(2 - 3\mu_0/2\pi) + (3X/\pi)cos(k\mu_0/2)\underline{/-k\mu_0/2} \tag{C.2k}$$

$$l = -\frac{3\sqrt{3}V_1}{2\pi}sin(\alpha_0)\Big[1 + \underline{/-k\mu_0}\Big] \tag{C.2l}$$

Appendix D

LIST OF PUBLICATIONS

Conference Papers:

1. Orillaza, J.R., Hwang, M.S. and Wood, A.R., 'Switching Instant Variation in Harmonic State-Space Modelling of Power Electronic Devices', presented at the *20th Australasian Universities Power Engineering Conference*, Christchurch, New Zealand, December 2010.

2. Hwang, M.S. and Wood, A.R., 'Harmonic State-Space Modelling of an HVdc Converter', in the *Proceedings of 15th IEEE International Conference on Harmonics and Quality of Power*, Hong Kong, June 2012, pp. 573-580. doi: 10.1109/ICHQP.2012.6381184

3. Hwang, M.S. and Wood, A.R., 'A New Modelling Framework for Power Supply Networks with Converter Based Loads and Generators - the Harmonic State-Space', presented at the *2012 IEEE International Conference on Power System Technology*, Auckland, New Zealand, October 2012. doi: 10.1109/PowerCon.2012.6401352

Journal Papers:

1. Hwang, M.S., Das, B.P., Wood, A.R., Watson, N.R. and Liu, Y., 'Experimental Validation of the Harmonic State-Space Model of a Graetz Bridge Converter', *International Transactions on Electrical Energy Systems*, August 2013. doi: 10.1002/etep.1787

2. Hwang, M.S. and Wood, A.R., 'Harmonic State-Space Modelling of a Controlled HVDC Converter', submitted to IEEE Transactions on Power Delivery.

REFERENCES

Acha, E. and Madrigal, M. (2001), *Power Systems Harmonics Computer Modelling and Analysis*, John Wiley & Sons, Ltd, Baffins Lane, Chichester, West Sussex, PO 19 1UD, England.

Adamson, C. and Hingorani, N. (1960), *High Voltage Direct Current Power Transmission*, Garraway Ltd, 11 Kensington Church Street, London, W.8.

Ainsworth, J. (1967), 'Harmonic instability between controlled static convertors and a.c. networks', *Proceedings of IEE*, Vol. 114, No. 7, July, pp. 949–957.

Ainsworth, J. (1968), 'The phase-locked oscillator-a new control system for controlled static convertors', *IEEE Transactions on Power Apparatus and Systems*, Vol. PAS-87, pp. 859–865.

Aprille Jr., T. and Trick, T. (1972), 'Steady-state analysis of nonlinear circuits with periodic inputs', *Proceedings of the IEEE*, Vol. 60, No. 1, January, pp. 108–114.

Arrillaga, J. and Smith, B. (1998), *AC-DC power system analysis*, The Institution of Electrical Engineers, Michael Faraday House, Six Hills Way, Stevenage, Herts. SG1 2AY, United Kingdom.

Arrillaga, J., Medina, A., Lisboa, M., Cavia, M. and Sanchez, P. (1995), 'The harmonic domain. a frame of reference for power system harmonic analysis', *IEEE Transactions on Power Systems*, Vol. 10, pp. 433–440.

Arrillaga, A., Smith, B., Watson, N. and Wood, A. (1997), *Power System Harmonic Analysis*, John Wiley & Sons, Ltd, Baffins Lane, Chichester, West Sussex, PO 19 1UD, England.

Bathurst, G. (1999), *A Newton solution for the harmonic analysis of power systems with multiple non-linear devices*, PhD thesis, Department of Electrical and Electronic Engineering, University of Canterbury.

Bathurst, G., Smith, B., Watson, N. and Arrillaga, J. (1999), 'Modelling of hvdc transmission systems in the harmonic domain', *IEEE Transactions on Power Delivery*, Vol. 14, No. 3, July, pp. 1075–1079.

Bathurst, G., Watson, N. and Arrillaga, J. (2000), 'Modelling of bipolar hvdc links in the harmonic domain', *IEEE Transactions on Power Delivery*, Vol. 15, No. 3, July, pp. 1034–1038.

Chavez, J. (2010), 'A modified dynamic harmonic domain distribution line model', In *Power and Energy Society General Meeting*.

Chavez, J. and Ramirez, A. (2008), 'Dynamic harmonic domain modeling of transients in three-phase transmission lines', *IEEE Transactions on Power Delivery*, Vol. 23, pp. 2294–2301.

Chavez, J., Ramirez, A., Dinavahi, V., Iravani, R., Martinez, J., Jatskevich, J. and Chang, G.W. (2010), 'Interfacing techniques for time-domain and frequency-domain simulation methods', *IEEE Transactions on Power Delivery*, Vol. 25, No. 3, pp. 1796–1807.

Collins, C. (2006), *FACTS device modelling in the harmonic domain*, PhD thesis, Department of Electrical and Electronic Engineering, University of Canterbury.

Dang, J., Liu, D., Bai, X. and Xiong, Y. (2007), 'A simplified tcsc dynamic phasors model considering harmonic characteristics', In *2nd IEEE Conference on Industrial Electronics and Applications*.

de Souza, L. and Watanabe, E. (2009), 'Eliminating gibbs phenomenon from switching ffunction for power electronics circuit analysis', *IEEE Transactions on Power Delivery*, Vol. 24, No. 2, April, pp. 970–971.

Dommel, H. (1969), 'Digital computer solution of electromagnetic transients in single- and multiphase networks', *IEEE Transactions on Power Apparatus and Systems*, Vol. PAS-88, No. 4, March, pp. 734–741.

Dommel, H. (1971), 'Nonlinear and time-varying elements in digital simulation of electromagnetic transients', *IEEE Transactions on Power Apparatus and Systems*, Vol. 90, No. 6, November, pp. 2561–2567.

Dommel, H. (1997), 'Techniques for analyzing electromagnetic transients', *IEEE Computer Applications in Power*, Vol. 10, No. 3, July, pp. 18–21.

Dommel, H. and Meyer, W. (1974), 'Computation of electromagnetic transients', *Proceedings of the IEEE*, Vol. 62, No. 7, pp. 983–993.

Dommel, H., Yan, A. and Wei, S. (1986), 'Harmonics from transformer saturation', *IEEE Transactions on Power Systems*, Vol. 1, No. 2, April, pp. 209–215.

Floquet, G. (1883), 'Sur les équations différentielles linéaires à coefficients périodiques', *Annales de l'École Normale Supérieure*, Vol. 12, pp. 47–89.

Fortescue, C. (1918), 'Method of symmetrical co-ordinates applied to the solution of polyphase networks', In *34th Annual Convention of the American Institute of Electrical Engineers,*, Atlantic City, N.J., June.

Frey, W. and Althammer, P. (1961), 'The calculation of transients on lines by means of a digital computer', *Brown Boveri Rev.*, Vol. 48, May, pp. 334–355.

Garcia, H. and Madrigal, M. (2009), 'Modeling and analysis of a tcr-fc reactive power compensator using the harmonic domain', In *Electronics, Robotics and Automotive Mechanics Conference*.

Garcia, H., Madrigal, M., Vyakaranam, B., Rarick, R. and Villaseca, F. (2011), 'Dynamic companion harmonic circuit model for analysis of power systems with embedded power electronics devices', *Electric Power Systems Research*, Vol. 81, pp. 340–346.

Guckenheimer, J. and Holmes, P. (2002), *Nonlinear Oscillations, Dynamical System, and Bifurcations of Vector Fields*, Springer.

Hammad, A. (1992), 'Analysis of second harmonic instability for the chateauguay hvdc/svc scheme', *IEEE Transactions on Power Delivery*, Vol. 7, No. 1, January, pp. 410–415.

He, R. and Cai, Z. (2005), 'Modeling and harmonic analysis of tcsc with dynamic phasors', In *Transmission and Distribution Conference and Exhibition: Asia and Pacific, 2005 IEEE/PES*.

Hill, G. (1878), 'Researches in lunar theory', *American Journal of Mathematics*, Vol. 1, pp. 129–147.

Hill, G. (1886), 'On the part of the motion of lunar perigee which is a function of the mean motions of the sun and moon', *Acta Mathematica*, Vol. 8, pp. 1–36.

Hingorani, N. and Gyugyi, L. (2000), *Understanding FACTS*, IEEE Press.

Hu, L. and Yacamini, R. (1992), 'Harmonic transfer through converters and hvdc links', *IEEE Transactions on Power Electronics*, Vol. 7, pp. 514–525.

Hu, L. and Yacamini, R. (1993), 'Calculation of harmonics and interharmonics in hvdc ss-cheme with low dc side impedance', *Generation, Transmission and Distribution, IEE Proceedings C*, Vol. 140, No. 6, November, pp. 469–476.

Hume, D. (2002), *Harmonic and Interharmonic Cross Modulation in HVDC Links*, PhD thesis, University of Canterbury, Christchurch, New Zealand.

Hume, D., Wood, A. and Osauskas, C. (2002), 'The effect of ac system impedance on the cross-modulation of distortion in hvdc links', In *10th International Conference on Harmonics and Quality of Power*, pp. 196–201.

Hume, D., Wood, A. and Osauskas, C. (2003), 'Frequency-domain modelling of interharmonics in hvdc systems', *IEE Proceedings on Generation, Transmission and Distribution*, Vol. 150, No. 1, January, pp. 41–48.

IEEE (2000), *The Authoritative Dictionary of IEEE Standards Terms*, IEEE, 7 ed.

Ino, T., Mathur, R., Iravani, M. and Sasaki, S. (1985), 'Validation of digital simulation of dc links - part ii', *IEEE Transactions on Power Apparatus and Systems*, Vol. PAS-104, No. 9, September, pp. 2596–2603.

Jovcic, D., Pahalawaththa, N. and Zavahir, M. (1999), 'Analytical modelling of hvdc-hvac systems', *IEEE Transactions on Power Delivery*, Vol. 14, No. 2, April, pp. 506–511.

Kuffel, P., Kent, K. and Irwin, G. (1997), 'The implementation and effectiveness of linear interpolation within digital simulation', *Electrical Power and Energy Systems*, Vol. 19, No. 4, May, pp. 221–228.

Kulicke, B. (1981), 'Simulation program netomac: Difference conductance method for continuous and discontinuous systems', *Siemens Research and Development Reports*, Vol. 10, No. 5, pp. 299–302.

Larson, E., Baker, D. and McIver, J. (1989), 'Low order harmonic interaction on ac/dc systems', *IEEE Transactions on Power Delivery*, Vol. 4, No. 1, pp. 493–501.

Love, G. (2007), *Small signal modelling of power electronic converters, for the study of time-domain waveforms, harmonic domain spectra, and control interactions*, PhD thesis, Department of Electrical and Computer Engineering, University of Canterbury.

Love, G. and Wood, A. (2008), 'Harmonic state space model of power electronics', In *Proceedings of 13th International Conference on Harmonics and Quality of Power*, Wollongong, Australia, pp. 1–6.

Maguire, T. and Gole, A. (1991), 'Digital simulation of flexible topology power electronic apparatus in power systems', *IEEE Transactions on Power Delivery*, Vol. 6, No. 4, October, pp. 1831–1840.

Mathur, R. and Sharaf, A. (1977), 'Harmonics on the dc side in hvdc conversion', *IEEE Transactions on Power Apparatus and Systems*, Vol. 96, No. 5, September, pp. 1631–1638.

Mattavelli, P., Verghese, G. and Stanković, A. (1997), 'Phasor dynamic of thyristor-controlled series capacitor systems', *IEEE Transactions on Power Systems*, Vol. 12, pp. 1259–1267.

Mattavelli, P., Stanković, A. and Verghese, G. (1999), 'Ssr analysis with dynamic phasor model of thyristor-controlled series capacitor', *IEEE Transactions on Power Systems*, Vol. 14, pp. 200–208.

Middlebrook, R. and Cuk, S. (1976), 'A general unified approach to modelling switching-converter power stages', In *Proceedings of the IEEE Power Electronics Specialists Conference*.

Mohan, N., Robbins, W., Undeland, T., Nilssen, R. and Mo, O. (1994), 'Simulation of power electronic and motion control systems - an overview', *Proceedings of the IEEE*, Vol. 82, No. 8, August, pp. 1287–1302.

Mollerstedt, E. (2000a), *Dynamic Analysis of Harmonics in Electrical Systems*, PhD thesis, Department of Automatic Control, Lund Institute of Technology.

Mollerstedt, E. (2000b), 'Out of control because of harmonics-an analysis of the harmonic response of an inverter locomotive', *IEEE Control Systems*, Vol. 20, pp. 70–81.

Murere, G., Lefebvre, S. and Do, X. (1995), 'A generalized harmonic balance method for emtp initialization', *IEEE Transactions on Power Delivery*, Vol. 10, No. 3, July, pp. 1353–1359.

Nakhla, M. (1976), 'A piecewise harmonic balance technique for determination of periodic response of nonlinear systems', *IEEE Transactions on Circuits and Systems*, Vol. 23, No. 2, February, pp. 85–91.

Noda, T., Yamamoto, K., Nagaoka, N. and Ametani, A. (1997), 'A predictor-corrector scheme for solving a nonlinear circuit', In *Proceedings of IPST*, Seattle, USA, June, pp. 5–10.

O'Reilly, J., Wood, A. and Osauskas, C. (2003), 'Frequency domain based control design for an hvdc converter connected to a weak ac network', *IEEE Transactions on Power Delivery*, Vol. 18, No. 3, July, pp. 1028–1033.

Orillaza, J. (2012), *Harmonic State Space Model of Three Phase Thyristor Controlled Reactor*, PhD thesis, Department of Electrical and Computer Engineering, University of Canterbury.

Orillaza, J. and Wood, A. (2008), 'Linearized harmonic domain model for three-phase thyristor controlled reactor', In *Australasian Universities Power Engineering Conference*, Sydney, Australia, December.

Orillaza, J. and Wood, A. (2013), 'Harmonic state-space model of a controlled tcr', *IEEE Transactions on Power Delivery*, Vol. 28, January, p. 1.

Orillaza, J., Hwang, M. and Wood, A. (2010), 'Switching instant variation in harmonic state-space modelling of power electronic devices', In *Australasian Universities Power Engineering Conference*, University of Canterbury, Christchurch, New Zealand, December.

Osauskas, C. and Wood, A. (1998), 'A frequency domain model of a thyristor controlled reactor', In *8th International Conference on Harmonics and uality of Power*, Athens, Greece, October.

Osauskas, C. and Wood, A. (2003), 'Small-signal dynamic modeling of hvdc systems', *IEEE Transactions on Power Delivery*, Vol. 18, No. 1, January, pp. 220–225.

Perkins, B., Marti, J. and Dommel, H. (1995), 'Nonlinear elements in the emtp: Steady-state initialization', *IEEE Transactions on Power Systems*, Vol. 10, No. 2, May, pp. 593–601.

Persson, E. (1970), 'Calculation of transfer functions in grid-controlled convertor systems', *IEE Proceedings*, Vol. 117, No. 5, May, pp. 989–997.

Power Electronics Modeling Task Force & Digital Simulation Working Group (1997), 'Guidelines for modeling power electronics in electric power engineering applications', *IEEE Transactions on Power Delivery*, Vol. 12, No. 1, January.

Ramirez, A. (2011), 'The modified harmonic domain: interharmonics', *IEEE Transactions on Power Delivery*, Vol. 26, pp. 235–241.

Rico, J., Madrigal, M. and Acha, E. (2003), 'Dynamic harmonic evolution using the extended harmonic domain', *IEEE Transactions on Power Delivery*, Vol. 18, pp. 587–594.

Sakui, M. and Fujita, H. (1992), 'Calculation of harmonic currents in a three-phase convertor with unbalanced power supply conditions', *IEE Proceedings*, Vol. 139, p. 478.

Sakui, M., Yanase, A. and Fujita, H. (1985), 'Line harmonic current of three-phase thyristor bridge rectifier circuit with dc current ripple and overlapping angle', *Electrical Engineering in Japan*, Vol. 105, No. 6, pp. 48–55.

Sakui, M., Fujita, H. and Shioya, M. (1989), 'A method for calculating harmonic currents of a three-phase bridge uncontrolled rectifier with dc filter', *IEEE Transactions on Industrial Electronics*, Vol. 36, pp. 434–440.

Sanders, S., Noworolski, J., Liu, X. and Verghese, G. (1991), 'Generalized averaging method for power conversion circuits', *IEEE Transactions on Power Electronics*, Vol. 6, No. 2, April, pp. 251–259.

Segundo, J. and Medina, A. (2008), 'Periodic steady-state solution of electric systems including upfcs by extrapolation to the limit cycle', *IEEE Transactions on Power Delivery*, Vol. 23, No. 3, July.

Semlyen, A. and de León, F. (1993), 'Computation of electromagnetic transients using dual or multiple time steps', *IEEE Transactions on Power Systems*, Vol. 8, No. 3, August, pp. 1274–1281.

Semlyen, A. and Medina, A. (1995), 'Computation of the periodic steady state in systems with non-linear components using a hybrid time and frequency domain methodology', *IEEE Transactions on Power Systems*, Vol. 10, No. 3, August, pp. 1498–1504.

Smith, B., Watson, N., Wood, A. and Arrillaga, J. (1996a), 'Newton solution for the steady-state interaction of ac/dc systems', *IEE Proceedings on Generation, Transmission and Distribution*, Vol. 142, No. 2, March, pp. 200–210.

Smith, B., Watson, N., Wood, A. and Arrillaga, J. (1996b), 'A newton solution for the harmonic phasor analysis of ac/dc converters', *IEEE Transactions on Power Delivery*, Vol. 11, No. 2, April, pp. 965–971.

Smith, B., Arrillaga, J., Wood, A. and Watson, N. (1998), 'A review of iterative harmonic analysis for ac-dc power systems', *IEEE Transactions on Power Delivery*, Vol. 13, No. 1, January, pp. 180–185.

Sood, V. (2004), *HVDC and FACTS Controllers Applications of Static Converters in Power Systems*, Kluwer Academic Publishers, 101 Philip Drive, Assinippi Park, Norwell, Massachusetts 02061, USA.

Stanković, A., Mattavelli, P., Caliskan, V. and Verghese, G. (2000), 'Modeling and analysis of facts devices with dynamic phasors', In *Power and Energy Society Winter Meeting*, Singapore.

Stefanov, P. and Stanković, A. (2002), 'Modeling of upfc operation under unbalanced conditions with dynamic phasors', *IEEE Transactions on Power Systems*, Vol. 17, No. 2, May.

Sucena-Paiva, J. and Freris, L. (1974), 'Stability of a dc transmission link between weak ac systems', *IEE Proceedings*, Vol. 121, No. 6, June, pp. 508–515.

Thallam, R. (1992), 'Review of the design and performance features of hvdc systems connected to low short circuit ratio ac systems', *IEEE Transactions on Power Delivery*, Vol. 7, No. 4, October, pp. 2065–2073.

Todd, S. and Wood, A. (1997), 'An s-domain model of an hvdc converter', *IEEE Transactions on Power Delivery*, Vol. 12, No. 4, October, pp. 1723–1729.

Vyakaranam, B., Madrigal, M., Villaseca, F. and Rarick, R. (2010), 'Dynamic harmonic evolution in facts via the extended harmonic domain method', In *Power and Energy Conference at Illinois*.

Wang, Q. and Marti, J. (1996), 'A waveform relaxation technique for steady state initialization of circuits with nonlinear elements and ideal diodes', *IEEE Transactions on Power Delivery*, Vol. 11, No. 3, July, pp. 1437–1443.

Wereley, N. (1991), *Analysis and Control of Linear Periodically Time Varying Systems*, PhD thesis, Department of Aeronautics and Astronautics, Massachusetts Institute of Technology.

Wood, A. (1993), *An analysis of non-ideal HVdc convertor behaviour in the frequency domain, and a new control proposal*, PhD thesis, Department of Electrical and Electronic Engineering, University of Canterbury.

Wood, A. and Arrillaga, J. (1995a), 'Composite resonance; a circuit approach to the waveform distortion dynamics of an hvdc converter', *IEEE Transactions on Power Delivery*, Vol. 10, pp. 1882–1888.

Wood, A. and Arrillaga, J. (1995b), 'Hvdc convertor waveform distortion: a frequency-domain analysis', *IEE Proceedings, Transmission and Distribution*, Vol. 142, pp. 88–96.

Wood, A. and Osauskas, C. (2004), 'A linear frequency-domain model of a statcom', *IEEE Transactions on Power Delivery*, Vol. 19, No. 3, July, pp. 1410–1418.

Wood, A., Hume, D. and Osauskas, C. (2000), 'Linear analysis of waveform distortion for hvdc and facts devices', In *Ninth International Conference on Harmonics and Quality of Power*, Orlando, FL.

Woodford, D., Gole, A. and Menzies, R. (1983), 'Digital simulation of dc links and ac machines', *IEEE Transactions on Power Apparatus and Systems*, Vol. PAS-102, No. 6, June, pp. 1616–1623.